Computational Modeling to Guide Cardiac Electrophysiological Therapies

A DISSERTATION PRESENTED
BY
THIEN-KHOI N. PHUNG
TO
THE FACULTY OF THE SCHOOL OF ENGINEERING AND APPLIED SCIENCE
UNIVERSITY OF VIRGINIA

IN PARTIAL FULFILLMENT OF THE REQUIREMENTS
FOR THE DEGREE OF
DOCTOR OF PHILOSOPHY
IN THE SUBJECT OF
BIOMEDICAL ENGINEERING

UNIVERSITY OF VIRGINIA
CHARLOTTESVILLE, VIRGINIA
MAY 2020

©2020 – Thien-Khoi N. Phung
all rights reserved.

APPROVAL SHEET

The dissertation is submitted
in partial fulfillment of the requirements
for the degree of
Doctor of Philosophy

Author Thien-Khoi N. Phung

The dissertation has been read and approved by the examining committee:

Advisor Jeffrey W. Holmes
Chair Silvia S. Blemker
Kenneth C. Bilchick
Frederick H. Epstein
Seth H. Weinberg

Accepted for the School of Engineering and Applied Science

Craig H. Benson
Dean, School of Engineering and Applied Science
May 2020

This work is dedicated

to my brother, Thien-Chuong Phung, who inspired me to pursue engineering,

and to my parents, Kim-Trang Nguyen and Chuong Phung, who nurtured my curiosity and creativity.

Acknowledgments

My sincerest gratitude to my friends and family who have encouraged and supported me throughout graduate school. The work in this dissertation is the product of many minds, and I would like to take them all. In the projects presented throughout the dissertation, I want to sincerely thank the following who contributed immensely to this work:

- Chapter 2- Christian Moyer, Patrick Norton, John Ferguson, & Jim Whayne
- Chapter 3- Christopher Waters, Pim Oomen, Daniel Auger, & Mohammad Abdishektaei
- Chapter 4- Craig Goodman, Jeremy Gatesman, Seth Weinberg, & Cory Weller
- Chapter 5- Kyoko Yoshida, Ana Estrada, & Derek Bivona

I also want to thank my advisor, Jeffrey Holmes, and the Cardiac Biomechanics Group who have all provided a generous learning environment for me to develop as a researcher. I am so fortunate to have been able to work along side *Team Growth*- Colleen, Kyoko, Ana, Derek, and Pim- who have helped me develop my confidence and competence as a computational biomechanics modeler. Thank you to Ana and Derek who have been my comedic relief in lab as we spent each day troubleshooting our failed models.

Lastly, I want to thank my friends who have helped me make endlessly joyful memories throughout graduate school. I want to thank the Tuesday trivia crew, Cory, Eric, KT, Ana, Chris, and Marc. I want to thank Laura who helped me expand beyond lab work into running my first race in Charlottesville as well as joining the Crozet Community Orchestra. And I want to thank Liz and Sham who have been my family away from home ♡

Contents

1

Introduction

1.1 Electro-mechanical physiology of the heart

The human heart functions as a well-coordinated system of pumps that delivers blood throughout the body. An organized electrical network of specialized cells throughout the heart controls the timing of mechanical contraction of the four muscle chambers. The electrical signaling is initiated by a periodic action potential transmitted by a series of ions crossing channels in the cell membrane. In a healthy heart, the electrical pacing originates from cells of the sinoatrial node in the right atrium, which periodically depolarize due to leaky ion channels. The electrical signal then rapidly travels across the heart through a network of cells connected by gap junctions, which allow for ions to rapidly pass between cells.

The electrical signaling triggers muscle contraction through the influx of calcium ions into the cell as part of the action potential. This process, known as excitation-contraction coupling, causes additional release of sequestered calcium in the cell, which then binds to troponin, a protein that regulates the contraction. Contraction in cardiac muscle cells occurs by the sliding of different muscle fiber filaments towards each other, described as the sliding filament theory, to

generate a force and effectively shorten the cell along the muscle fiber direction[1,2] Rapid, coordinated activation of the cardiac muscle contracts the chambers to effectively eject blood. Importantly, the normal pattern of electrical signaling coordinates contraction of the atria slightly before the ventricles. This precise timing allows for the atria to pump blood into the ventricles before the ventricles pump that blood throughout the body.

The heart's function can break down when either electrical or mechanical properties are altered. For example, in atrial fibrillation and premature ventricular contraction, cells not located in the sinoatrial node can trigger contraction by spontaneously misfiring an action potential. In the case of myocardial infarction (heart attack), blockage of blood flow to the heart muscle can lead to tissue death reducing the heart's ability to pump. Electrical and mechanical abnormalities in the heart can further trigger remodeling processes such as fibrosis and hypertrophy. The goal of many cardiac therapies is to halt and even reverse these remodeling processes.

1.2 Computational modeling of the heart

Advances in computational modeling now allow simulation of complex electro-mechanical function of the heart and have advanced the development of cardiac therapies. These simulations span 0-D lumped parameter models to 3-D finite-element models, each providing increasing physiologic resolution that inevitably increases computational costs. The lumped parameter models have been used to simulate mechanical dysfunction with disease as well as predict organ-level long-term remodeling.[3–5] More complex finite-element models have been used to simulate the electrical and mechanical consequences of myocardial infarction and understand the effect of cardiac therapies at the cell and tissue level.[6–8] Despite the many advances of *in silico* methods, the application of computational mechanical modeling to the clinic has stalled as the needs of researchers and physicians diverge.

As computational resources become more readily accessible to researchers, the complexity of computational models has scaled allowing for higher spatial and temporal resolution simulations.[9] While these biophysical models can serve as tools to understand multi-scale function, they provide a level of detail that may not be relevant for the clinic. When designing computational models for clinical translation, simplicity is valuable. Models should provide relevant spatial reso-

lution for a specific use case and low computational cost. As researchers continue to employ more powerful computational models, there remains tremendous potential in using lower dimensional models, which require orders of magnitude less computation time.[10]

1.3 Computational modeling to guide cardiac electrophysiologic therapies

In this dissertation, we developed computational models of the heart to guide different cardiac electrophysiological therapies. Each chapter leverages computational modeling techniques with different spatial resolutions and computational costs. Chapter 2 presents a finite-element mechanical model used to simulate the effect of catheter ablation for atrial fibrillation in the left atrium. The model is used as a test-bed for head-to-head comparisons between different, commonly used ablation patterns. Chapter 3 presents a data fusion method for registering multimodal imaging data to guide cardiac resynchronization therapy. This data fusion routine is currently employed in a randomized clinical trial* and serves as a crucial model building step for further biophysical simulations presented in later chapters. In Chapters 4 and 5, we present the development of an electro-mechanical modeling pipeline, *Virtual CRT*, for predicting long-term outcomes of cardiac resynchronization therapy. The electrical model in Chapter 4 was developed to be computationally efficient and compatible for coupling with practically any mechanical modeling methods. The finite-element mechanical model in Chapter 5 was designed to assess the importance of various model parameters in simulating accurate regional LV mechanics. Together, Chapters 4 and 5 represent important initial steps towards creating a clinically translatable computational modeling framework for CRT.

*clinicaltrials.gov/ct2/show/NCT03398369

References

[1] A. F. Huxley and R. Niedergerke, "Structural changes in muscle during contraction," *Nature*, vol. 4412, no. 4412, pp. 971–973, 1954.

[2] H. Huxley and J. Hanson, "Changes in the Cross-Striations of Muscle during Contraction and Stretch and their Structural Interpretation," *Nature*, vol. 173, pp. 973–976, 5 1954.

[3] P. J. A. Oomen, C. M. Witzenburg, T.-K. N. Phung, K. C. Bilchick, and J. W. Holmes, "Fast Predictions of Cardiac Growth During Ventricular Dyssynchrony," in *Proceedings of the 2019 Summer Biomechanics, Bioengineering and Biotransport Conference*, (Seven Springs, PA), 2019.

[4] J. Walmsley, T. Arts, N. Derval, P. Bordachar, H. Cochet, S. Ploux, F. W. Prinzen, T. Delhaas, and J. Lumens, "Fast Simulation of Mechanical Heterogeneity in the Electrically Asynchronous Heart Using the MultiPatch Module," *PLoS Computational Biology*, vol. 11, no. 7, pp. 1–23, 2015.

[5] C. M. Witzenburg and J. W. Holmes, "Predicting the Time Course of Ventricular Dilation and Thickening Using a Rapid Compartmental Model," *Journal of Cardiovascular Translational Research*, vol. 11, pp. 109–122, 4 2018.

[6] A. C. Estrada, K. Yoshida, S. A. Clarke, and J. W. Holmes, "Longitudinal Reinforcementof Acute Myocardial Infarcts Improves Function by Transmurally Redistributing Stretch and Stress," *Journal of Biomechanical Engineering*, vol. 142, no. 2, pp. 1–10, 2020.

[7] J. D. Moreno, Z. I. Zhu, P.-C. Yang, J. R. Bankston, M.-T. Jeng, C. Kang, L. Wang, J. D. Bayer, D. J. Christini, N. A. Trayanova, C. M. Ripplinger, R. S. Kass, and C. E. Clancy, "A Computational Model to Predict the Effects of Class I Anti-Arrhythmic Drugs on Ventricular Rhythms," *Science Translational Medicine*, vol. 3, pp. 83–98, 8 2011.

[8] J. White, E. Ukwatta, N. A. Trayanova, E. McVeigh, H. Arevalo, F. Vadakkumpadan, F. Pashakhanloo, A. Prakosa, M. Rajchl, A. C. Lardo, and D. A. Herzka, "Image-based reconstruction of three-dimensional myocardial infarct geometry for patient-specific modeling of cardiac electrophysiology," *Medical Physics*, vol. 42, no. 8, pp. 4579–4590, 2015.

[9] B. Baillargeon, N. Rebelo, D. D. Fox, R. L. Taylor, and E. Kuhl, "The living heart project: A robust and integrative simulator for human heart function," *European Journal of Mechanics, A/Solids*, vol. 48, no. 1, pp. 38–47, 2014.

[10] J. W. Holmes and J. Lumens, "Clinical Applications of Patient-Specific Models: The Case for a Simple Approach," *Journal of Cardiovascular Translational Research*, vol. 11, pp. 71–79, 4 2018.

2

Simulating the effect of ablation on mechanical function in the left atrium

2.1 Introduction

2.1.1 Left atrial function

The left atrium (LA) is a muscular chamber that pumps oxygenated blood received from the lungs into the left ventricle. Throughout the cardiac cycle, the LA undergoes three distinct functional phases consisting of filling, passive emptying, and active emptying. While filling and passive emptying occur when the muscle walls are relaxed, the active emptying phase occurs when the atrial muscle contracts. Active emptying contributes to about 30% of the total emptying volume of the LA in healthy patients.[1]

2.1.2 Atrial fibrillation

Atrial fibrillation (AF) is a condition featuring disorganized electrical signaling within the atria leading to irregular pump function. AF typically starts as intermittent episodes separated by periods of normal sinus rhythm; however, left untreated, the episodes of irregular pumping can become more frequent and lead to progressive atrial and ventricular remodeling and mechanical dysfunction.[2] The stages of AF are categorized based on increasing severity as paroxysmal, persistent, and permanent. In a study that measured LA emptying volumes in patients with paroxysmal AF, active emptying contributed to about 60% of the total emptying volume, a drastic increase compared to healthy patients.[3]

2.1.3 Catheter ablation

Treatment for AF often involves catheter ablation, which induces scar formation to electrically isolate misfiring electrical signals in the atrium. Successful ablation frequently restores sinus rhythm; however, it does so at the cost of replacing contractile muscle with non-contractile scar tissue. The success and development of ablation in treating AF has led to increased utilization, with many arguing for it as a first-line therapy.[4–6] A range of ablation patterns have emerged to target different atrial regions, as well as new ablation catheters that increase both scar volume and transmurality.[7–10] While eliminating electrical abnormalities in the atrium is a main goal of ablation, the scar introduced by ablation has also been shown to impair mechanical function including both atrial contractility and compliance.[11]

2.1.4 Preserving left atrial mechanical function

Imaging of the LA has shown regional motion of the different walls to be highly heterogeneous in both healthy and AF patients imaged in sinus rhythm.[12,13] The differences in contribution from the different regions to active and passive atrial emptying led Kuklik et al. to suggest that ablation in regions with greater mechanical function should be minimized to preserve global atrial function.[14] Given the availability of multiple widely accepted ablation procedures that target different regions of the LA, it may be possible to choose procedures that achieve both goals of restoring normal electrical function and preserving mechanical function. However, the impact of various

ablation procedures on regional and global mechanical function has received only limited attention. In this chapter, we used a computational model shown previously to reproduce mechanics measured in paroxysmal AF patients to simulate various ablation patterns and determine their effect on atrial global and regional function.[3]

2.2 Methods

2.2.1 Modeling left atrial function

Our group previously developed a coupled finite-element (FE) and hemodynamic circuit model of the left atrium to provide insight into the mechanics of paroxysmal AF.[3] The AF model featured a dilated, more spherical geometry, diffuse fibrosis, increased pressure load, reduced conduction velocity, and impaired left ventricular relaxation. The coupling to a circuit model accounted for upstream (pulmonary veins) and downstream (left ventricle and systemic arteries) hemodynamic interactions that determine atrial pressures and volumes as atrial properties and function change. The model also introduced a set of force boundary conditions to represent the impact of contact with adjacent structures and downward force exerted by the left ventricle on the mitral annulus on atrial shape and mechanics. This model reproduced not only global differences in atrial function between healthy subjects and paroxysmal AF patients, but also the regional variations in function observed in both groups.[3]

This baseline AF model was used as a platform to simulate changes in atrial function following the introduction of various ablation scar patterns. Global function of the atrium was analyzed by comparing pressure-volume loops generated from the FE models. To compare effects of ablation on passive versus active emptying, the amounts of emptying occurring during each phase were computed and compared. Wall motion analysis was used to evaluate the regional effects of different ablation patterns. Anatomic regions of the atrium were defined using pulmonary vein and mitral valve landmarks, and wall motion was calculated as a change in radius using a fixed centroid as described by Moyer et al.[12]

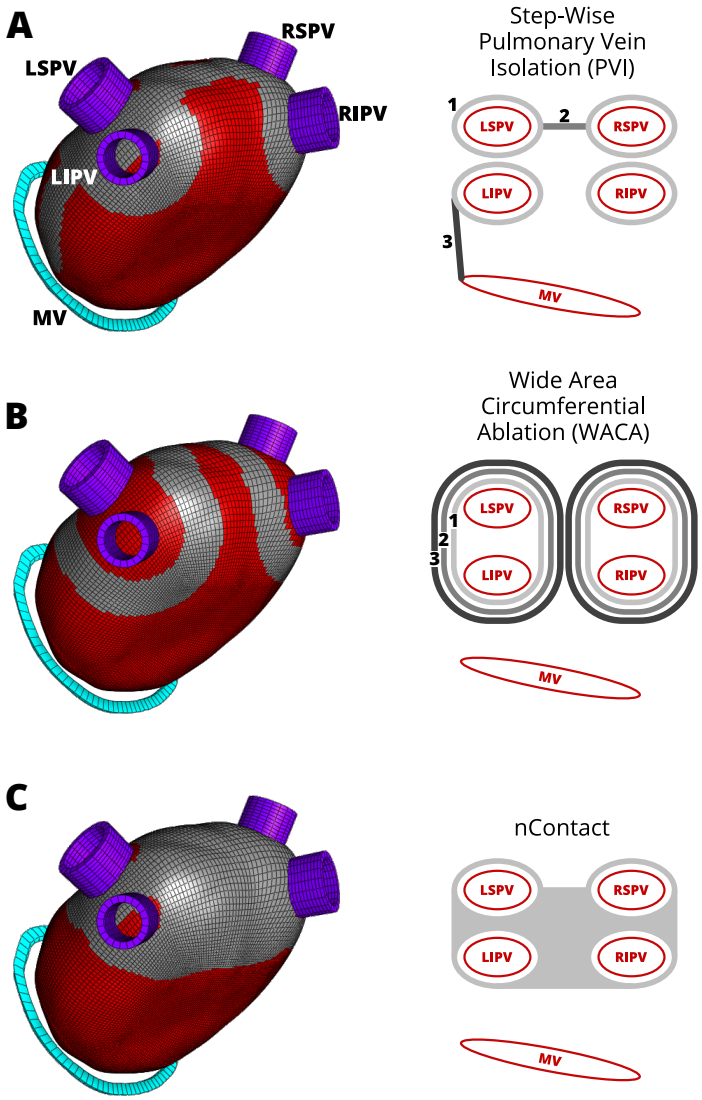

Figure 2.1: Simulated ablation patterns (gray) shown on the FE model (left, single variant shown) and schematically (right, all variants shown) with respect the locations of the mitral valve (MV), left superior (LSPV), left inferior (LIPV), right superior (RSPV), and right inferior pulmonary veins (RIPV). PVI (A) was simulated step-wise using PVI alone, PVI plus a roof line, or PVI plus roof line and isthmus line. WACA (B) was simulated at three different distances from the pulmonary veins. All PVI and WACA variants were simulated using two ablation widths to replicate RF and cryoablation. The nContact (C) ablation pattern was simulated in a single variant consisting of PVI plus ablation of a substantial portion of the posterior wall.

2.2.2 Simulating ablation scar

Ablation scar patterns were introduced by transmurally modifying local material properties in the finite-element model to increase passive stiffness and eliminate active contraction. 13 ablation patterns were tested in our model, including variations of two widely used ablation patterns – step-wise pulmonary vein isolation (PVI) and wide area circumferential ablation (WACA) – as well as a posterior ablation developed by nContact, Inc. that is currently in clinical trials (Fig. 2.1).

The first step-wise PVI model included four scar rings circling each pulmonary vein at 150% of its diameter (Fig. 2.1A). A roof line linking the shortest path between the superior pulmonary veins and an isthmus line connecting the left inferior pulmonary vein to the mitral valve were added sequentially to create the other two PVI models, reflecting common variants of the PVI procedure.[15–17] The three WACA patterns were created by encircling the left and right pairs of pulmonary veins at a distance of 0.5, 1, or 2 cm to represent the range of published WACA methods (Fig. 2.1B).[18–20] The PVI and WACA patterns were simulated using two widths of scar (4 and 8 mm) to represent radiofrequency and cryoablation lines based on typical widths of the catheters used. The nContact pattern was created by combining the PVI plus roof line scar at a width of 5 mm with ablation of the posterior wall bounded by the pulmonary veins (Fig. 2.1C). Myocardium was represented in the model using a transversely-isotropic Mooney-Rivlin material with active contraction. Moyer et al. originally simulated diffuse fibrosis of the atrial myocardium in a typical AF patient by increasing one of the isotropic material coefficients (C_2 = 4.0 kPa).[3] In this study, we simulated ablation scar by stiffening the material further (C_2 = 8.0 kPa) and eliminating anisotropy (C_3 and C_4 = 0) and active contraction to yield properties consistent with post-infarction myocardial scar tissue in animal models.[21] Scar volumes from each ablation pattern were calculated as percentages of atrial wall volume. Because we assumed a constant wall thickness and fully transmural ablation scar, these scar volume fractions also represent the fraction of the endocardial area occupied by scar.

2.3 Results

2.3.1 Global function

The simulated ablation patterns spanned a range of 5% to 31% scar volume. PVI varied from 5% to 20% scar while WACA varied from 13% to 31%. The nContact pattern created 25% scar. In the presence of ablation, the atrium was stiffer during passive filling, as indicated by a lower peak volume and increased slope of the passive "tail" of the simulated pressure-volume loops (Fig. 2.2). Ablation also decreased the active work performed by the atrium with each cycle, as indicated by a decreased loop area.

Total emptying volumes decreased by up to 11 mL following simulated ablation in comparison to baseline (Fig. 2.3A). When comparing the passive and active portions of the emptying volume, changes in active emptying accounted for most of the changes in total emptying volume. While passive emptying varied by less than 1 mL across all the ablation patterns simulated, active emptying decreased with increasing scar volume, up to 44% (11 mL) in the most aggressive lesion simulated (Fig. 2.3B). For ablation patterns with nearly matched scar volumes, WACA patterns decreased active emptying more than PVI (Fig. 2.3B, open and closed circles at 17-19% scar) or the nContact pattern (Fig. 2.3B, square vs. open circle at 25-26% scar).

2.3.2 Regional motion

To better understand the differences between ablation patterns with matched scar volumes, we examined predicted wall motion of the different atrial regions. The walls of the atrial finite-element model were mapped to a two-dimensional hammer projection (Fig. 2.4A), and the total change in radius calculated from the time of maximal atrial volume to the time of minimum atrial volume. In the baseline AF model, radial motion increased from the pulmonary veins towards the mitral valve, with the highest average motion in the inferior and lateral walls (Fig. 2.4B).

To compare the effects of different ablation patterns, the radial motion for the baseline (non-ablated) model was subtracted from the radial motion of the ablation models to calculate the change in regional wall motion (Fig. 2.4C-E) due to ablation. The cryoablation PVI without roof or isthmus line (17% scar) and cryoablation WACA with radius of 0.5 cm (26% scar) were used as representative models for the PVI and WACA groups. All ablation patterns depressed

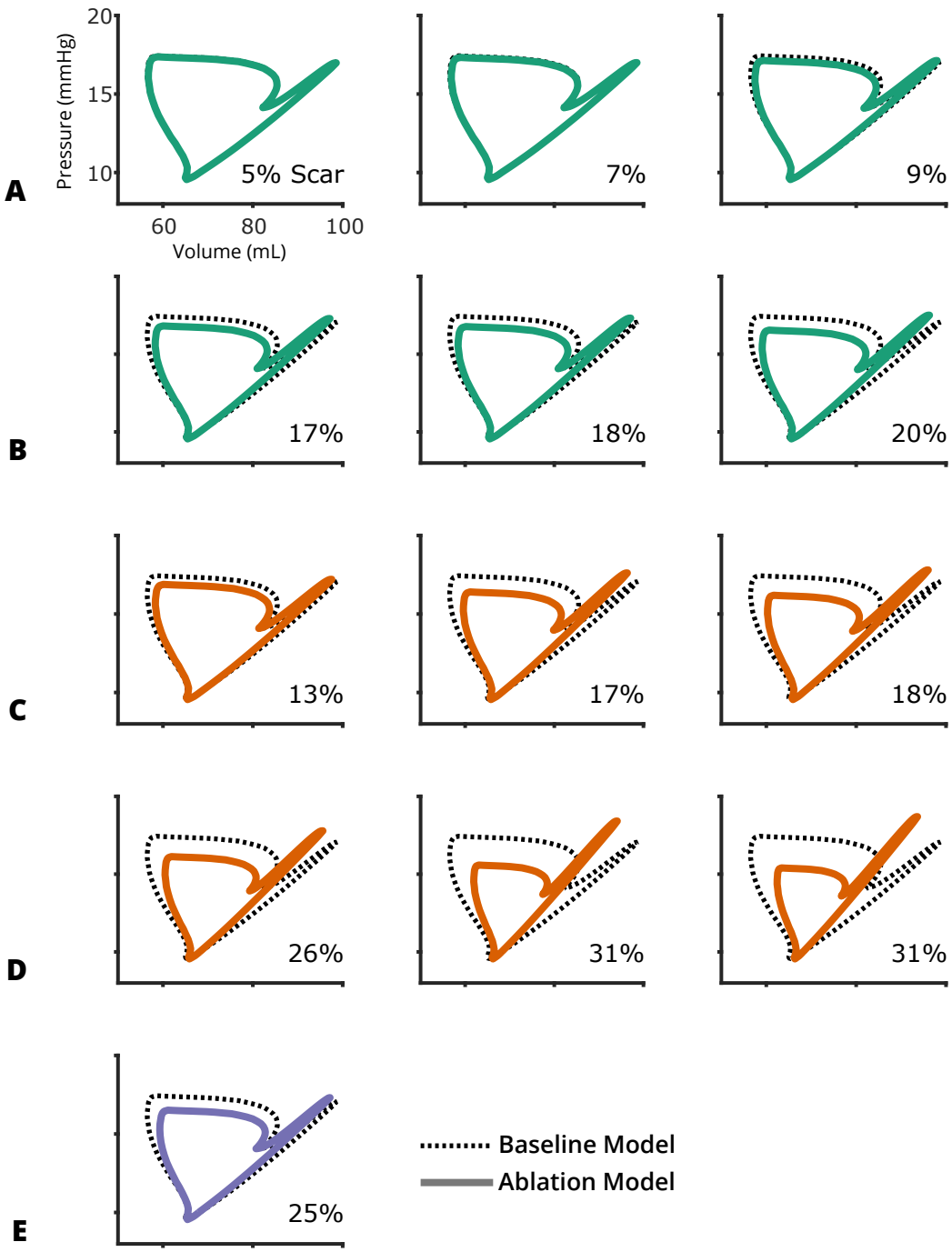

Figure 2.2: Pressure-volume loops from the ablation models (solid line) show that ablation increased passive atrial stiffness (increased slope of linear "tail" on right side of each loop) and decreased active work (area inside the loop) compared to baseline (dotted line). A and B show the variants of step-wise PVI for radiofrequency and cryoablation, respectively. C and D show the variants of WACA for radiofrequency and cryoablation, respectively. And E shows the result from the nContact ablation pattern. Ablation scar amount (by percent wall mass) is indicated in each plot.

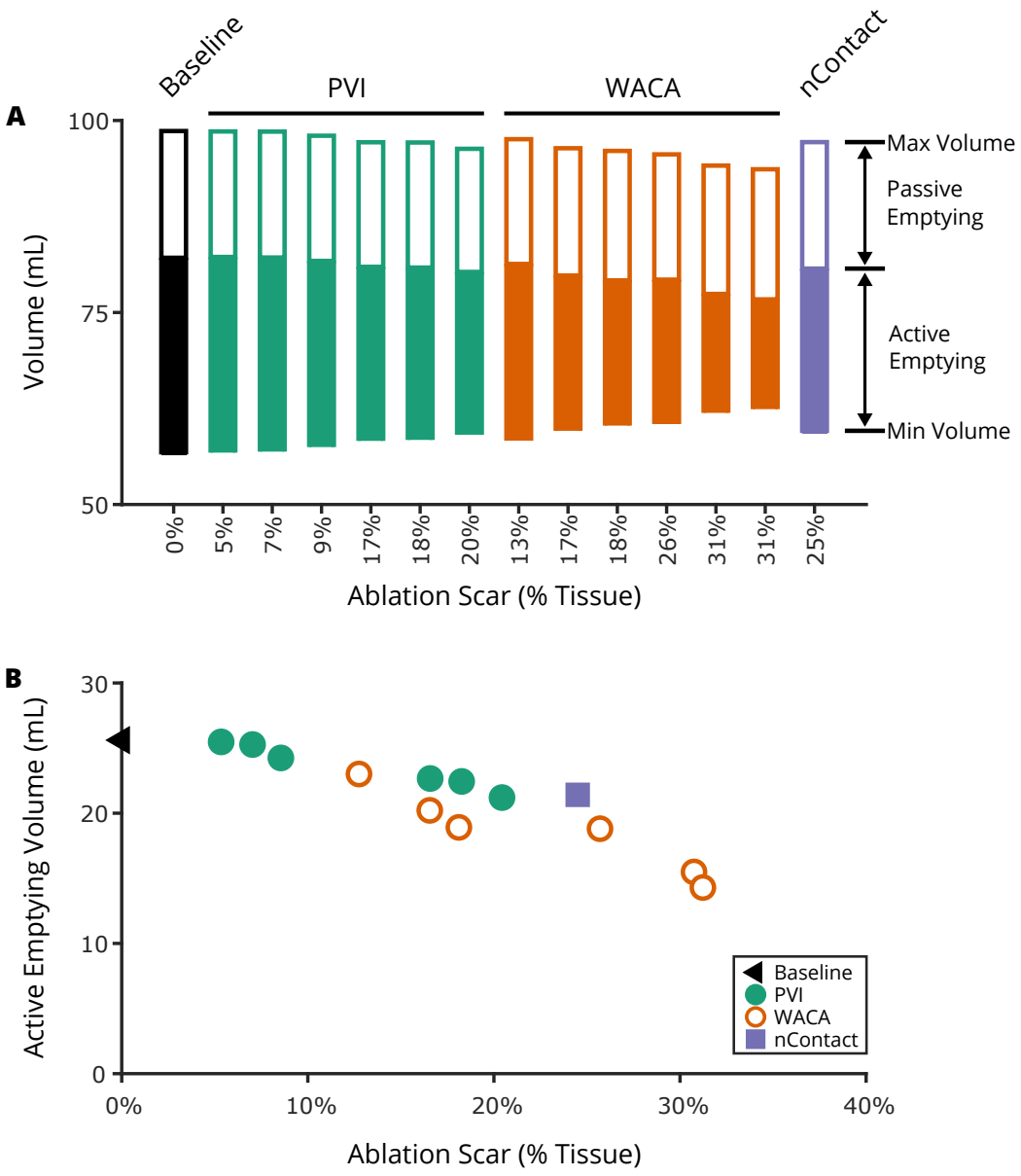

Figure 2.3: (A) Bar graphs of atrial volumes for all models indicating contributions from passive (open portion of bar) and active (closed portion) emptying of the atrium. Active emptying accounted for most of the decrease in total emptying volume with ablation across the procedures simulated. (B) Active emptying decreased with increasing ablation scar volume. At matched scar volumes, PVI and nContact ablation decreased active emptying less than WACA. Active emptying volume decreased by about 3 mL per 10% ablation scar.

radial motion throughout large regions of the atrium; however, the extent and distribution of this depression varied. For example, the 0.5 cm-radius cryoablation WACA (Fig. 2.4D, 26% scar) produced substantial depression in wall motion, particularly in the lateral wall. By contrast, the nContact ablation pattern produced a much smaller and more evenly distributed reduction in wall motion (Fig. 2.4E), even though the total scar volume was nearly identical (25%). The average radial wall motion calculated for each region is summarized in Figure 2.4F. Consistent with the location of the lesions, WACA reduced lateral wall motion more than the other patterns.

2.4 Discussion

In this chapter, we used a computational model that accurately reproduces regional and global mechanics measured in paroxysmal AF patients to simulate a number of variants of commonly employed ablation patterns and determine their effect on atrial global and regional function. The simulated ablations covered a range of scar volumes (5-31% of left atrial wall volume) and by design involved different regions of the atrium. Passive stiffness increased and active atrial emptying decreased as scar volume increased in our simulations, consistent with recent clinical reports .[11] In addition, our simulations suggested that the location of ablation scar is an important determinant of its functional impact: at matched scar volume, WACA lesions impaired active function more than other ablation patterns because WACA involves regions of the lateral wall that normally have the highest regional function in AF patients. By contrast, a novel ablation pattern that focuses on the posterior wall produced less functional depression than expected from its size, because baseline wall motion is already low in the posterior wall.

2.4.1 Effect of ablation scar volume

The simulated ablation patterns in our finite-element model spanned a range of scar volumes similar to those reported from MRI.[10,11,22] For example, Badger et al. showed that AF patients with successful AF termination received 16.4 ± 9.8% scar from ablation,[22] while Cochet et al. quantified ablation scar volume of 29 ± 6% in patients treated for persistent AF. Across this range, we found that ablation scar reduced active emptying volume by 2.7 mL per 10% scar (Fig. 2.3B). Computing active emptying fraction (AEF) using the formula employed by Cochet et. al., this

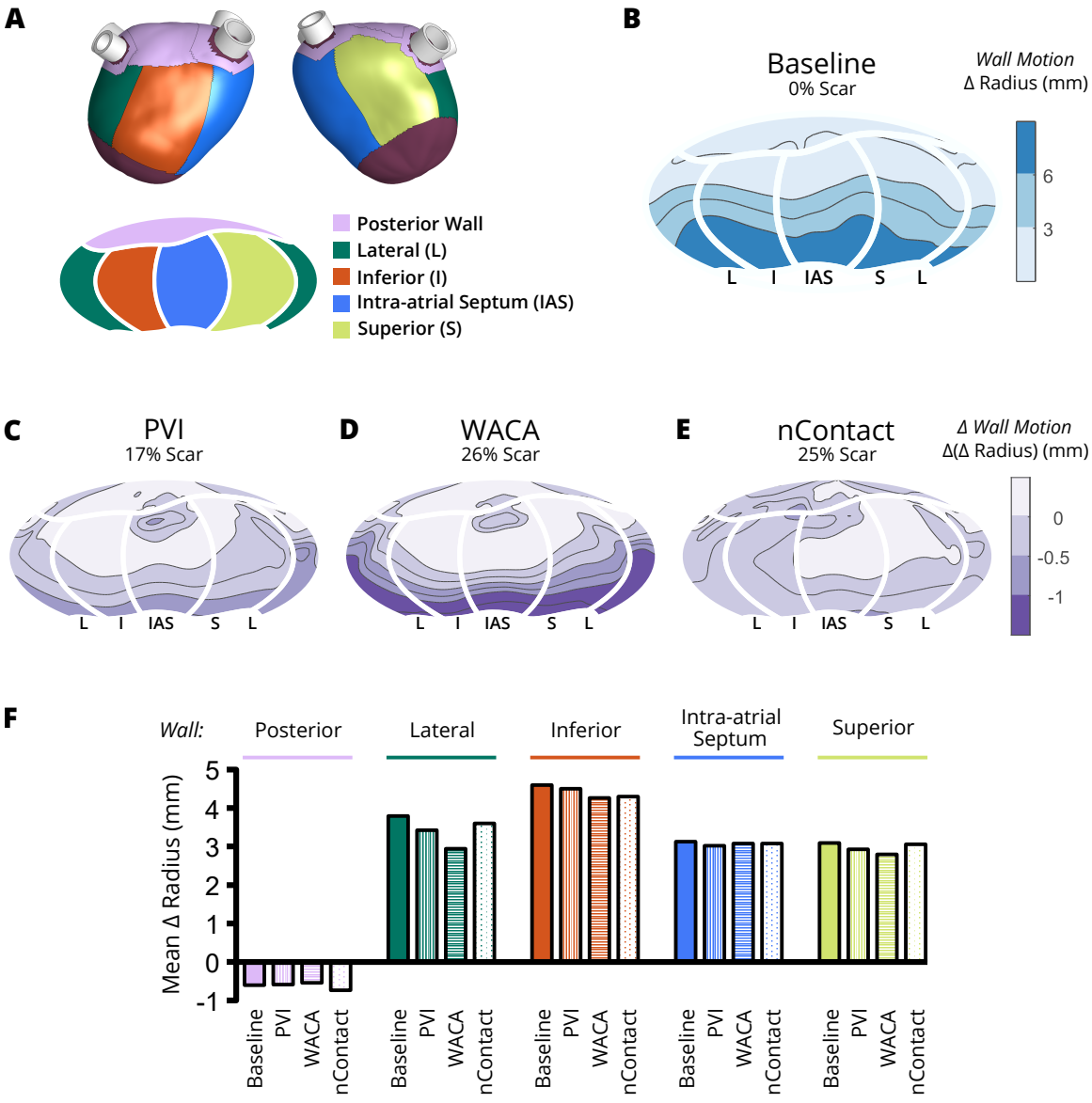

Figure 2.4: (A) Regional atrial function was mapped onto 2-D hammer projections. (B) Baseline atrial motion increased towards the mitral valve and was highest on average in the lateral and inferior walls. (C-E) Maps of change in radial motion for cryoablation PVI without roof or isthmus line (17% scar), cryoablation WACA with radius of 0.5 cm (26%), and nContact (25%) showed the greatest disruption with WACA, particularly in the lateral wall. (F) Average radial motion showed highest baseline function in the lateral and inferior walls, with WACA decreasing regional motion more than nContact, particularly in the lateral wall.

corresponds to a 3% change in AEF per 10% scar versus their reported 10% per 10% scar.[11]

In comparison to the baseline AF model, simulated ablation scar increased stiffness during passive filling as expected. However, the effect of this increased stiffness on passive atrial filling and emptying was largely offset by the fact that the model atrium was connected to a simulated circulation: at steady-state, slightly elevated pulmonary venous pressures helped preserve filling in the face of increased atrial stiffness, and higher peak pressures promoted passive emptying. Thus, passive filling and emptying of the atrium was minimally affected across the range of scar volumes and ablation patterns considered here.

By contrast to passive function, replacing contractile muscle with non-contractile scar substantially impaired active function, with pressure-volume loops for the ablation models revealing a decrease in loop area reflecting a decrease in active work (Fig. 2.2) and active emptying volume dropping by nearly half in some simulations (Fig. 2.3). Our model may actually under-estimate the impact of ablation on active pumping, because reduced filling would be expected to yield less forceful atrial contraction through the Frank-Starling mechanism, which has been reported to play a role in normal atrial function but was omitted from our model.[1,23] The loss of active emptying following ablation in our simulations could be particularly significant given that active emptying appears to play a more important role in AF patients than in healthy subjects: Moyer et al. found that patients with paroxysmal AF who were imaged in sinus rhythm relied on active emptying for 61% of their total emptying volume.[3] While active emptying plays a lesser role for young healthy patients, its fraction of total emptying increases with age, which is also associated with increased incidence of AF.[24–31]

2.4.2 Effect of ablation scar location

Atrial wall motion has been shown to be an effective metric for assessing left atrial active function.[12,32] Throughout the cardiac cycle, the walls of the atrium move heterogeneously, each contributing differently to atrial function. Therefore, it was not surprising that creating ablation scar in different locations of our model atrium impaired active atrial function to different degrees, even at matched scar volume (Fig. 2.3B). Specifically, PVI variations and the nContact ablation pattern decreased active function less than WACA variations when the ablation patterns featured similar scar volumes. Consistent with our prior measurements in paroxysmal AF patients,

at baseline the lateral and inferior walls displayed the greatest motion (Fig. 2.4A), suggesting a greater contribution from these regions to overall atrial function.[12] Motion in these two regions decreased with the presence of ablation scar, but the lateral wall was impacted much more by the WACA pattern (Fig. 2.4C, F) than the other ablations, because the lesions affected regions of the lateral wall with high baseline motion. Providing some support to these model results, Nori et al. reported that both total emptying volume and lateral wall radial motion decreased following WACA ablation in paroxysmal AF patients.[33]

Simulated ablations involving the posterior wall had little effect on function in large part because the posterior wall contributed very little to function at baseline. In the model, this was due primarily to the fact that the pulmonary veins were modeled as rigid bodies fixed in space, thereby tethering the motion of surrounding regions. However, it is important to note that this feature of the model was designed to match measurements by our group using MRI and reported in Moyer et al.[12] We tracked the pulmonary vein ostia over the entire cardiac cycle in both normal volunteers and AF patients imaged in sinus rhythm, and found that the average peak displacement of the centroid of the ostia was less than 2 mm. Thus, we believe that the boundary conditions imposed at the pulmonary veins in our simulations reasonably represent the actual *in vivo* mechanics of the human left atrium.

Although we focus in this chapter primarily on the difference among the three principal ablation patterns (PVI, WACA, nContact), the differences among the variants of PVI we simulated also suggest that the location of individual ablation lines helps determine the degree to which they reduce active function. For example, the three green circles plotted on the left side of Figure 2.3B show the impact of PVI alone, PVI plus a roof line, and PVI plus a roof line and isthmus line on active emptying. Relative to baseline (black triangle), PVI alone had very little effect on active emptying, and adding a roof line also had little impact; however, adding an isthmus line reduced emptying volume noticeably. These results reinforce the concept that creating ablation scar in locations with high baseline motion (such as the lateral wall) reduces active atrial function more than creating in ablation scar in locations with little baseline motion (such as the posterior wall). This principle may be useful in thinking about functional effects of CAFE and rotor ablation and other procedures not explicitly simulated here.

2.4.3 Study limitations

AF is characterized by abnormalities in electrical signaling through the atrium. Our models assumed a transmural ablation scar with no impact on electrical activity except the loss of active contraction in scar regions. For simplicity, we assumed that ablation scar was transmural and that ablation always restored sinus rhythm. While our models allowed for direct comparison of mechanical function among ablation patterns, there is a need for models that can simulate not only the mechanical but also electrical effects of specific ablation patterns.

In modeling post-ablation scar tissue, we were forced to approximate passive mechanical properties based on published infarct scar mechanics, given a lack of information on how material properties change post-ablation;[34] however, since the loss of active function turned out to be much more important in our simulations than the change in passive function, we expect any error in the assumed scar material properties to have minimal impact on the conclusions of the study. Our model geometry intentionally omitted the left atrial appendage due to its heterogeneity among patients.[35] This omission imposes several limitations on our simulations and their interpretation. First, we cannot simulate AF procedures that target the appendage. Second, because we do not represent the contributions of the LAA to atrial pump function, we cannot predict how any of the ablation sets modeled here will alter those contributions. Finally, in practice the presence of the LAA restricts the anterior extent of WACA lesions surrounding the left pulmonary veins, but in our model these lesions were represented as complete circles; thus, the model may over-estimate the impact of WACA lesions on function in the anterior portion of the lateral wall (Fig. 2.4D, far right portion of map).

Our baseline (pre-ablation) model is described here and in a prior methods paper as representing the mechanics of the atrium in paroxysmal AF patients. However, nothing about the model actually incorporates clinical history. Rather, this description reflects the fact that the geometry, wall motion, and hemodynamic data used to construct the model were all obtained from patients with AF who met clinical criteria for ablation but were in normal sinus rhythm when data were collected prior to ablation. When considering this model relative to the very broad range of structural remodeling present across the AF patient population, it may be more useful to think of it as a model of a moderately dilated (maximum volume 100 ml) and diffusely fibrotic (25% aver-

age collagen content) atrium with moderately elevated pressures (minimum pressure 10 mmHg); more details about the choice of these parameters are available in Moyer et al.[3]

2.5 Conclusion- Guiding therapy development for AF

Our simulations support emerging evidence that increasing ablation scar volume depresses atrial function, primarily by reducing active emptying. Furthermore, our model suggests that both amount and location of scar are important determinants of its functional impact. Simulated WACA created ablation scar in regions with high baseline motion (portions of the lateral and inferior walls closer to the mitral valve), which resulted in greater depression of active function in comparison to PVI and the recently introduced nContact ablation pattern. Our results suggest that when multiple options with similar efficacy in preventing AF recurrence are available, choosing patterns that avoiding regions of the atrium with high baseline motion may limit detrimental effects of ablation on atrial mechanical function.

References

[1] A. C. Boyd, N. B. Schiller, D. Leung, D. L. Ross, and L. Thomas, "Atrial dilation and altered function are mediated by age and diastolic function but not before the eighth decade," *JACC: Cardiovascular Imaging*, vol. 4, no. 3, pp. 234–242, 2011.

[2] J. Andrade, P. Khairy, D. Dobrev, and S. Nattel, "The clinical profile and pathophysiology of atrial fibrillation: Relationships among clinical features, epidemiology, and mechanisms," *Circulation Research*, vol. 114, no. 9, pp. 1453–1468, 2014.

[3] C. B. Moyer, P. T. Norton, J. D. Ferguson, and J. W. Holmes, "Changes in Global and Regional Mechanics Due to Atrial Fibrillation: Insights from a Coupled Finite-Element and Circulation Model.," *Annals of biomedical engineering*, vol. 43, no. 7, pp. 1600–1613, 2015.

[4] H. Calkins, K. H. Kuck, R. Cappato, J. Brugada, A. John Camm, S. A. Chen, H. J. G. Crijns, R. J. Damiano, D. W. Davies, J. DiMarco, J. Edgerton, K. Ellenbogen, M. D. Ezekowitz, D. E. Haines, M. Haissaguerre, G. Hindricks, Y. Iesaka, W. Jackman, J. Jalife, P. Jais, J. Kalman, D. Keane, Y. H. Kim, P. Kirchhof, G. Klein, H. Kottkamp, K. Kumagai, B. D. Lindsay, M. Mansour, F. E. Marchlinski, P. M. McCarthy, J. L. Mont, F. Morady, K. Nademanee, H. Nakagawa, A. Natale, S. Nattel, D. L. Packer, C. Pappone, E. Prystowsky, A. Raviele, V. Reddy, J. N. Ruskin, R. J. Shemin, H. M. Tsao, and D. Wilber, "2012 HRS/EHRA/ECAS expert consensus statement on catheter and surgical ablation of atrial fibrillation: Recommendations for patient selection, procedural techniques, patient management and follow-up, definitions, endpoints, and research trial design," *Journal of Interventional Cardiac Electrophysiology*, vol. 33, no. 2, pp. 171–257, 2012.

[5] P. Santangeli, L. Di Biase, and a. Natale, "Ablation Versus Drugs: What Is the Best First-Line Therapy for Paroxysmal Atrial Fibrillation?: Antiarrhythmic Drugs Are Outmoded and Catheter Ablation Should Be the First-Line Option for All Patients With Paroxysmal Atrial Fibrillation: Pro," *Circulation: Arrhythmia and Electrophysiology*, vol. 7, no. 4, pp. 739–746, 2014.

[6] M. Wright and S. M. Narayan, "Ablation of atrial fibrillation," *Trends in Cardiovascular Medicine*, vol. 25, no. 5, pp. 409–419, 2015.

[7] C. S. Elayi, A. Verma, L. Di Biase, C. K. Ching, D. Patel, C. Barrett, D. Martin, B. Rong, T. S. Fahmy, Y. Khaykin, R. Hongo, S. Hao, G. Pelargonio, A. Dello Russo, M. Casella, P. Santarelli, D. Potenza, R. Fanelli, R. Massaro, M. Arruda, R. A. Schweikert, and A. Natale, "Ablation for longstanding permanent atrial fibrillation: Results from a randomized study comparing three different strategies," *Heart Rhythm*, vol. 5, no. 12, pp. 1658–1664, 2008.

[8] a. M. Gillinov, E. H. Blackstone, and P. M. Mccarthy, "Atrial fibrillation: current surgical options and their assessment.," *The Annals of thoracic surgery*, vol. 74, no. 6, pp. 2210–7, 2002.

[9] D. Pajitnev, Z. Szalay, M. Kuniss, T. Neumann, S. Zaltsberg, H. Greiss, S. Lehinant, C. Hamm, T. Walther, H. Pitschner, and M. Schönburg, "Hybrid ablation of long standing persistent atrial fibrillation utilizing minimally invasive surgical and endocardial catheter approach: A safety and feasibility study," *The Thoracic and Cardiovascular Surgeon*, vol. 61, p. OP183, 1 2013.

[10] N. M. Segerson, M. Daccarett, T. J. Badger, A. Shabaan, N. Akoum, E. N. Fish, S. Rao, N. S. Burgon, Y. Adjei-Poku, E. Kholmovski, S. Vijayakumar, E. V. R. Dibella, R. S. MacLeod, and N. F. Marrouche, "Magnetic resonance imaging-confirmed ablative debulking of the left atrial posterior wall and septum for treatment of persistent atrial fibrillation: Rationale and initial experience," *Journal of Cardiovascular Electrophysiology*, vol. 21, no. 2, pp. 126–132, 2010.

[11] H. Cochet, D. Scherr, S. Zellerhoff, F. Sacher, N. Derval, A. Denis, S. Knecht, Y. Komatsu, M. Montaudon, F. Laurent, B. M. Pieske, M. Hocini, M. Haïssaguerre, and P. Jaïs, "Atrial structure and function 5 years after successful ablation for persistent atrial fibrillation: An MRI study," *Journal of Cardiovascular Electrophysiology*, vol. 25, no. 7, pp. 671–679, 2014.

[12] C. B. Moyer, P. a. Helm, C. J. Clarke, L. P. Budge, C. M. Kramer, J. D. Ferguson, P. T. Norton, and J. W. Holmes, "Wall-motion based analysis of global and regional left atrial mechanics," *IEEE Transactions on Medical Imaging*, vol. 32, no. 10, pp. 1765–1776, 2013.

[13] R. Vianna-Pinton, C. A. Moreno, C. M. Baxter, K. S. Lee, T. S. M. Tsang, and C. P. Appleton, "Two-Dimensional Speckle-Tracking Echocardiography of the Left Atrium: Feasibility and Regional Contraction and Relaxation Differences in Normal Subjects," *Journal of the American Society of Echocardiography*, vol. 22, no. 3, pp. 299–305, 2009.

[14] P. Kuklik, P. Molaee, P. Podziemski, a. N. Ganesan, a. G. Brooks, S. G. Worthley, and P. Sanders, "Quantitative description of the 3D regional mechanics of the left atrium using cardiac magnetic resonance imaging.," *Physiological measurement*, vol. 35, no. 5, pp. 763–75, 2014.

[15] A. G. Brooks, M. K. Stiles, J. Laborderie, D. H. Lau, P. Kuklik, N. J. Shipp, L. F. Hsu, and P. Sanders, "Outcomes of long-standing persistent atrial fibrillation ablation: A systematic review," *Heart Rhythm*, vol. 7, no. 6, pp. 835–846, 2010.

[16] M. Hocini, P. Jaïs, P. Sanders, Y. Takahashi, M. Rotter, T. Rostock, L. F. Hsu, F. Sacher, S. Reuter, J. Clémenty, and M. Haïssaguerre, "Techniques, Evaluation, and Consequences of Linear Block at the Left Atrial Roof in Paroxysmal Atrial Fibrillation: A Prospective Randomized Study," *Circulation*, vol. 112, no. 24, pp. 3688–3696, 2005.

[17] P. Jais, M. Hocini, L. F. Hsu, P. Sanders, C. Scavee, R. Weerasooriya, L. Macle, F. Raybaud, S. Garrigue, D. C. Shah, P. L. Metayer, J. Clementy, and M. Haissaguerre, "Technique and results of linear ablation at the mitral isthmus," *Circulation*, vol. 110, no. 19, pp. 2996–3002, 2004.

[18] H. Oral, C. Pappone, A. Chugh, E. Good, F. Bogun, F. Pelosi, E. R. Bates, M. H. Lehmann, G. Vicedomini, G. Augello, E. Agricola, S. Sala, V. Santinelli, and F. Morady, "Circumferential pulmonary-vein ablation for chronic atrial fibrillation.," *The New England journal of medicine*, vol. 354, no. 9, pp. 934–41, 2006.

[19] H. Oral, C. Scharf, A. Chugh, B. Hall, P. Cheung, E. Good, S. Veerareddy, F. Pelosi, and F. Morady, "Catheter Ablation for Paroxysmal Atrial Fibrillation: Segmental Pulmonary Vein Ostial Ablation Versus Left Atrial Ablation," *Circulation*, vol. 108, no. 19, pp. 2355–2360, 2003.

[20] C. Pappone, S. Rosanio, G. Oreto, M. Tocchi, F. Gugliotta, G. Vicedomini, A. Salvati, C. Dicandia, P. Mazzone, V. Santinelli, S. Gulletta, and S. Chierchia, "Circumferential Radiofrequency Ablation of Pulmonary Vein Ostia," *Circulation*, vol. 102, no. 21, pp. 2619–2628, 2000.

[21] G. M. Fomovsky and J. W. Holmes, "Evolution of scar structure, mechanics, and ventricular function after myocardial infarction in the rat.," *American journal of physiology. Heart and circulatory physiology*, vol. 298, no. 1, pp. 221–8, 2010.

[22] T. J. Badger, M. Daccarett, N. W. Akoum, Y. A. Adjei-Poku, N. S. Burgon, T. S. Haslam, S. Kalvaitis, S. Kuppahally, G. Vergara, L. McMullen, P. A. Anderson, E. Kholmovski, R. S. MacLeod, and N. F. Marrouche, "Evaluation of Left Atrial Lesions After Initial and Repeat Atrial Fibrillation Ablation: Lessons Learned From Delayed-Enhancement MRI in Repeat Ablation Procedures," *Circulation: Arrhythmia and Electrophysiology*, vol. 3, pp. 249–259, 6 2010.

[23] A. M. Anwar, M. L. Geleijnse, O. I. I. Soliman, A. Nemes, and F. J. ten Cate, "Left atrial Frank-Starling law assessed by real-time, three-dimensional echocardiographic left atrial volume changes.," *Heart (British Cardiac Society)*, vol. 93, no. 11, pp. 1393–7, 2007.

[24] T. M. Alhogbani, O. Strohm, and F. Matthias, "Evaluation of normal atrial contribution to left ventricular filling," *Journal of Cardiovascular Magnetic Resonance*, vol. 12, no. Suppl 1, p. O91, 2010.

[25] J. Heeringa, D. A. M. Van Der Kuip, A. Hofman, J. A. Kors, G. Van Herpen, B. H. C. Stricker, T. Stijnen, G. Y. H. Lip, and J. C. M. Witteman, "Prevalence, incidence and lifetime risk of atrial fibrillation: The Rotterdam study," *European Heart Journal*, vol. 27, no. 8, pp. 949–953, 2006.

[26] Y. Miyasaka, M. E. Barnes, B. J. Gersh, S. S. Cha, K. R. Bailey, W. P. Abhayaratna, J. B. Seward, and T. S. M. Tsang, "Secular trends in incidence of atrial fibrillation in Olmsted County, Minnesota, 1980 to 2000, and implications on the projections for future prevalence," *Circulation*, vol. 114, no. 2, pp. 119–125, 2006.

[27] N. F. Murphy, C. R. Simpson, P. S. Jhund, S. Stewart, M. Kirkpatrick, J. Chalmers, K. MacIntyre, and J. J. V. McMurray, "A national survey of the prevalence, incidence, primary care burden and treatment of atrial fibrillation in Scotland," *Heart*, vol. 93, no. 5, pp. 606–612, 2007.

[28] J. P. Piccini, B. G. Hammill, M. F. Sinner, P. N. Jensen, A. F. Hernandez, S. R. Heckbert, E. J. Benjamin, and L. H. Curtis, "Incidence and prevalence of atrial fibrillation and associated mortality among medicare beneficiaries: 1993-2007," *Circulation: Cardiovascular Quality and Outcomes*, vol. 5, no. 1, pp. 85–93, 2012.

[29] S. Rietbrock, E. Heeley, J. Plumb, and T. van Staa, "Chronic atrial fibrillation: Incidence, prevalence, and prediction of stroke using the Congestive heart failure, Hypertension, Age >75, Diabetes mellitus, and prior Stroke or transient ischemic attack (CHADS2) risk stratification scheme," *American Heart Journal*, vol. 156, no. 1, pp. 57–64, 2008.

[30] K. T. Spencer, V. Mor-Avi, J. Gorcsan, a. N. DeMaria, T. R. Kimball, M. J. Monaghan, J. E. Perez, L. Weinert, J. Bednarz, K. Edelman, O. L. Kwan, B. Glascock, J. Hancock, C. Baumann, and R. M. Lang, "Effects of aging on left atrial reservoir, conduit, and booster pump function: a multi-institution acoustic quantification study.," *Heart (British Cardiac Society)*, vol. 85, no. 3, pp. 272–7, 2001.

[31] T. Wilke, A. Groth, S. Mueller, M. Pfannkuche, F. Verheyen, R. Linder, U. Maywald, R. Bauersachs, and G. Breithardt, "Incidence and prevalence of atrial fibrillation: An analysis based on 8.3 million patients," *Europace*, vol. 15, no. 4, pp. 486–493, 2013.

[32] B. Hesse, S. U. Schuele, M. Thamilasaran, J. Thomas, and L. Rodriguez, "A rapid method to quantify left atrial contractile function: Doppler tissue imaging of the mitral annulus during atrial systole," *European Journal of Echocardiography*, vol. 5, no. 1, pp. 86–92, 2004.

[33] D. Nori, G. Raff, V. Gupta, R. Gentry, J. Boura, and D. E. Haines, "Cardiac magnetic resonance imaging assessment of regional and global left atrial function before and after catheter ablation for atrial fibrillation.," *Journal of interventional cardiac electrophysiology : an international journal of arrhythmias and pacing*, vol. 26, no. 2, pp. 109–17, 2009.

[34] J. W. Holmes, Z. Laksman, and L. Gepstein, "Making better scar: Emerging approaches for modifying mechanical and electrical properties following infarction and ablation," *Progress in Biophysics and Molecular Biology*, vol. 120, no. 1-3, pp. 134–148, 2016.

[35] B. D. Hoit, "Left atrial size and function: Role in prognosis," *Journal of the American College of Cardiology*, vol. 63, no. 6, pp. 493–505, 2014.

3

Data fusion and visualization routine to integrate patient-specific anatomic and functional cardiac information

3.1 Introduction

3.1.1 Dyssynchrony and cardiac resynchronization therapy

The left ventricle (LV) is a muscular chamber approximately the shape of a truncated ellipsoid, which forcefully pumps oxygenated blood received from the left atrium to the rest of the body. The pumping is coordinated through fast electrical signaling along a specialized network of cells known as the Purkinje network. Disruption of the network, such as in left bundle branch block (LBBB), leads to slowing of the signaling and dyssynchrony of contraction in the LV. The pump function deteriorates from a nearly instantaneous contraction of the entire LV to an inefficient, gradual sequence of contraction around the muscle chamber.[1]

Cardiac resynchronization therapy (CRT) employs a pacemaker with electrical leads to restore coordinated muscular contraction. A lead is placed on the LV free wall to deliver an external electrical stimulus to the muscle.[2] The choice of lead placement has been shown to be critical for predicting patient response to CRT.[3] Therefore, there is a need for developing patient-specific methods for customizing CRT lead placement.

3.1.2 Non-invasive imaging of cardiac anatomy and function

A range of cardiac imaging modalities now enable non-invasive collection of data on geometry, motion, perfusion, electrical activation, and even tissue properties such as fibrosis. Each of these pieces of information could help define spatially heterogeneous tissue properties relevant to customizing CRT lead placement. Specific magnetic resonance imaging (MRI) techniques, such as late gadolinium enhancement (LGE) MRI and displacement encoding with stimulated echoes (DENSE) MRI, can provide information about LV scar location and regional mechanics, respectively. Patient-specific metrics related to scar and mechanics have been associated with improved CRT outcomes.[3–5]

3.1.3 Creating patient-specific visuals for guiding CRT

We hypothesized that creating a standardized patient-specific visualization containing relevant information could help streamline physician decision-making when choosing a CRT lead position. However, integrating data across multiple modalities or scans to construct a coherent patient-specific visual is a non-trivial task. Different modalities typically employ different coordinate systems, produce images with different spatial and temporal resolution, and store and display that information in different formats (e.g., a series of 2D slices vs. a 3D surface map). Thus, standardization and sharing of methods for integrating multimodal imaging data has the potential to enhance reproducibility within and across research groups for creating patient-specific visuals and models.[6]

In this chapter, we use non-invasive imaging data of a dyssynchronous LV to demonstrate our method for creating a three-dimensional patient-specific model. We use short- and long-axis cine MRI to construct the LV geometry by fitting the endocardial and epicardial surfaces in prolate spheroidal coordinates. We then interpolate and map data from other MRI sequences onto the

personalized geometry. We focus first on the mapping of scar determined by myocardial LGE MRI and mechanical activation from DENSE MRI a canine subject. We also show an example of the data fusion routine incorporating MRI and CRT using a human data set for pre-procedure planning of CRT. The MATLAB code employed here and a Python version are both available for download from SimTK*. The data fusion routine uses the freely available, MATLAB-based software Segment for MRI segmentation†[7] and generates geometries that port easily to FEBio for finite-element (FE) simulations.[8]

3.2 Methods

3.2.1 Overview of approach

The goal of our method is to combine personalized information from different MRI protocols and/or different imaging modalities to build a model representation of a patient's LV. Combining different MRI imaging sequences acquired during the same exam has the advantage that all data are recorded in the same coordinate system. However, even in this case challenges arise due to differences in image resolution and physiologic state of the patient. For example, while cine MRI provides high spatial and temporal resolution of the heart geometry during the cardiac cycle, LGE MRI provides the geometry of the LV and scar at a lower resolution at end diastole. We resolve these differences by mapping the patient information at a matched cardiac phase (end diastole) to the epicardial surfaces fit from each imaging modality. The epicardial surface was chosen as the platform for information exchange because it is smoother than the endocardial surface and, in our experience, simpler to register across protocols, exams, and imaging modalities. The geometries fit from the different imaging modalities are rotated into a common cardiac coordinate system based on landmark locations on the LV. The data are then projected onto a common visualization created from the high-resolution cine MRI geometry, which is used to create a FE model of the LV.

*simtk.org/projects/lvdatamap
†http://segment.heiberg.se

3.2.2 Constructing the LV finite-element geometry

The patient-specific FE geometry of the LV was generated from multiple short-axis cine MRI slices taken at end diastole. Fitting of the segmented MRI contours to create a finite-element mesh was previously described by our group.[9] Briefly, the epicardial and endocardial surfaces were segmented using software Segment v2.0 R5430[‡].[7] Landmark pinpoints were placed at the right ventricle (RV) insertions in the most basal short-axis slice and at the base (midpoint in the mitral valve plane) and apex in the two-chamber long-axis view to define the cardiac coordinate system (Fig. 3.1A). The segmentations were registered in three dimensions in cardiac coordinates with the x-axis oriented from LV base to apex, y-axis oriented from lateral to septal wall, and z-axis oriented from anterior to posterior wall. The endocardial and epicardial surfaces were independently fit using bicubic Hermite elements (8 circumferential by 4 longitudinal) in a prolate spheroidal coordinate system (Fig. 3.1).[9–11] In this coordinate system, μ describes an angle spanning from apex to base of the LV, θ describes an angle measured circumferentially around the LV from mid septum (Fig. 3.3A), and λ describes a term similar to a radius extending from the origin. The wall mass between the two surface fits was filled with 3,600 linear, hexahedral elements with a resolution of 24 longitudinal by 30 circumferential by 5 radial elements. Interior nodes between the endocardial and epicardial surfaces were created at equally spaced intervals in λ along lines of constant angular (μ, θ) coordinates. The nodes on the epicardial surface were used as the points onto which patient-specific data were projected and exchanged.

3.2.3 Extracting and registering scar location data

Epicardial, endocardial, and scar boundaries were segmented from short-axis and long-axis LGE MRI using semi-automated methods in Segment.[12] Segmentations were registered to map data onto the epicardial surface through the process shown in Figure 3.2. Scar extent was quantified using two metrics: transmurality and starting depth from the epicardium, both expressed as fractions of wall thickness. Scar metrics were computed in individual image slices for 50 evenly spaced bins ranging from 0° to 360° in θ in short-axis slices and 100 evenly spaced bins ranging from 0° to 120° in μ in long-axis slices. These two metrics allowed us to effectively project all information

[‡]segment.heiberg.se

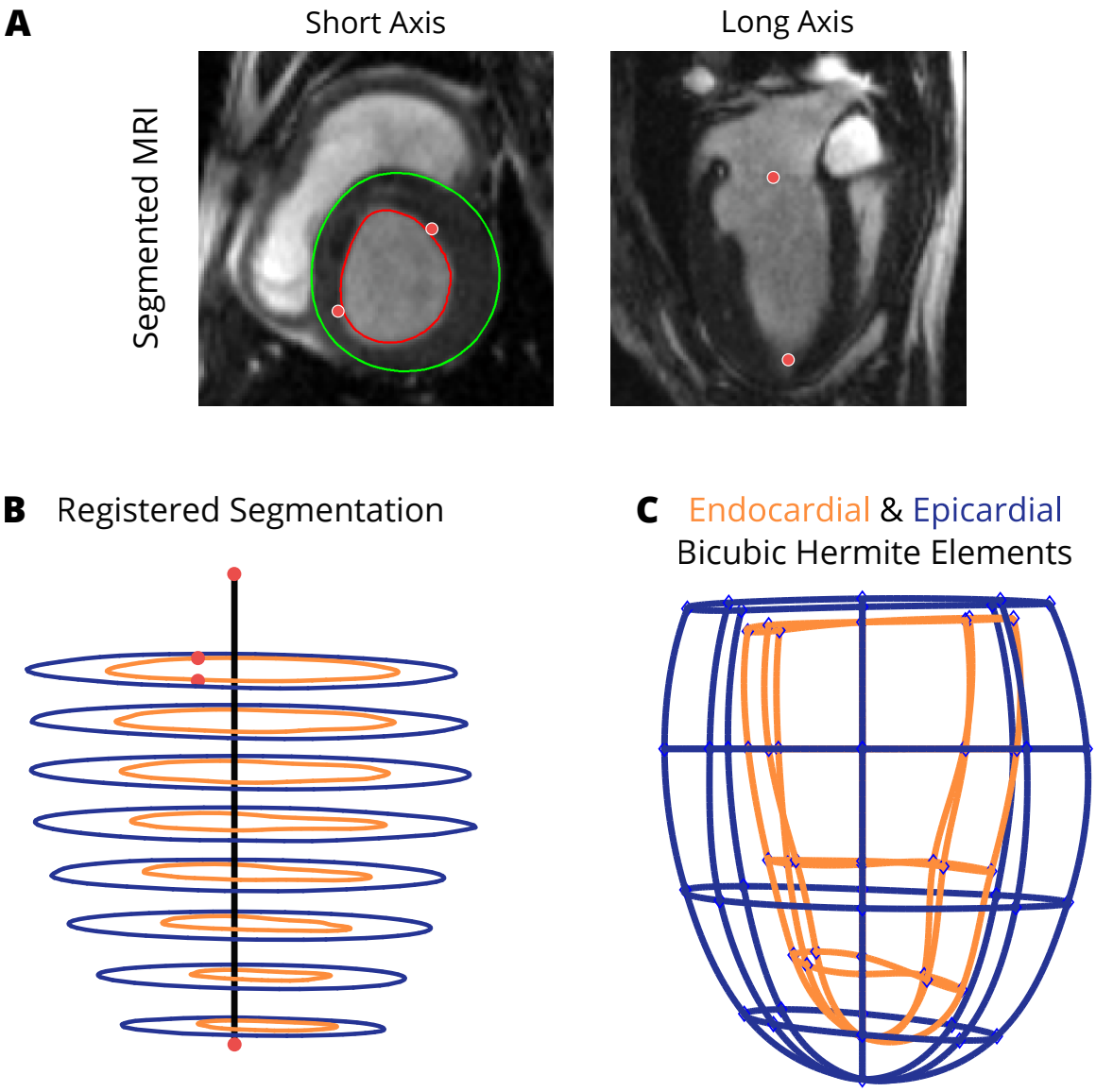

Figure 3.1: Creation of a patient-specific model geometry. (A) Long and short axis cine MRI were segmented and landmarked at the right ventricular insertions, base, and apex points. (B) The segmentations were registered in three dimensions. (C) The endocardial and epicardial surfaces were fit independently using 2D bicubic Hermite elements.

needed to recreate the scar geometry onto the epicardial surface of the ventricle. Landmark points described in the previous section 3.2.2 were selected and used to express segmented scar, endocardial, and epicardial data from the LGE MRI in the same cardiac coordinate system employed to generate the FE geometry. The registered coordinates were converted to a prolate spheroidal coordinate system as detailed above. The (μ, θ) location of each resulting scar data point on the epicardial surface is displayed as circles in Figure 3.3B and 3.3C.

3.2.4 Mapping scar data onto the model geometry

Once scar data were projected onto the epicardial surface from the LGE image slices, the next step was to interpolate and transfer the scar information to the FE model. Defining the prolate spheroidal coordinate system for the geometric fits and the LGE analysis using the same anatomic landmarks allowed us to simply overlay the scar data onto a (μ, θ) grid representing the epicardial surface in the geometric model (Fig. 3.3). The scar transmurality and depth measures were transferred using a scattered, linear interpolation function with nearest neighbor extrapolation in MATLAB. The epicardial nodal points from the FE geometry were used as sample points and the epicardial points containing scar data from LGE as the data points (Fig. 3.3). In order to decide which elements in the finite-element mesh would be considered to be scar, the data at the four nodes of each epicardial element face were averaged to get a single transmurality and depth per transmural stack of elements. The depth value defined the starting scar element from the epicardium in each transmural stack of elements, and the transmurality metric determined the number of elements through each transmural stack that were assigned as scar. Each metric was multiplied by the number of radial elements and rounded to the nearest whole number to determine which elements in a transmural column are scar. For example, given a resolution of 5 elements from epicardium to endocardium through the wall, a scar starting at depth of 9% with transmurality of 57% would be represented as scar starting at the first epicardial element and spanning 3 elements (Fig. 3.4).

3.2.5 Mapping mechanical activation data onto the model geometry

In principle, these same methods can be used to fuse any information that can be expressed as one or more numerical values associated with epicardial surface points. As a second illustration,

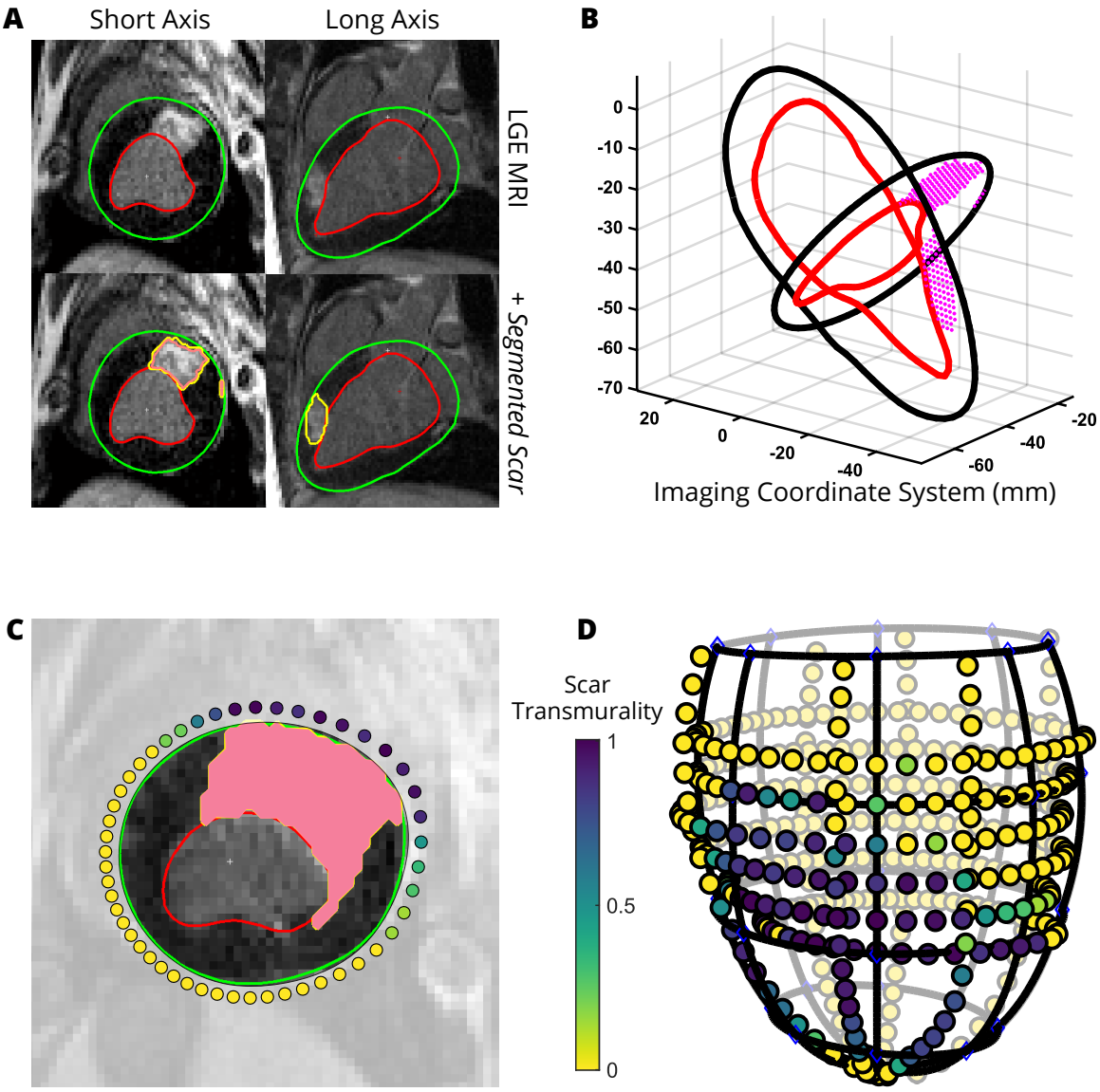

Figure 3.2: Mapping scar onto patient-specific geometry. Long- and short-axis LGE MRI were segmented (A) and registered (B) into their common imaging coordinate system. Transmurality of the segmented scar was calculated and projected onto the epicardial surface of the heart in each image (C). The scar transmurality data from all images were projected onto the epicardial surface (wireframe) fitted to the segmented epicardial contours (D).

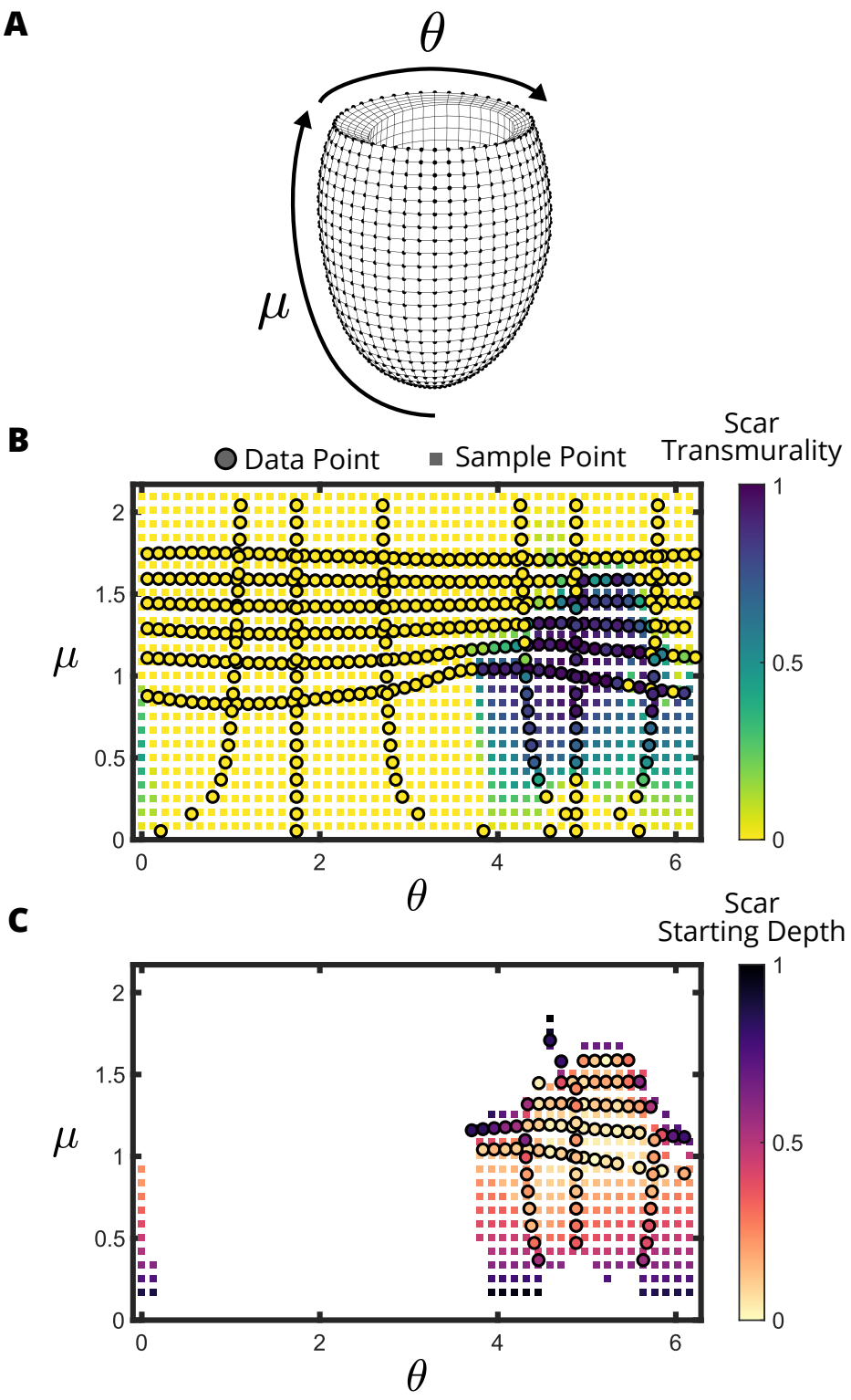

Figure 3.3: Fusion of geometric data from cine MRI and scar location data from LGE MRI. (A) Diagram of the prolate spheroid coordinate system with arrows showing the two angular coordinates that describe the location of any point on the epicardial surface. (B) After expressing both the fitted epicardial nodes and the scar data on the same coordinate system and registering them, information about scar transmurality calculated from the different LGE MRI imaging planes (closed circles) was transferred to the epicardial nodes (squares) of the finite-element mesh by interpolation. (C) The same interpolation procedure was also used to transfer information on scar starting depth.

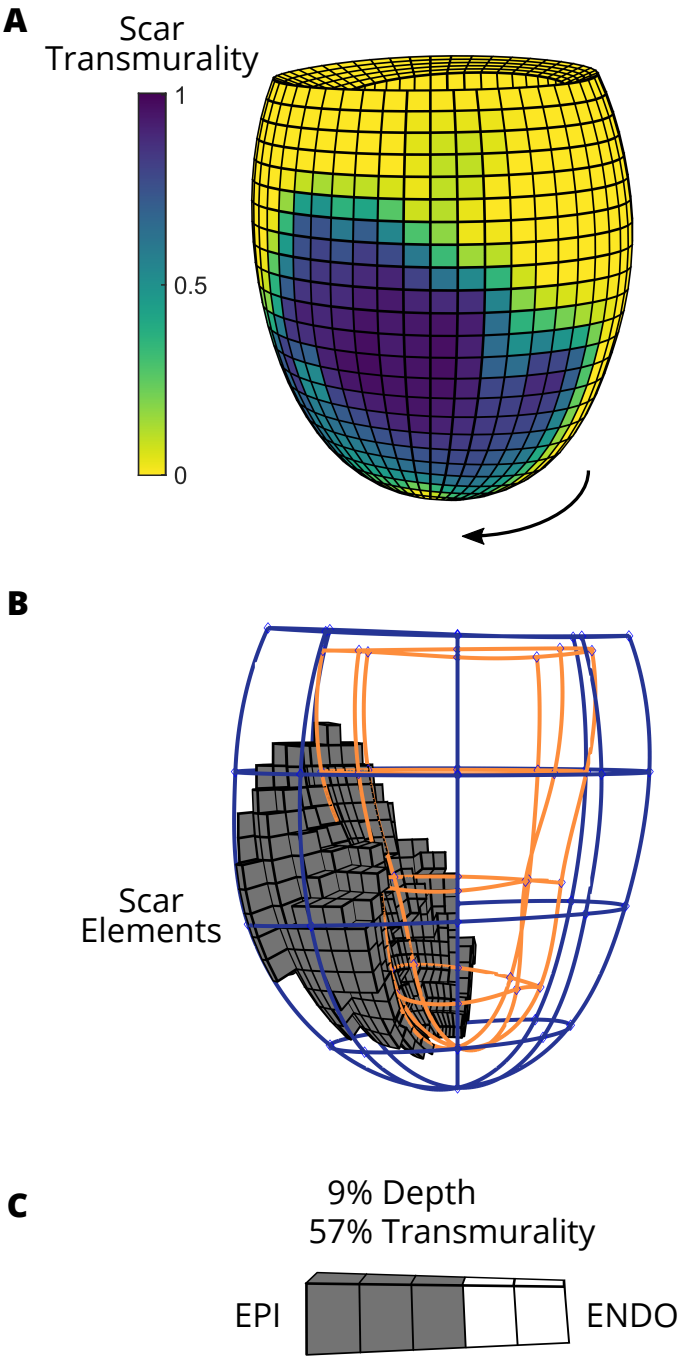

Figure 3.4: Visualizing scar in a patient-specific model. (A) Scar transmurality is represented as a heat map on the epicardial surface of the finite-element mesh and shown in an anterior view (anterior wall of left ventricle in front). (B) The reconstructed scar location is visualized in a lateral view to display the variable depth and transmural extent (lateral wall of left ventricle in front). The blue and orange meshes show the epicardial and endocardial surfaces of the finite-element mesh, and the gray boxes indicate elements designated as scar. (C) A single transmural column of elements is shown with the interpolated scar transmurality and depth at the corresponding μ and θ values.

we mapped mechanical activation time calculated from DENSE MRI short-axis slices onto the finite-element mesh (Fig. 3.5).[4] Since these data already consisted of a single number (activation time) associated with each of 18 segments per short-axis DENSE slice, we were able to transfer this information using interpolation of a single metric. We used linear interpolation between the short-axis slices and nearest neighbor extrapolation above and below the most basal and apical short-axis slices.

3.2.6 Combining multi-modal imaging onto a patient-specific model

We created a map of the scar transmurality, mechanical activation, and coronary vein anatomy onto a single patient-specific epicardial geometry for guiding CRT.[13,14] This map featured data fusion between LGE MRI, DENSE MRI, and CT. On the scar transmurality epicardial map created from LGE MRI, we overlaid mechanical activation time for any regions that had no scar. Coronary vein anatomy was segmented from CT and registered to MRI-derived surface by aligning RV insertion points and the base-apex axis. The coronary veins are displayed as a binary mask on a slightly larger epicardial surface which hovered above the true epicardial surface (Fig. 3.6).

3.3 Results

3.3.1 Validation of scar mapping

In order to assess the ability of the entire pipeline to accurately map LGE scar data onto a geometric model, we created plane cuts through the final FE model that approximated the MRI planes used for LGE MRI acquisition and compared the resulting images side-by-side (Fig. 3.7). Although the FE model geometry was created from a separate cine MRI sequence rather than the LGE images shown in the comparison, the dimensions and shape of the LV appeared similar, with some loss of detail around the papillary muscles due to smoothing apparent in short-axis cuts of the model. Long and short axis views showed comparable scar location and transmurality to the segmented LGE MRI.

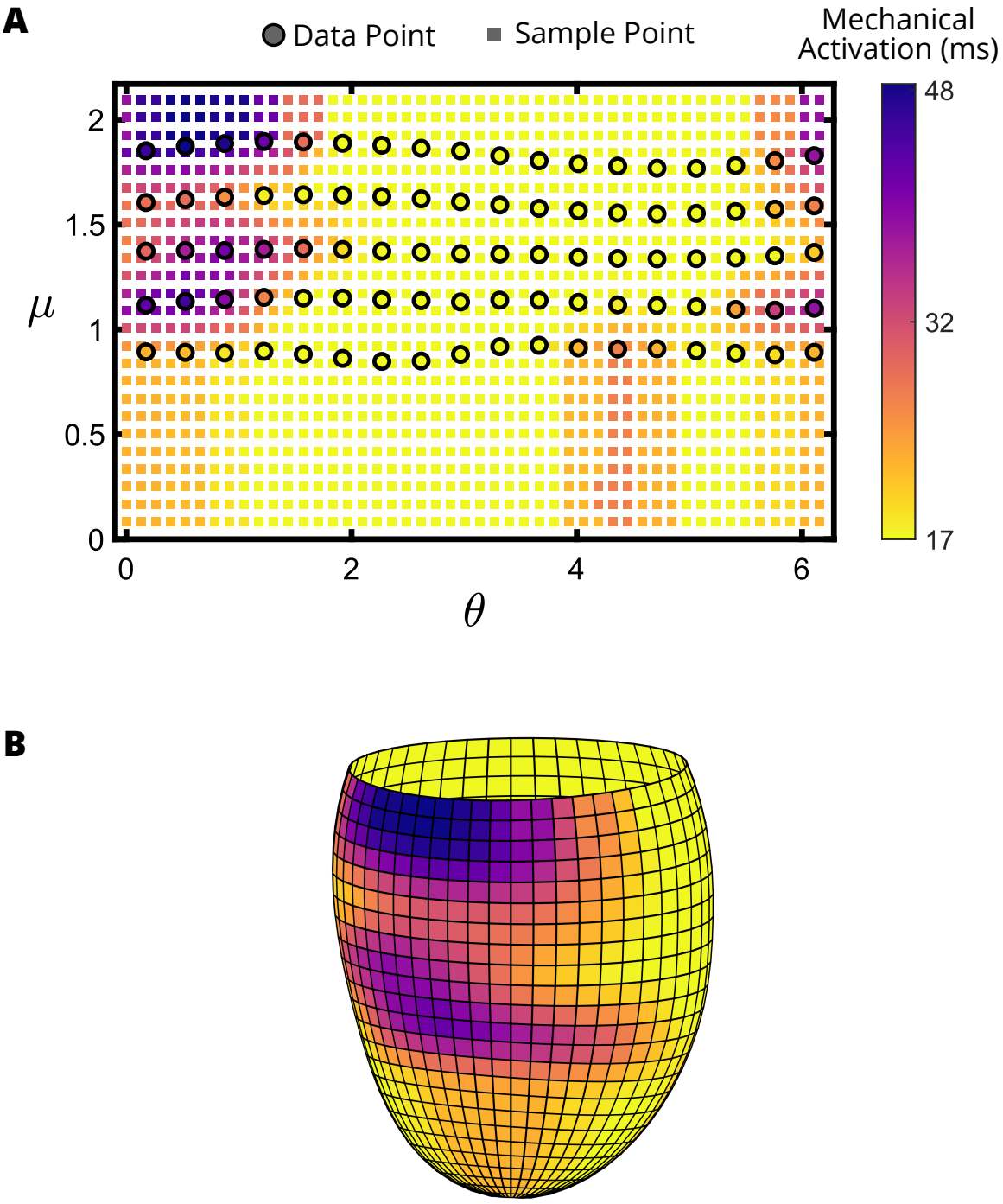

Figure 3.5: Mapping mechanical activation onto patient-specific geometry. (A) Mechanical activation was calculated from DENSE MRI for each of 18 segments in 5 short-axis slices and registered with the fitted finite-element geometry (closed circles). The epicardial nodes of the finite-element mesh were used as sample points (squares), and mechanical activation times estimated at each using a combination of interpolation and extrapolation. (B) Mechanical activation is shown as a heat map on the epicardial surface of the geometry.

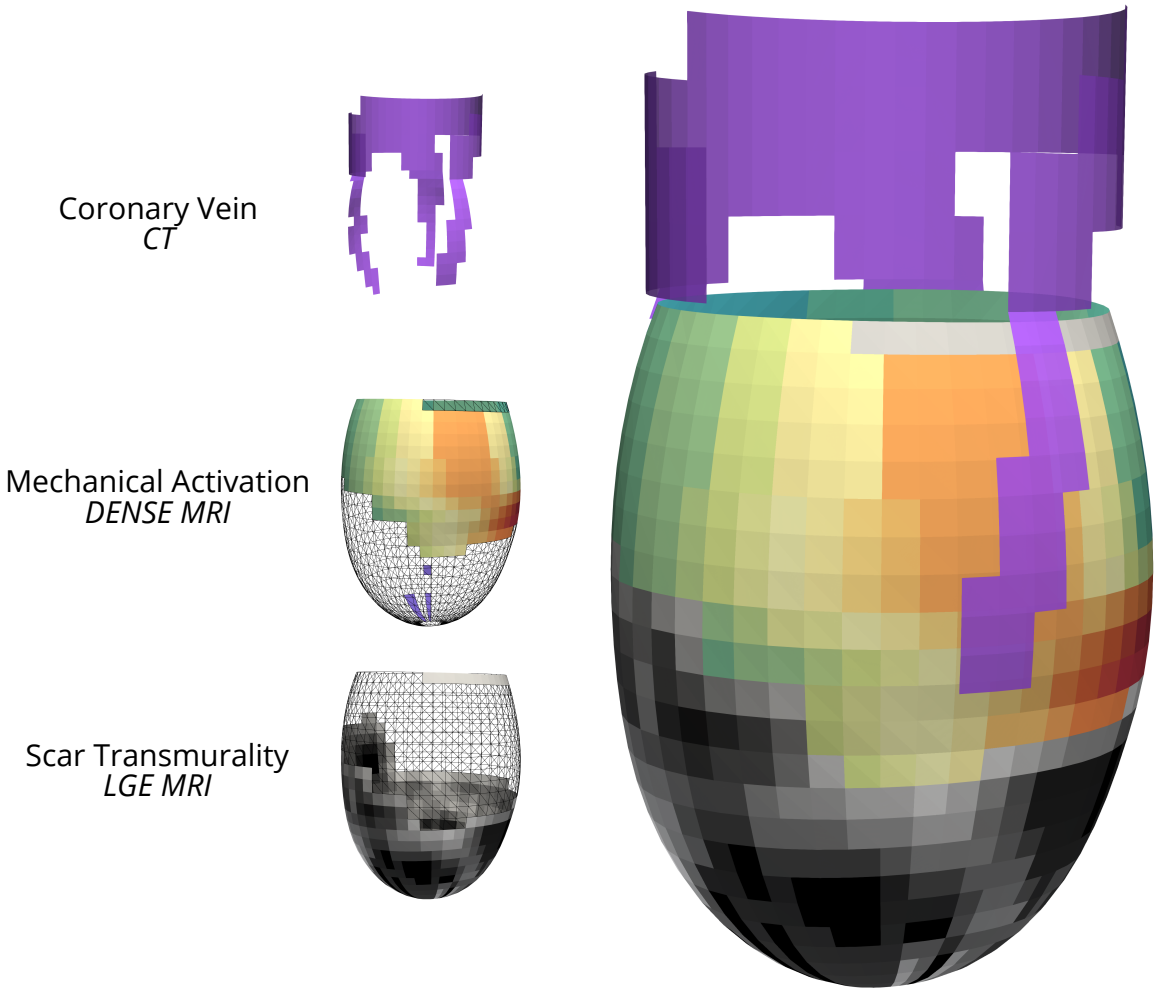

Figure 3.6: Human patient-specific map of coronary vein anatomy from CT, mechanical activation times from DENSE MRI, and scar transmurality from LGE MRI. This data fusion map was generated as a tool for guiding CRT lead placement.

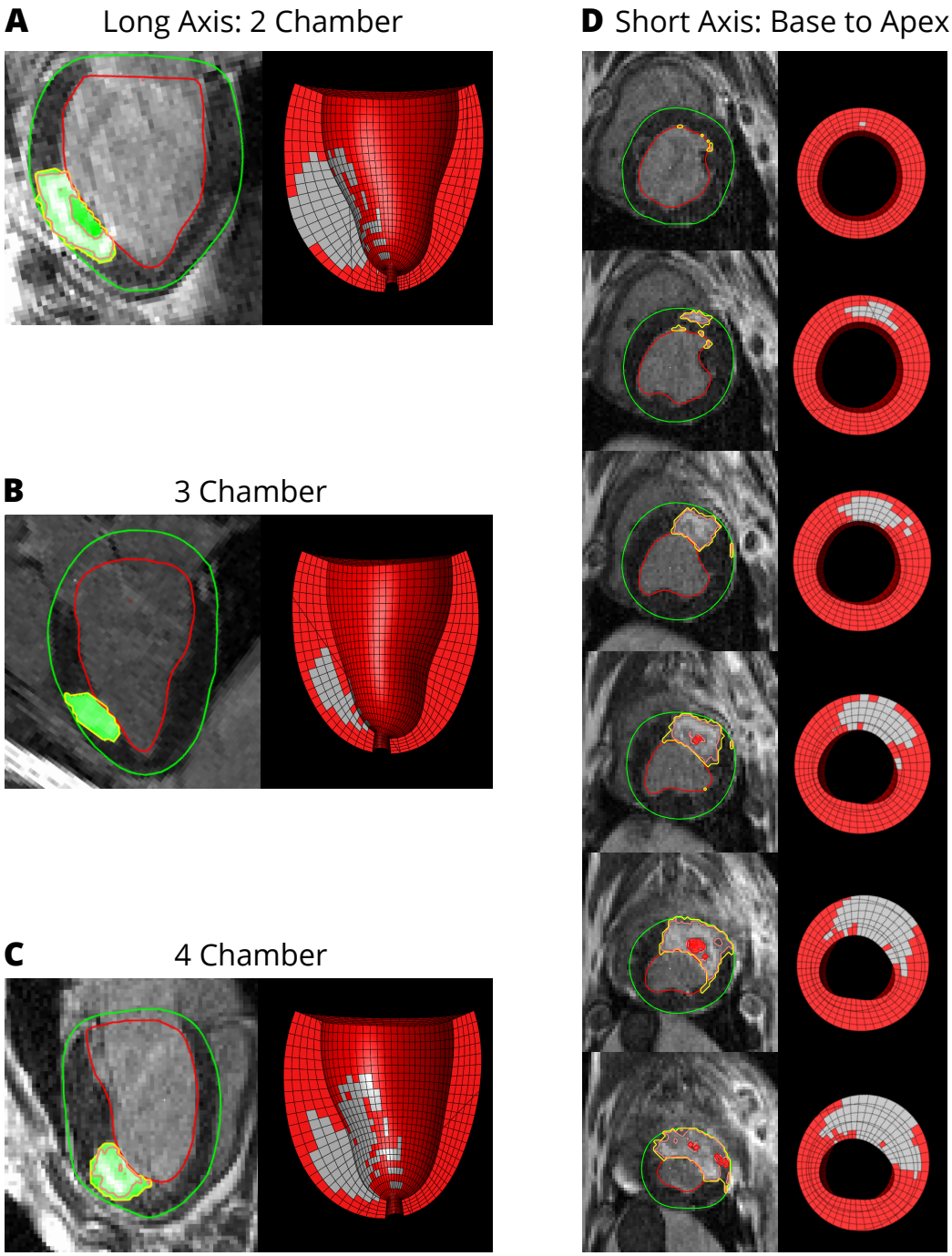

Figure 3.7: Validation of patient-specific scar model. Segmented long (A-C) and short (D) axis LGE MRI planes are shown with corresponding sections through the finite-element model. All voxels enclosed by the yellow segmentation outline are marked as scar. The scar location and volumes in each frame show good agreement with the corresponding MRI images. Note that in general the spatial resolution of the LGE images is lower than of the cine MRI images used to generate the finite-element geometry.

3.3.2 Validation of map guidance in the clinic

The combined coronary vein, mechanical activation times, and scar transmurality map (Fig. 3.6) is currently being used in a randomized clinical trial for pre-procedure CRT planning[§]. Creating a patient-specific map takes about 3 hours, which is mainly limited by the time required for manual geometry segmentation.[14] Currently, 31 patients have been enrolled with favorable results for the map-guided patients.[13] The map-guided patients have LV leads placed in later activated regions compared to control (Fig. 3.8). Post-CRT implantation for each patient was evaluated based on metrics of electrical activation timing. The timing at the LV lead (QLV) is compared to the pre-CRT QRS duration. The change in QRS duration post-CRT is also quantified. Optimal CRT has a QLV to QRS ratio approaching 1 and a decrease in QRS duration post-CRT.

3.4 Discussion

3.4.1 Data fusion

We have presented a method for mapping MRI-derived data on scar location or mechanical activation onto a patient-specific finite-element geometry using prolate spheroidal coordinates. The data fusion routine relies on identifying landmark locations in the LV anatomy in each image set to register the information. The use of prolate spheroidal coordinates allowed us to simplify the mapping of LGE or DENSE data into a two-dimensional interpolation problem along the epicardial surface of the heart (Fig. 3.3). The projection onto the epicardium requires parameterizing the quantities of interest using metrics than can represent an entire transmural column; thus, mapping non-transmural scar presented an interesting challenge. To maintain information on both transmural extent and transmural location, we created separate variables that quantified these two features. The transmurality metric tracked what percentage of the wall was scar, and the depth metric tracked the distance below the epicardium at which the scar began (Fig. 3.4C). These two parameters allowed for reconstruction of the scar in the finite-element model (Fig. 3.4B).

We also demonstrated the methods presented here on datasets from multiple imaging modal-

[§]clinicaltrials.gov/ct2/show/NCT03398369

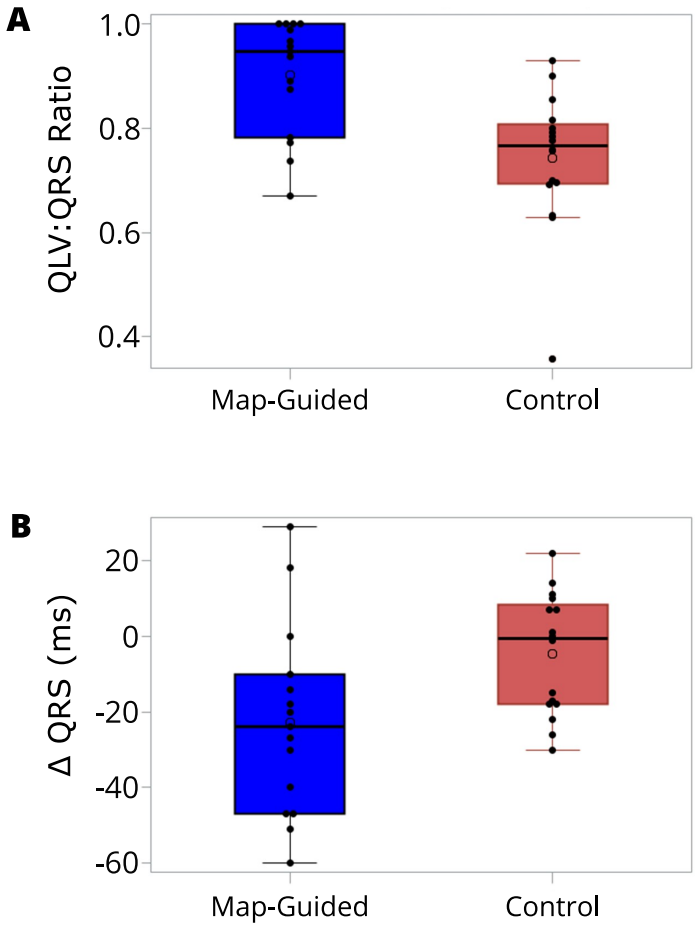

Figure 3.8: Patients ($n = 31$) randomized to MRI guidance (map-guided) for the CRT procedure had superior implant results with respect to LV lead placement and electrical remodeling post-CRT. (A) The time at the LV lead implant site (QLV) approached the latest activation time (QRS) in map-guided patients. QLV:QRS ratio approached 1. (B) QRS duration decreased on map-guided patients versus control patients ($p = 0.02$).

ities including CT and different MRI sequences (Fig. 3.6). Each set of images had different voxel resolutions and gap distances between imaging planes, which we addressed by separately mapping each dataset to the epicardial surface before fusing with the geometry. The sequences provided information at differing numbers of time points during the cardiac cycle, requiring selection of data from similar time points (in this case end diastole) prior to fusion. Furthermore, given the potential for subject motion between sequences and the fact that the anatomy is not identical in the different datasets (due to the differing resolution and slice locations), we also performed a rigid registration step using anatomical landmarks. Registered scar transmurality, mechanical activation, and coronary vein mapping is currently being used in a clinical trial to guide CRT lead placement.

3.4.2 Limitations of data fusion

Because of the relatively low resolution of finite elements through the wall (5 elements from epicardium to endocardium) used here, the representation of scar was discretized to 20% of wall depth bins. Therefore, locations with less than 10% scar transmurality were marked as having no scar due to rounding. This likely accounted for some differences in the observed scar map in comparison to the raw MRI images (Fig. 3.6). However, greater resolution in representing the scar geometry could be achieved either by increasing the number of elements in the finite-element mesh or by employing a mixture formulation for the material properties so that individual elements could be partially composed of scar. Employing a mixture formulation or adding transitional borderzone elements with material properties that are intermediate between scar and muscle could also smooth any stress concentrations that might arise at the infarct border.

The fact that MRI data on scar location are typically available only at discrete slice locations rather than continuously in 3D space also presents a challenge when mapping to a three-dimensional finite-element mesh. Here, we used interpolation to integrate all available data from both long and short axis slices in the LGE MRI dataset, but the accuracy of this approach depends heavily on the number of image slices. We also demonstrated that the mapping techniques presented here can be used for sparser data sets, such as mechanical activation times determined from DENSE MRI (Fig. 3.5).[3] However, in this case estimating mechanical activation values for the entire LV required extrapolation, so the results should be interpreted cautiously in locations beyond the

image slices used to generate the original data.

3.4.3 Open-source code on SimTK

While many previous papers have employed imaging data to generate patient-specific heart models, few have utilized methods that extend easily to fusion of data from multiple MRI sequences or imaging modalities. The most common approach for mapping the location and extent of an infarct onto a model is to identify the infarct using information (such as local wall thickness) segmented from the same images used to construct the model geometry.[15–21] This approach ensures that all information is both represented in the same coordinate system and correctly aligned, avoiding the need for landmark-based registration. In situations where registration is required in order to combine information from different imaging modalities, most groups have placed physical markers such as beads or wire sutures that are visible in multiple imaging modalities.[22–27] For example, Mazhari and coworkers quantified regional strain using radiopaque markers imaged by high-speed x-ray, then used the marker locations to register the mechanics to LV geometry and perfusion boundaries mapped by a 3D manual digitizing probe.[24,25] Another related approach is to register information from different images by identifying physical landmarks that can be aligned using rigid body rotation or probabilistic atlases.[28–30] A small number of papers in this area have used commercial or open-source software packages such as Continuity, CardioViz3D, and ITK-SNAP, making their methods easier for other interested groups to reproduce.[31–34] However, to our knowledge the routines presented here represent the simplest available open-source method for fusing information from multiple imaging sequences or techniques onto a cardiac model geometry.[¶]

3.5 Conclusion- Building patient-specific visuals for guiding CRT

Starting with raw images, the fusion and mapping process outlined here can be completed in less than half an hour by a single, trained operator. The main limitation is the time required to segment the cine and LGE MRI. While the full FE mesh is important for simulating mechanical models, a simpler visualization can be created from the epicardial surface alone (Fig. 3.5B). The

[¶] simtk.org/projects/lvdatamap

simple visualization extends the use of this registration routine from building patient-specific computational models to creating a clinical tool that can superimpose LV data from multiple imaging modalities (Fig. 3.6), which we are currently testing in a randomized, clinical trial[‖].

[‖]clinicaltrials.gov/ct2/show/NCT03398369

References

[1] O. A. Smiseth and J. M. Aalen, "Mechanism of harm from left bundle branch block," *Trends in Cardiovascular Medicine*, vol. 29, pp. 335–342, 8 2019.

[2] L. M. Jaffe and D. P. Morin, "Cardiac resynchronization therapy: history, present status, and future directions.," *The Ochsner journal*, vol. 14, no. 4, pp. 596–607, 2014.

[3] K. C. Bilchick, S. Kuruvilla, Y. S. Hamirani, R. Ramachandran, S. A. Clarke, K. M. Parker, G. J. Stukenborg, P. Mason, J. D. Ferguson, J. R. Moorman, R. Malhotra, J. M. Mangrum, A. E. Darby, J. Dimarco, J. W. Holmes, M. Salerno, C. M. Kramer, and F. H. Epstein, "Impact of mechanical activation, scar, and electrical timing on cardiac resynchronization therapy response and clinical outcomes," *Journal of the American College of Cardiology*, vol. 63, no. 16, pp. 1657–1666, 2014.

[4] D. A. Auger, K. C. Bilchick, J. A. Gonzalez, S. X. Cui, J. W. Holmes, C. M. Kramer, M. Salerno, and F. H. Epstein, "Imaging left-ventricular mechanical activation in heart failure patients using cine DENSE MRI: Validation and implications for cardiac resynchronization therapy," *Journal of Magnetic Resonance Imaging*, pp. 1–10, 2017.

[5] K. C. Bilchick, V. Dimaano, K. C. Wu, R. H. Helm, R. G. Weiss, J. A. Lima, R. D. Berger, G. F. Tomaselli, D. A. Bluemke, H. R. Halperin, T. Abraham, D. A. Kass, and A. C. Lardo, "Cardiac Magnetic Resonance Assessment of Dyssynchrony and Myocardial Scar Predicts Function Class Improvement Following Cardiac Resynchronization Therapy," *JACC: Cardiovascular Imaging*, vol. 1, no. 5, pp. 561–568, 2008.

[6] A. Erdemir, P. J. Hunter, G. A. Holzapfel, L. M. Loew, J. Middleton, C. R. Jacobs, P. Nithiarasu, R. Lohner, G. Wei, B. A. Winkelstein, V. H. Barocas, F. Guilak, J. Ku, J. L. Hicks, S. Delp, M. Sacks, J. A. Weiss, D. G. A. Ateshian, S. A. Maas, A. D. McCulloch, and G. C. Peng, "Perspectives on Sharing Models and Related Resources in Computational Biomechanics Research," *Journal of Biomechanical Engineering*, vol. 140, no. February, pp. 1–11, 2017.

[7] E. Heiberg, J. Sjögren, M. Ugander, M. Carlsson, H. Engblom, and H. Arheden, "Design and validation of Segment - freely available software for cardiovascular image analysis," *BMC Medical Imaging*, vol. 10, pp. 1–13, 2010.

[8] S. A. Maas, B. J. Ellis, G. A. Ateshian, and J. A. Weiss, "FEBio: Finite Elements for Biomechanics," *Journal of Biomechanical Engineering*, vol. 134, no. 1, p. 011005, 2012.

[9] S. L. Herz, C. M. Ingrassia, S. Homma, K. D. Costa, and J. W. Holmes, "Parameterization of left ventricular wall motion for detection of regional ischemia," *Annals of Biomedical Engineering*, vol. 33, no. 7, pp. 912–919, 2005.

[10] P. Hunter and B. Smaill, "The analysis of cardiac function: A continuum approach," *Progress in Biophysics and Molecular Biology*, vol. 52, no. 2, pp. 101–164, 1988.

[11] P. M. Nielsen, I. J. Le Grice, B. H. Smaill, and P. J. Hunter, "Mathematical model of geometry and fibrous structure of the heart.," *The American journal of physiology*, vol. 260, no. 4 Pt 2, pp. 1365–1378, 1991.

[12] H. Engblom, J. Tufvesson, R. Jablonowski, M. Carlsson, A. H. Aletras, P. Hoffmann, A. Jacquier, F. Kober, B. Metzler, D. Erlinge, D. Atar, H. Arheden, and E. Heiberg, "A new automatic algorithm for quantification of myocardial infarction imaged by late gadolinium enhancement cardiovascular magnetic resonance: Experimental validation and comparison to expert delineations in multi-center, multi-vendor patient data," *Journal of Cardiovascular Magnetic Resonance*, vol. 18, no. 1, pp. 1–13, 2016.

[13] K. C. Bilchick, M. Abdishektaei, T.-K. N. Phung, D. A. Auger, X. Gao, R. Malhotra, P. Mason, N. Mehta, A. Darby, M. Mangrum, C. M. Kramer, J. W. Holmes, and F. H. Epstein, "Randomized Clinical Trial of CMR-Guided Cardiac Resynchronization Therapy: Implant Findings," in *SCMR 23rd Annual Scientific Sessions: Transforming Cardiovascular Care Through Discoveries in Imaging*, (Orlando, FL), Society for Cardiovascular Magnetic Resonance, 2020.

[14] T.-K. N. Phung, D. Auger, F. H. Epstein, K. C. Bilchick, and J. W. Holmes, "Registering multimodal MRI to guide patient-specific cardiac resynchronization therapy," in *8th World Congress of Biomechanics*, (Dublin, Ireland), 2018.

[15] N. Cedilnik, J. Duchateau, H. Cochet, M. Sermesant, R. Dubois, F. Sacher, P. Jaïs, H. Cochet, and M. Sermesant, "Fast personalized electrophysiological models from computed tomography images for ventricular tachycardia ablation planning," *EP Europace*, vol. 20, no. suppl_3, pp. iii94–iii101, 2018.

[16] A. B. C. Dang, J. M. Guccione, J. M. Mishell, P. Zhang, A. W. Wallace, R. C. Gorman, J. H. Gorman, and M. B. Ratcliffe, "Akinetic myocardial infarcts must contain contracting myocytes: finite-element model study," *American Journal of Physiology-Heart and Circulatory Physiology*, vol. 288, pp. H1844–H1850, 4 2005.

[17] J. M. Guccione, S. M. Moonly, P. Moustakidis, K. D. Costa, M. J. Moulton, M. B. Ratcliffe, and M. K. Pasque, "Mechanism underlying mechanical dysfunction in the border zone of left ventricular aneurysm: A finite element model study," *Annals of Thoracic Surgery*, vol. 71, no. 2, pp. 654–662, 2001.

[18] K. Sun, N. Stander, C.-S. Jhun, Z. Zhang, T. Suzuki, G.-Y. Wang, M. Saeed, A. W. Wallace, E. E. Tseng, A. J. Baker, D. Saloner, D. R. Einstein, M. B. Ratcliffe, and J. M. Guccione, "A computationally efficient formal optimization of regional myocardial contractility in a sheep with left ventricular aneurysm.," *Journal of biomechanical engineering*, vol. 131, p. 111001, 11 2009.

[19] J. F. Wenk, K. Sun, Z. Zhang, M. Soleimani, L. Ge, D. Saloner, A. W. Wallace, M. B. Ratcliffe, and J. M. Guccione, "Regional Left Ventricular Myocardial Contractility and Stress in a Finite Element Model of Posterobasal Myocardial Infarction," *Journal of Biomechanical Engineering*, vol. 133, no. 4, p. 044501, 2011.

[20] J. F. Wenk, P. Eslami, Z. Zhang, C. Xu, E. Kuhl, J. H. Gorman, J. D. Robb, M. B. Ratcliffe, R. C. Gorman, and J. M. Guccione, "A novel method for quantifying the in-vivo mechanical effect of material injected into a myocardial infarction," *Annals of Thoracic Surgery*, vol. 92, no. 3, pp. 935–941, 2011.

[21] J. White, E. Ukwatta, N. A. Trayanova, E. McVeigh, H. Arevalo, F. Vadakkumpadan, F. Pashakhanloo, A. Prakosa, M. Rajchl, A. C. Lardo, and D. A. Herzka, "Image-based reconstruction of three-dimensional myocardial infarct geometry for patient-specific modeling of cardiac electrophysiology," *Medical Physics*, vol. 42, no. 8, pp. 4579–4590, 2015.

[22] H. Ashikaga, S. R. Mickelsen, D. B. Ennis, I. Rodriguez, P. Kellman, H. Wen, and E. R. McVeigh, "Electromechanical analysis of infact border zone in chronic myocardial infarction," *Am. J. Physiol. Circ. Physiol.*, vol. 289, no. 3, pp. 1099–105, 2005.

[23] O. P. Faris, F. J. Evans, D. B. Ennis, P. A. Helm, J. L. Taylor, A. S. Chesnick, M. A. Guttman, C. Ozturk, and E. R. McVeigh, "Novel technique for cardiac electromechanical mapping with magnetic resonance imaging tagging and an epicardial electrode sock," *Annals of Biomedical Engineering*, vol. 31, no. 4, pp. 430–440, 2003.

[24] R. Mazhari, J. H. Omens, J. W. Covell, and A. D. McCulloch, "Structural basis of regional dysfunction in acutely ischemic myocardium," *Cardiovascular Research*, vol. 47, no. 2, pp. 284–293, 2000.

[25] R. Mazhari, J. H. Omens, L. K. Waldman, and A. D. Mcculloch, "Regional myocardial perfusion and mechanics: A model-based method of analysis," *Annals of Biomedical Engineering*, vol. 26, no. 5, pp. 743–755, 1998.

[26] J. R. McGarvey, D. Mojsejenko, S. M. Dorsey, A. Nikou, J. A. Burdick, J. H. Gorman, B. M. Jackson, J. J. Pilla, R. C. Gorman, and J. F. Wenk, "Temporal Changes in Infarct Material Properties: An In Vivo Assessment Using Magnetic Resonance Imaging and Finite Element Simulations," *Annals of Thoracic Surgery*, vol. 100, no. 2, pp. 582–589, 2015.

[27] D. Mojsejenko, J. R. McGarvey, S. M. Dorsey, J. H. Gorman, J. A. Burdick, J. J. Pilla, R. C. Gorman, and J. F. Wenk, "Estimating passive mechanical properties in a myocardial infarction using MRI and finite element simulations," *Biomechanics and Modeling in Mechanobiology*, vol. 14, no. 3, pp. 633–647, 2015.

[28] R. A. B. Burton, G. Plank, J. E. Schneider, V. Grau, H. Ahammer, S. L. Keeling, J. Lee, N. P. Smith, D. Gavaghan, N. Trayanova, and P. Kohl, "Three-dimensional models of individual cardiac histoanatomy: tools and challenges.," *Annals of the New York Academy of Sciences*, vol. 1080, pp. 301–19, 10 2006.

[29] J. C. Walker, M. B. Ratcliffe, P. Zhang, A. W. Wallace, B. Fata, E. W. Hsu, D. Saloner, and J. M. Guccione, "MRI-based finite-element analysis of left ventricular aneurysm.," *American journal of physiology. Heart and circulatory physiology*, vol. 289, pp. 692–700, 8 2005.

[30] A. Young, B. French, Z. Yang, B. Cowan, W. Gilson, S. Berr, C. Kramer, and F. Epstein, "Reperfused myocardial infarction in mice: 3D mapping of late gadolinium enhancement and strain," *Journal of Cardiovascular Magnetic Resonance*, vol. 8, no. 5, pp. 685–692, 2006.

[31] J. Aguado-Sierra, A. Krishnamurthy, C. Villongco, J. Chuang, E. Howard, M. J. Gonzales, J. Omens, D. E. Krummen, S. Narayan, R. C. P. Kerckhoffs, and A. D. McCulloch, "Patient-specific modeling of dyssynchronous heart failure: A case study," *Progress in Biophysics and Molecular Biology*, vol. 107, no. 1, pp. 147–155, 2011.

[32] A. Krishnamurthy, C. T. Villongco, J. Chuang, L. R. Frank, V. Nigam, E. Belezzuoli, P. Stark, D. E. Krummen, S. Narayan, J. H. Omens, A. D. McCulloch, and R. C. P. Kerckhoffs, "Patient-specific models of cardiac biomechanics," *Journal of Computational Physics*, vol. 244, pp. 4–21, 2013.

[33] M. Sermesant, R. Chabiniok, P. Chinchapatnam, T. Mansi, F. Billet, P. Moireau, J. M. Peyrat, D. Chapelle, R. Razavi, N. Ayache, K. Wong, J. Relan, K. Rhode, M. Ginks, P. Lambiase, H. Delingette, M. Sorine, C. A. Rinaldi, D. Chapelle, R. Razavi, and N. Ayache, "Patient-specific electromechanical models of the heart for the prediction of pacing acute effects in CRT: A preliminary clinical validation," *Medical Image Analysis*, vol. 16, no. 1, pp. 201–215, 2012.

[34] C. T. Villongco, D. E. Krummen, P. Stark, J. H. Omens, and A. D. McCulloch, "Patient-specific modeling of ventricular activation pattern using surface ECG-derived vectorcardiogram in bundle branch block," *Progress in Biophysics and Molecular Biology*, vol. 115, no. 2-3, pp. 305–313, 2014.

4

A fast, tunable electrical model for predicting cardiac resynchronization therapy

4.1 Introduction

4.1.1 Virtual CRT

In Chapter 3, we presented a data fusion routine to map, integrate, and visualize data on multiple factors associated with cardiac resynchronization therapy (CRT) outcomes in order to assist pre-procedure planning.[1] Anticipating CRT efficacy is particularly difficult in patients with scar in the left ventricle (LV) due to complex interactions between the muscle, scar and pacemaker lead.[1,2] While integrating this information into a visual display can help physicians plan CRT lead placement, accurately predicting long-term outcome from specific CRT lead positions in specific patients would be an even more valuable tool for clinical planning. Successful CRT is intended to reduce dilation in the LV volume through remodeling; thus, the most useful predictive model would be one that accurately predicts LV remodeling for various possible choices of lead position.

Computational modeling has emerged as a powerful tool for cardiovascular research. Creating computational representations of the heart's electrical, mechanical, and hemodynamic function has allowed for improved understanding of cardiac physiology.[3–6] Current state-of-the-art computational models typically employ high-resolution 3-D finite-element models with detailed representations of anatomy and electrophysiology; however, the computational cost of these simulations render them intractable for routine clinical use. Additionally, mechanical simulations at this resolution provide excess spatial information that may not be relevant for the clinic. There remains tremendous potential in using lower dimensional models, which require orders of magnitude less computation time.[7,8] With the vast library of computational methods available, strategically matching model complexity to specific problems can help integrate these techniques into the clinic.

In the next two chapters, we present two components of a modeling pipeline, *Virtual CRT*, for predicting long-term outcomes of CRT. In this chapter, we developed a fast, tunable electrical model to simulate patient-specific electrical activation. The model strategically leverages older electrical modeling methods which can be implemented efficiently with current computing resources.

4.1.2 Electrical modeling

Models of electrical activation in the heart have spanned simpler phenomenologic to more complex physiologic representations.[9,10] Based on early work by Hodgkin and Huxley simulating nerve action potentials, the physiologic models simulate a cell's transmembrane potential over time by accounting for specific ion currents (such as sodium and potassium) across the cell membrane.[11] The different models often vary in the number of specific ions represented.[12,13] These models can be simplified using more generic reaction-diffusion models that lump all ion currents together, such as in the Fitzhugh-Nagumo and Mitchell-Schaeffer models.[14–16] These models contain fewer equations, allowing them to be more easily implemented in numerical solvers or analytically solved. Because all of these models compute transmembrane potential, they can also be extended to model spatial propagation of action potentials using cable theory.

By contrast, phenomenologic models of electrical activation simulate the spatial spread of the activation wavefront through the heart without explicitly computing transmembrane potential.

They capture the timing at which electrical signals reach each part of the heart. These models are often implemented using Huygens principle and the eikonal equation describing wave propagation.[17,18] Early phenomenologic models used discrete solving methods such as cellular automata to capture physiologic patterns of electrical activation.[10,19] Although these models were deemed computationally expensive when they were developed in the 70s and 80s, current implementations of these methods can generate electrical predictions in near real time, such as in the software ECGSIM.[20,21]

In clinical settings, electrical information about the heart is recorded using electrocardiogram (ECG) imaging systems. These methods rely on electrical leads to record changes in the electrical activity of the heart. They vary from non-invasive techniques such as standard 12 lead ECG to invasive contact mapping in the heart.[22] While 12 lead ECG relies on 9 electrical leads to generate 12 signals, the number of leads can be significantly increased to achieve higher spatial resolution. In this work, we validated our model using higher resolution ECG data, but we prioritized developing our work using 12 lead ECG because it is most widely used in the clinic.

The goal of the electrical model is to rapidly tune a model to match patient-specific ECG data. We adapted a phenomenologic model of electrical activation and paired it with a simplified, transmembrane potential function to simulate ECG signals. Our implementation was solved using efficient, graph-based pathfinding algorithms to minimize computation time. The resulting electrical activation patterns serves as the input for a mechanical model of the LV.

4.2 Methods

We first present the electrical modeling pipeline for predicting CRT. The pipeline was validated using a human patient-specific data set. We also generated a set of canine subject-specific models to demonstrate clinical use of the pipeline.

4.2.1 Electrical modeling pipeline

The goal of the electrical modeling pipeline is to simulate electrical activation times to inform when the myocardium contracts in a mechanical model described in the next chapter. The electrical model is built using cardiac MRI data. The model is solved in two steps. First, a cellular

automata framework is used to simulate the electrical activation times across the ventricles. Second, the electrical activation times are used to simulate ECG signals. The model is tuned using both steps to generate model ECG signals for comparison to patient-specific ECG data. After tuning the model, only the first step is used to predict new electrical activation times from CRT pacing. A flowchart of the pipeline is laid out in Figure 4.1.

Building a patient-specific model

The electrical model build consists of a biventricular finite-element mesh and material properties describing the conduction in the elements. In this chapter, we have generated models for both human and canine (Fig. 4.2A). The geometry of the finite-element mesh is generated from patient-specific cardiac MRI. The biventricular finite-element mesh is also spatially registered with the location of ECG leads. For patients with scar, elements were labeled as scar using the method described in the previous chapter. Scar elements are excluded from the electrical simulation to represent complete electrical block (examples of mapped scar geometry in Fig. 4.2C).

The material properties in the elements include the myocardial fiber orientation and conduction velocities. The material properties were determined from prior literature. To describe the muscle fiber architecture, we used a rule-based method to assign fibers with orientations varying linearly from 60° on the endocardium to -60° at the epicardium in the plane of the wall as described by Streeter and Hanna (Fig. 4.2B).[23] For each element, the conduction velocities are assigned along the fiber orientation, transmurally through the wall, and in the cross-fiber orientation in the plane of the wall. The heart was divided into a fast, endocardial layer in the right and left ventricles and the remaining bulk myocardium (Fig. 4.2B). Conduction speed was assumed to be transversely anisotropic with faster conduction along the fiber direction and 40% of that velocity in the cross-fiber directions. We specified endocardial fiber velocity to be 600% of the bulk myocardium fiber to model the Purkinje network as a fast conducting layer.[24–28] Absolute conduction velocities are only scaled by changing the bulk myocardium fiber velocity while maintaining the same scaling for the cross-fiber and endocardial fiber velocities as described by Lee et al.[27]

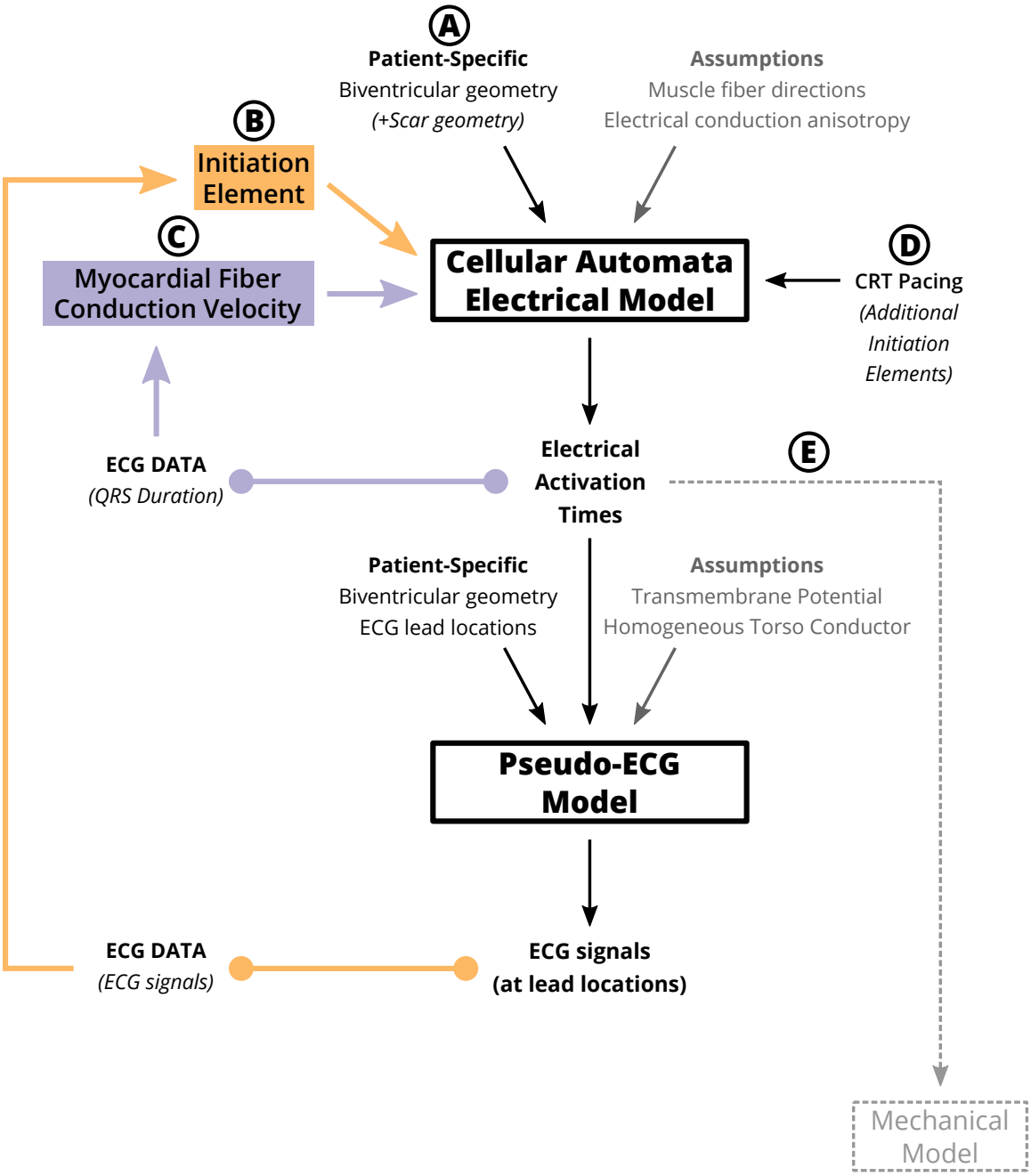

Figure 4.1: Patient-specific electrical modeling pipeline. After building a patient-specific finite-element mesh (A), the electrical initiation element (B) is optimized against patient ECG signals. (C) Then the myocardial fiber conduction velocity is scaled to match the patient's QRS duration. (D) CRT pacing can be incorporated into the model by adding initiation elements. (E) The tuned electrical activation times can be coupled to a mechanical model.

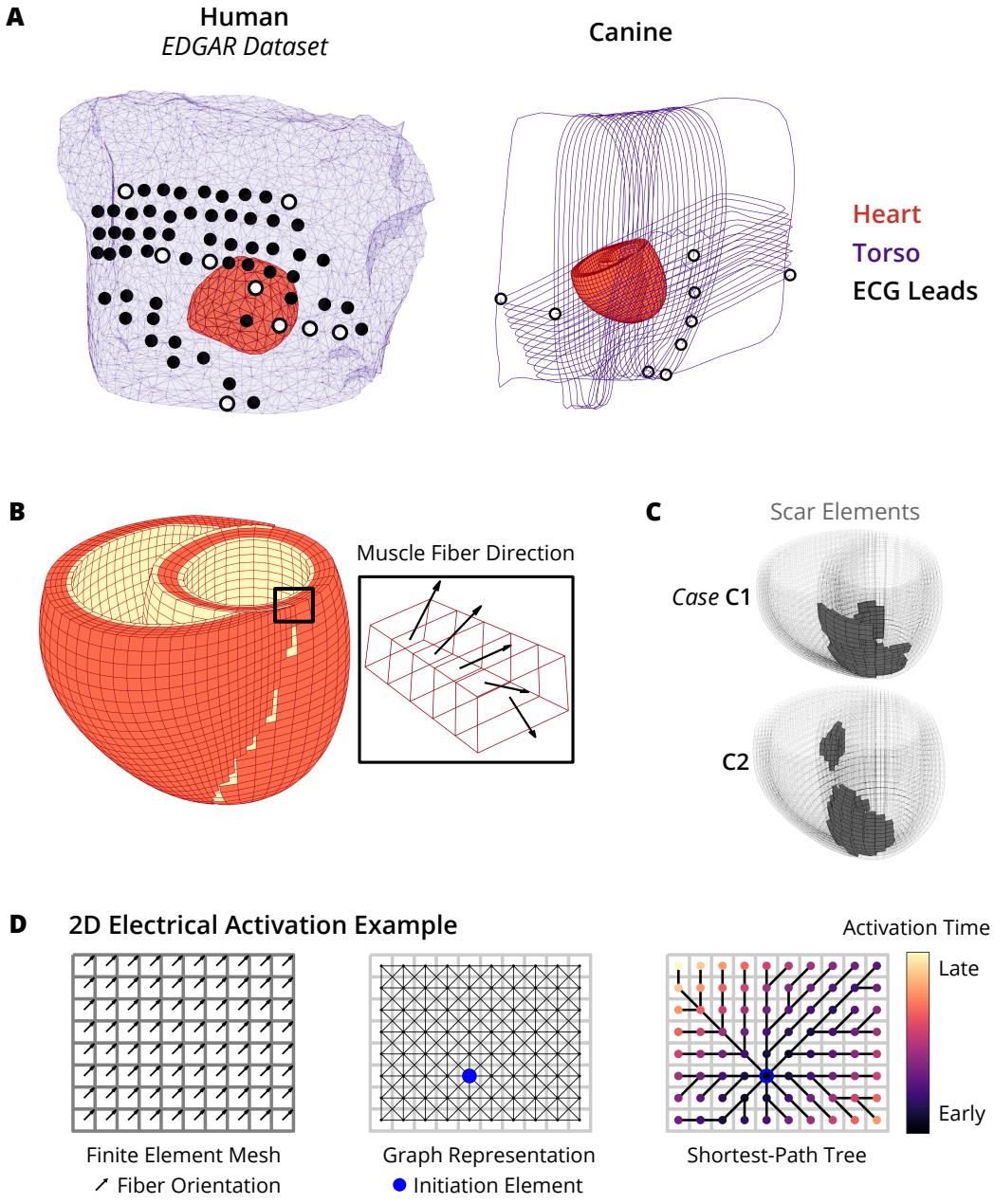

Figure 4.2: Electrical modeling methods. (A) Registered biventricular heart, torso, and electrical leads. The 9 leads used for 12 lead ECG are shown as open black circles. (B) Biventricular geometries were divided into bulk myocardium (red) and fast, endocardial conduction layers (yellow). Transmural muscle fiber directions were assigned using a rule-based method (inset). (C) Two canine models included mapped scar from LGE MRI. (D) A toy model of electrical activation simulating fast conduction along the fiber orientation. The graph representation connects the centers of all elements with its neighbors. A shortest-path tree algorithm was used to solve for the electrical activation times starting from the initiation element.

Model solving algorithm

We implemented a cellular automata model developed by Hunter and Smaill to simulate electrical wavefront propagation.[17] The electrical propagation is simulated by specifying two parameters: an initiation element and a myocardial fiber velocity. The cellular automata modeling framework relies on each element having discrete states, which we specify to be resting or depolarized. The activation starts from a *depolarized* initiation element and spreads to *resting* neighboring elements at a time dependent on the conduction velocities and distances between the elements' centroids. Because we have discretized the geometry into finite elements with defined neighbors (touching elements), we can represent the model as a weighted, undirected graph. The nodes of the graph are the centroids of all elements. The edges are the connections between each element and its neighbors. The weights of the edges are calculated as the time required for the wave front to pass from the centroid of an element to its neighbor. After specifying an initiation element, we can solve the propagation efficiently in MATLAB using a shortest-path tree algorithm emanating from the initiation site. The algorithm connects the initiation node to every other node by traversing the shortest combination of edges. The result of the cellular automata simulation is the electrical activation time for each element in the biventricular mesh. A two-dimensional toy model of the electrical activation algorithm is shown in Figure 4.2D.

To compare the model to recorded ECG data, we generated a unipolar pseudo-ECG ($pECG$) for each specified ECG lead location using equation 4.1.[29] The intracellular conductivity tensor (D_n) was set using the model conduction velocities.[30] The transmembrane potential ($V_{m,n}$) was generated for each element using a Heaviside step function which steps from -90 mV to 0 mV at the cellular automata model electrical activation time. Because we modeled the heart as discrete elements, we can approximate the gradient of the transmembrane potential at each element ($\nabla V_{m,n}$) using the difference in potential with its neighbors.[31] The lead location is represented as a vector between an element and the ECG lead location (r_n), and each element's contribution to the pseudo-ECG is weighted by its volume (v_n). Because the transmembrane potential step function only simulates depolarization, the pseudo-ECG simulates the lead voltage for an equivalent duration to the QRS complex. When comparing pseudo-ECG to recorded ECG, we normalized both signals' ranges to focus on the direction and timing of the deflections rather than the mag-

nitudes.

$$pECG(t) = -\sum_{n}^{Elements} D_n(\nabla V_{m,n}(t) \cdot \frac{\mathrm{I}}{\nabla r_n})v_n \tag{4.1}$$

Tuning a baseline model

The baseline patient-specific electrical model is tuned to simulate depolarization and match recorded ECG data for a QRS complex. The two model parameters (initiation element and myocardial fiber velocity) are tuned using a two-step approach similar to Giffard-Roisin et al.[32] We first optimized the initiation element by brute force. We simulated electrical propagation (and the resulting pseudo-ECG signals) from every endocardial element. For each simulation, correlation coefficient (CC) was calculated between the pseudo-ECG and recorded ECG leads. The average CC across all ECG leads was used as the fitness score for each endocardial initiation element.

Using the best fit initiation element, we then scaled the myocardial fiber velocity to match the latest electrical activation time with the recorded QRS duration. The velocity scaling only affects the absolute timing (and not the deflection or shape) of the pseudo-ECG signals; therefore, scaling the myocardial fiber velocity does not change the result of the initiation element optimization.

Predicting the effect of CRT

The tuned, baseline model simulated a patient's current electrical activation times. To predict the effect of CRT, we introduce additional initiation elements in the model to represent CRT pacing leads. The pacing initiation elements can be coordinated to depolarize at any time with respect to the tuned, baseline initiation element. The CRT electrical model predicts new electrical activation times across the ventricles.

4.2.2 Model validation (EDGAR patient-specific model)

We validated our electrical model pipeline using a benchmark study available on the open-source repository EDGAR* organized by the Consortium for ECG Imaging and the University of Utah.[33]

*edgar.sci.utah.edu

The EDGAR dataset[†] featured a nonischemic patient recorded during a premature ventricular contraction (PVC) ablation procedure. ECG signals from 63 leads were recorded for an intrinsic beat (originating from the PVC site) and 7 paced beats (originating from different LV pacing locations). The data included the patient biventricular geometry and locations of the 63 ECG leads, which were used to build the electrical model (Fig. 4.2A, left), and the PVC and 7 LV pacing locations recorded from an intracardiac CARTO system.

This patient-specific data set included the initiation point of electrical propagation and the resulting ECG signals, which are the input and output of our electrical modeling simulation. We used the data to test the electrical model forwards (without optimization, set the initiation element and simulate the resulting pseudo-ECG) and backwards (with optimization, use ECG data to predict the initiation element). For the electrical modeling pipeline, the backwards simulation will be used for *tuning a baseline model*, and the forwards simulation will be used for *predicting the effect of CRT pacing*.

Comparing cellular automata to Mitchell-Schaeffer electrical model

Using a forward simulation of the intrinsic beat, we evaluated the performance of our model against another published model which used the same EDGAR data. We simulated the intrinsic beat by mapping the PVC location as the initiation element in the finite-element mesh and simulating the electrical activation times and pseudo-ECG signals. The initiation element was mapped as the closest element in the finite-element mesh to the recorded PVC location. Our simulated electrical activation times were compared to results from a more complex Mitchell-Schaeffer electrical model implemented by Giffard-Roisin et al.[15,32] The pseudo-ECG signals were compared to the recorded ECG signals.

Reducing data needed for tuning

Tuning a baseline model involves using recorded ECG to optimize the initiation element (the backwards simulation). Any number of ECG signals (torso leads) can be used to tune the model. We validated the tuning method using high resolution ECG from the EDGAR data. We predicted

[†]This study was performed in a joint research project between the First Department of Medicine (Cardiology), University Medical Centre Mannheim and the Karlsruhe Institute of Technology (KIT).

initiation elements for 8 cases (intrinsic PVC and 7 pacing beats) using ECG signals from 63 torso leads. Then we reduced the ECG resolution by selecting 9 of the 63 ECG signals to represent 12 lead ECG, which is more common in the clinic (Fig. 4.2A, left). We repeated the tuning with the reduced data set. The optimized initiation elements were compared to the recorded initiation points from the intracardiac CARTO system. We calculated the distance between each recorded site and the centroid of its best fit initiation element. We also calculated the distance between the sites and the closest elements in the finite-element mesh to note minimum possible distance (Fig. 4.4a).

Predicting the effect of pacing

We used the modeling pipeline to test pacing simulations. We performed forward simulations of the 7 paced beats by mapping the recorded pacing locations as the initiation elements. The models were not simulated from a tuned baseline, so each simulation only included one initiation element (the pacing location). The 9 ECG leads selected to represent the 12 lead ECG were compared to the simulated pseudo-ECG signals.

4.2.3 Simulating CRT (canine subject-specific models)

We tested the ability of the electrical modeling pipeline to match subject-specific data relevant to CRT. The preoperative CRT state includes LBBB and can include scar for patients with prior myocardial infarction. We simulated 6 preoperative CRT cases collected from a canine study by our group. The canine dataset featured two ischemic and four nonischemic canines recorded during LBBB ablation surgery. 12 lead ECG was recorded before and immediately after ablation of the left bundle branch. Cine and LGE MRI from one week after LBBB surgery were acquired to provide the biventricular and scar geometries, respectively. Exact locations of the ECG leads were not recorded during LBBB surgery; therefore, the 9 electrode locations from 12 lead ECG were approximated on the torso geometry obtained from Cine MRI (Fig. 4.2A, right). We used the electrical modeling pipeline to simulate the healthy and LBBB states for each subject. We then used the tuned LBBB models (the baseline state pre-CRT) to simulate CRT pacing.

Simulating pre-CRT subjects

To test the model representation of scar, we used the backwards simulations to tune the 2 ischemic subject-specific models (Fig. 4.2C) in their healthy state (normal conduction with myocardial infarction scar). We also tuned the 4 non-ischemic subjects in their healthy state. All 6 subject-specific models were additionally tuned in their LBBB states. The pseudo-ECG signals from the healthy and LBBB states were compared to the recorded 12 lead ECG. The CC of each lead was compared across all simulations.

Simulating CRT

As a proof-of-concept for simulating CRT, one ischemic subject and one non-ischemic subject were used to simulate CRT. Two pacing initiation elements were added at the RV apex and LV lateral wall to their tuned pre-CRT (LBBB state) models to represent CRT biventricular pacing leads. The two pacing initiation elements and the tuned intrinsic initiation element were simultaneously initiated in a forward simulation to predict the resulting electrical activation times.

4.3 Results

4.3.1 Model validation

We validated the electrical modeling pipeline (Fig. 4.1) using the EDGAR human data set. We first used a forward (without optimization) simulation of the intrinsic (originating from the PVC site) heart beat to compare the cellular automata electrical model to the Mitchell-Schaeffer electrical model implemented by Giffard-Roisin et al.[32] The pattern of electrical activation times matched the trends in the more complex Mitchell-Schaeffer model (Fig. 4.3A). In particular, the earliest and latest activation regions agreed between the models. We compared the simulated pseudo-ECG signals for 9 lead locations to the recorded ECG (Fig. 4.3B). The deflections in signals matched in most leads.

We then tested the model tuning (backwards simulation) using the intrinsic (PVC) and 7 LV paced cases. Each case was tuned using the entire set of 63 ECG leads as well as a reduced set of 9 leads. The model tuning optimizes the initiation element and scales the myocardial fiber con-

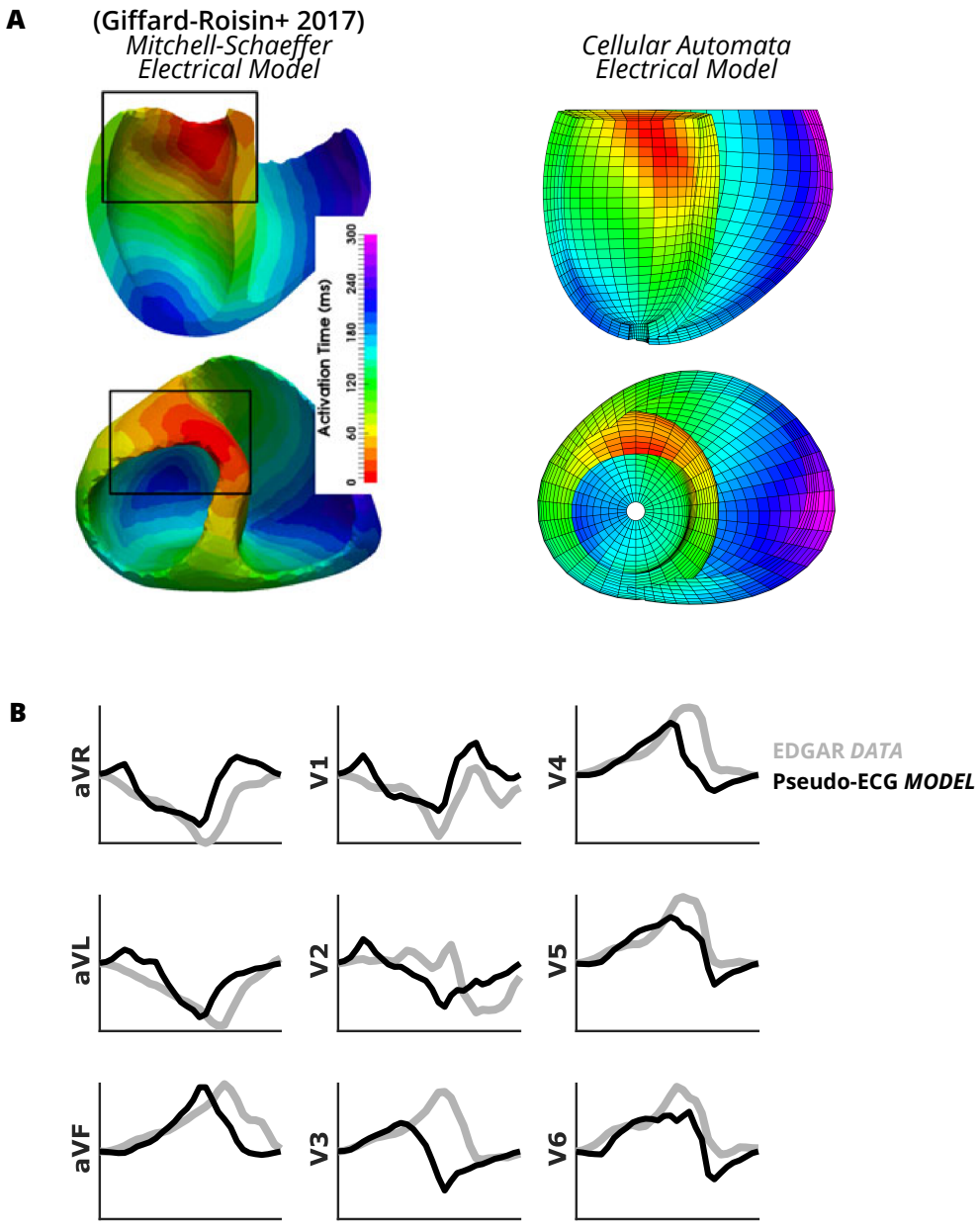

Figure 4.3: Simulating an intrinsic patient heart beat initiation from a recorded PVC site. (A) Comparison of cellular automata electrical model to Mitchell-Schaeffer model implemented by Giffard-Roisin et al.[32] (B) 9 leads were compared to the recorded ECG signals. The simulated pseudo-ECG signals matched the deflections in most leads.

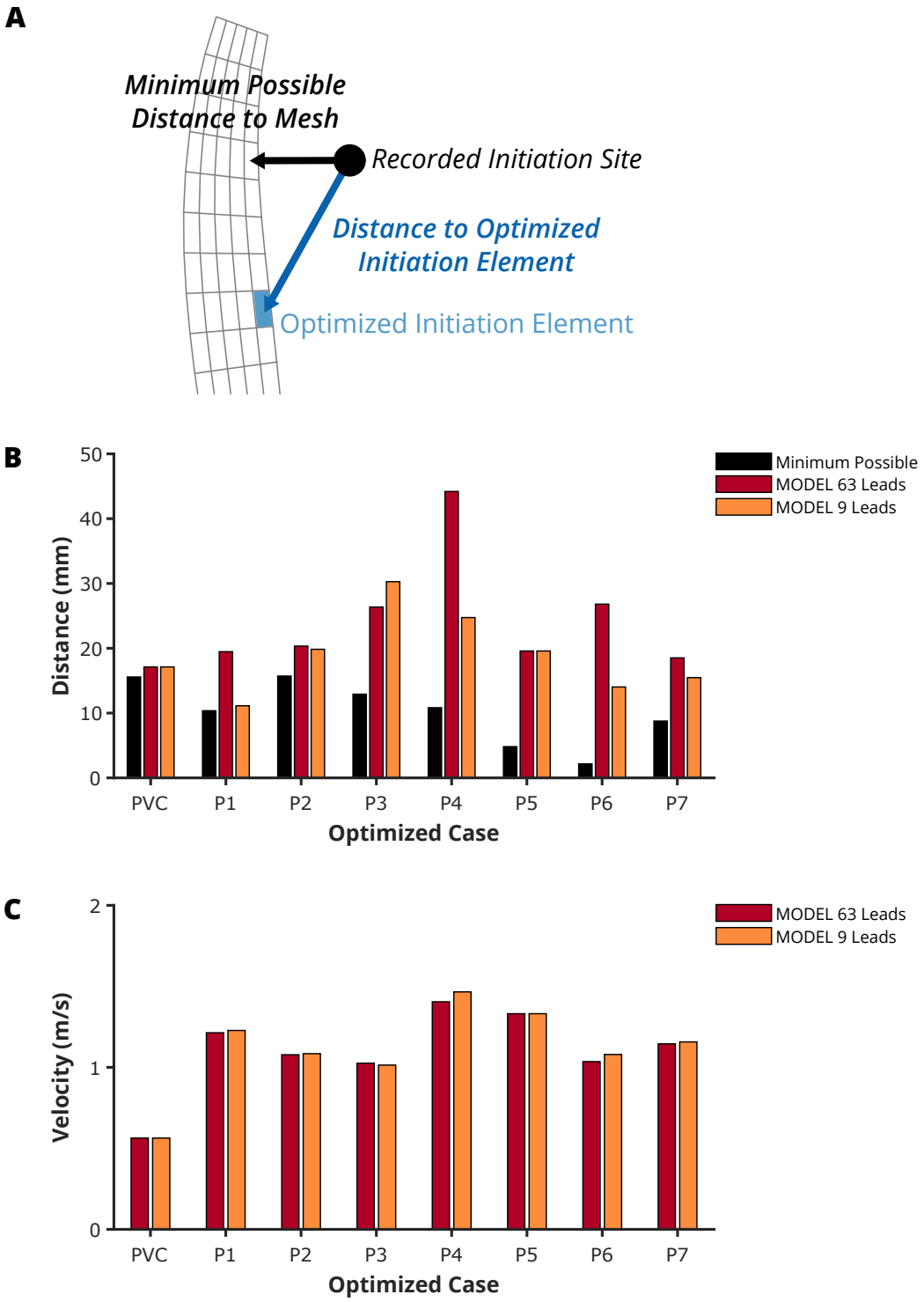

Figure 4.4: EDGAR data 63 lead and 9 lead optimization results. (A) Example diagram of distance metric between a recorded initiation site from CARTO and the finite-element mesh. (B) Summary of the distances for PVC and 7 paced heart beats including the minimum possible distance to mesh and distance to optimized initiation elements for the 63 and 9 lead optimizations. (C) The scaled myocardium fiber velocity for each case was similar between 63 lead and 9 lead optimizations.

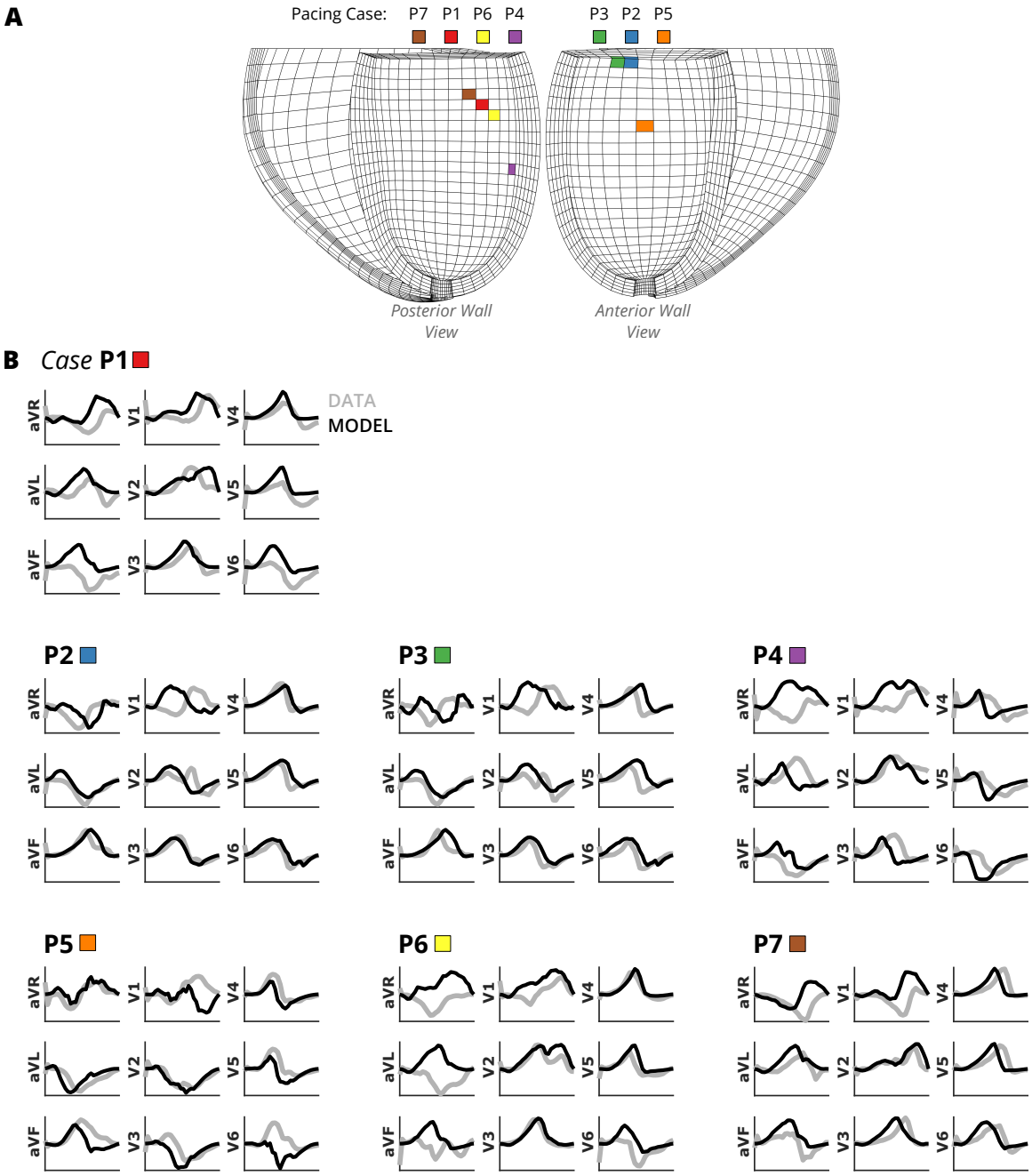

Figure 4.5: Simulating LV pacing based on recorded pacing locations. (A) For each case, the pacing location was registered to the finite-element mesh. (B) The simulated pseudo-ECG for 9 leads in each case matched the deflections in recorded ECG signals.

duction velocity. We compared the optimized initiation element for each case by calculating its distance to the recorded initiation site (Fig. 4.4A). The average minimum possible distance was 10±5 mm. For all cases except P3, reducing data from 63 to 9 leads maintained or improved the selection of the optimized initiation element (Fig. 4.4B). Improvement in optimized initiation element is marked by a decrease in distance to the recorded initiation site. While the optimized conduction velocity among the intrinsic and pacing cases varied, the 63 lead and 9 lead optimizations resulted in similar velocities for each case (Fig. 4.4C).

Lastly, we used the forward simulation to test the electrical modeling pipeline predictions for LV pacing. For each case, the pacing location was registered to the finite-element mesh (Fig. 4.5A). We compared the deflections in simulated pseudo-ECG at 9 ECG leads to recorded ECG signals (Fig. 4.5B). The majority of pseudo-ECG deflections matched the trends in the data.

4.3.2 Simulating CRT

To demonstrate the clinical usage of the electrical modeling pipeline, we simulated 6 canine subject-specific models. We tuned the models using their subject-specific ECG data from a healthy state and LBBB state. Two models included myocardial infarction scar, cases C1 and C2 (Fig. 4.2C). For each case, the optimized initiation elements were different between healthy and LBBB. Additionally, the optimized bulk myocardium fiber velocity was lower in LBBB (1.6±0.2 m/s in healthy and 0.7±0.1 m/s in LBBB). The resulting pseudo-ECG from all optimizations are shown in Figure 4.6A. We calculated CC between the recorded ECG signal and simulated pseudo-ECG to evaluate the fit (Fig. 4.6B). The healthy state optimizations had overall higher CC compared to LBBB. Importantly, there was no major differences in the CC between the subjects with and without scar.

The electrical activation time maps for each subject-specific model are shown in Figure 4.7. Most LBBB models featured delayed activation times towards the posterior and lateral walls of the LV. As a proof-of-concept for simulating CRT pacing, we added biventricular pacing to two cases, C1 and C6 (Fig. 4.8). The pacing simulations decreased the QRS durations compared to the LBBB simulations. A difference map of electrical activation times revealed the lateral wall in both cases became activated earlier, demonstrating the benefit of pacing (Fig. 4.8B).

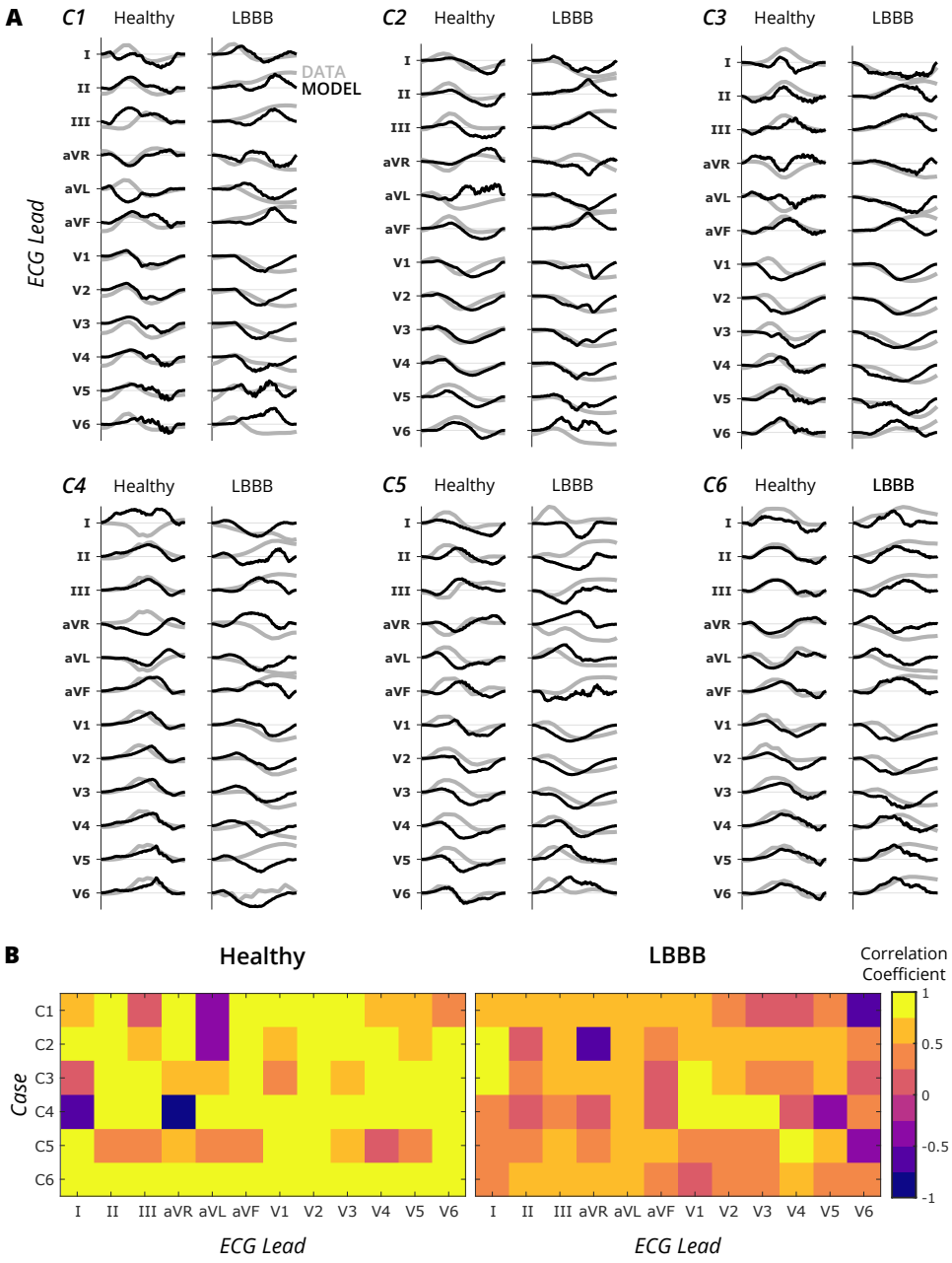

Figure 4.6: Results from 6 subject-specific optimizations. (A) Simulated pseudo-ECG signals for healthy and left bundle branch block optimizations compared to recorded 12 lead ECG data. (B) Correlation coefficient between model and data for each lead in each simulation.

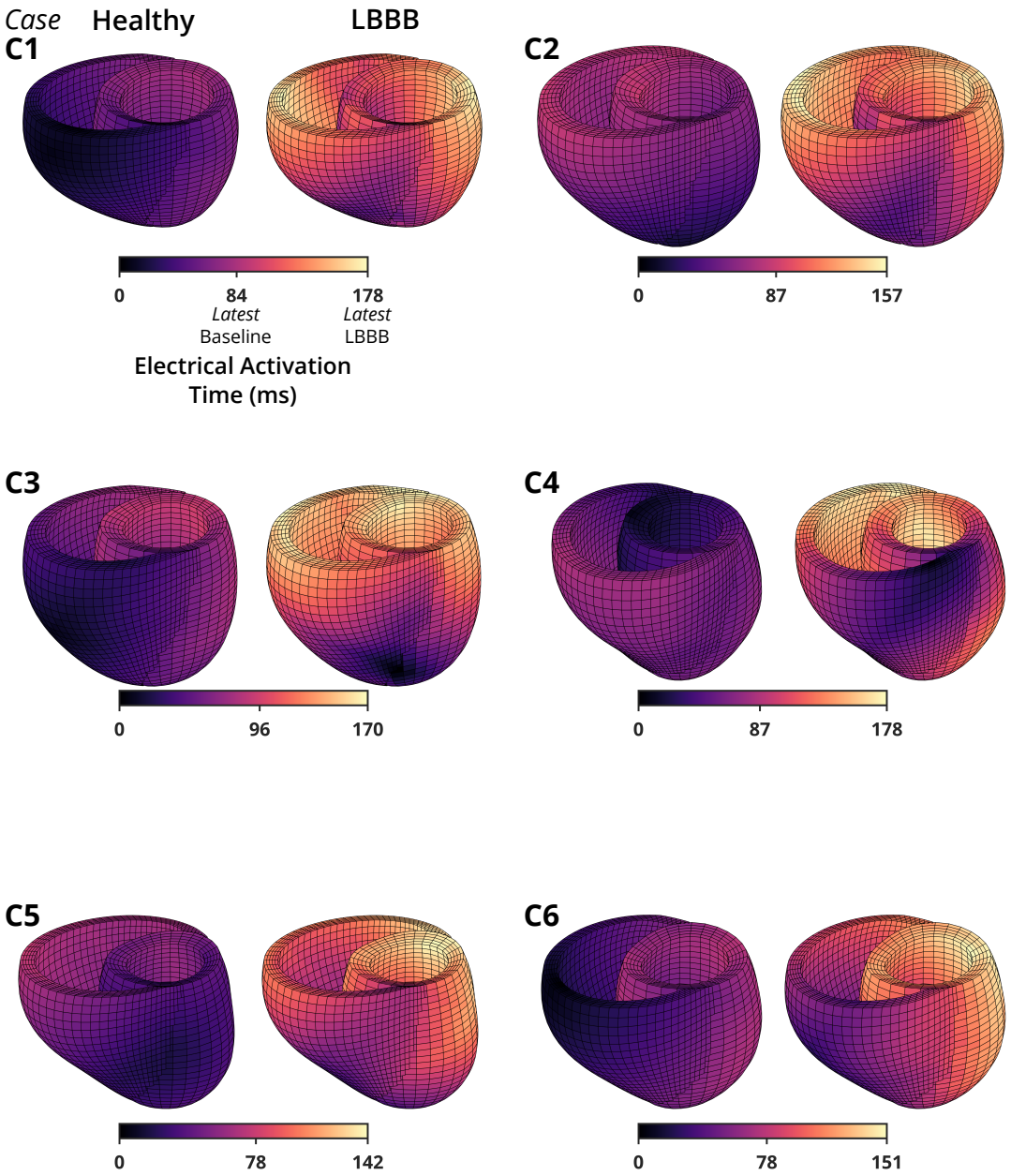

Figure 4.7: Optimized electrical activation time maps for 6 subject-specific models of a healthy heart and left bundle branch block. For each case, the color bar ticks indicate the latest activation time in the healthy and LBBB models, respectively.

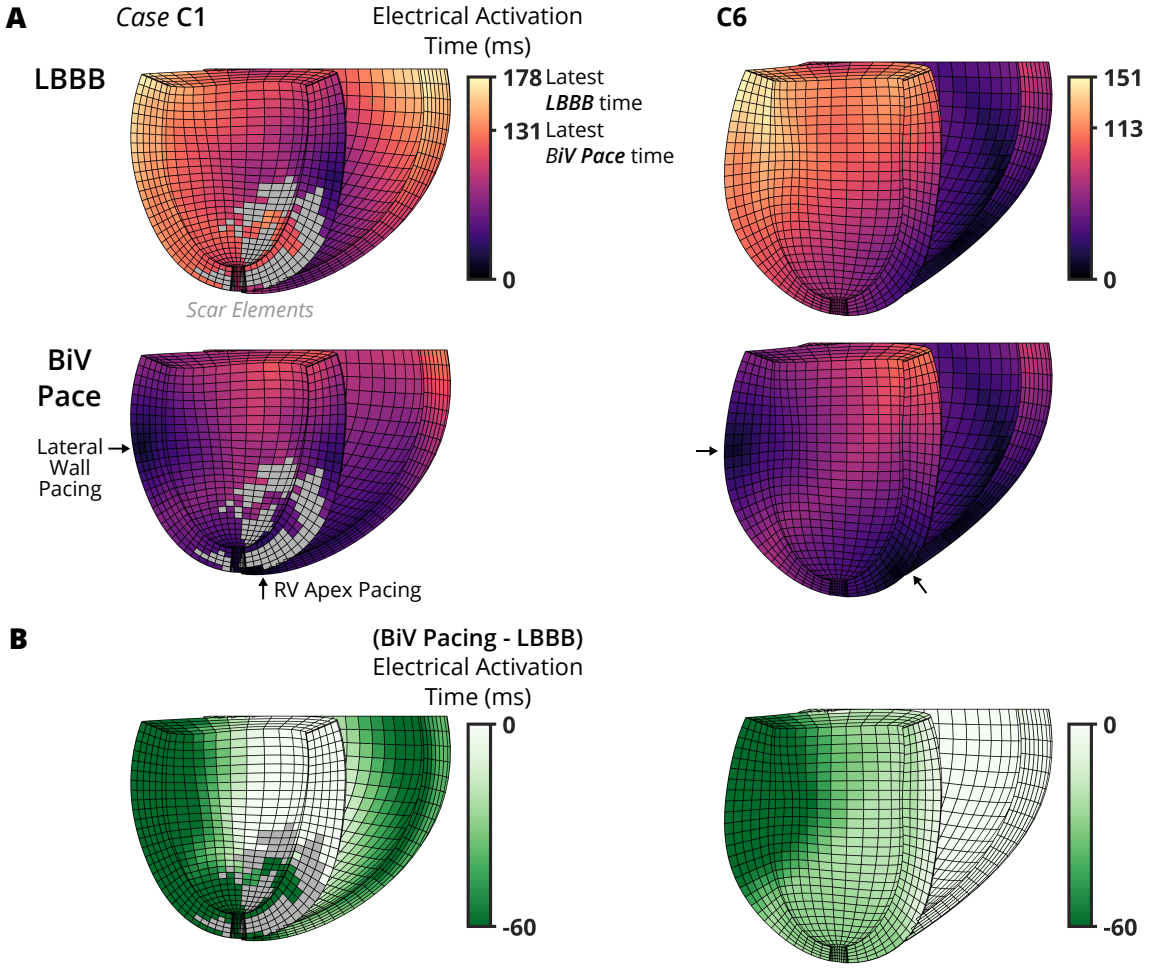

Figure 4.8: Simulating biventricular pacing for CRT in cases C1 and C6. The models show a cross-sectional view of the heart with a view of the LV anterior wall. (A) The baseline (LBBB state) and CRT (BiV Pacing) electrical activation times are shown with arrows indicating the biventricular pacing locations. The latest activation time (simulated QRS duration) for baseline and CRT are indicated as ticks on the color bar. (B) The difference in electrical activation times between pacing and LBBB reveal the regions that were affected by pacing.

4.4 Discussion

Developing a coupled electro-mechanical model of the LV is an essential step for predicting long-term outcomes of CRT. The electrical model is used to predict changes in electrical activation from different CRT pacing lead configurations. In this chapter, we adapted a simple but computationally efficient electrical model to simulate CRT. We validated the model against a more computationally and physiologically complex electrical model by simulating a human patient-specific data set from an open-source repository. We then simulated 6 canine subject-specific models with conditions more similar to preoperative CRT patients.

4.4.1 Model validation

To validate our implementation of a cellular automata electrical modeling framework, we compared our model to a more physiologic simulation implemented by Giffard-Roisin et al (Fig. 4.3A).[32] Their model used benchmark data from EDGAR that included an estimate of the electrical initiation point in the heart (from PVC or pacing leads) and the subsequent electrical signals recorded from multiple ECG leads.[33] Giffard-Roisin et al used the data set to tune and validate their implementation of a Mitchell-Schaeffer electrical model.[32] The major difference between our methods was the calculation of the transmembrane potential. The Giffard-Roisin simulation accounted for the evolution of transmembrane potential at all nodes in their finite-element mesh based on a lumped parameter, reaction-diffusion equation developed by Mitchell and Schaeffer.[15] Their model was solved using finite-element methods.[32] The cellular automata framework simulated electrical activation propagation across the finite-element mesh and assigned a transmembrane potential based on a simple step function. Our model was solved using a shortest-path tree algorithm.

We simulated the intrinsic PVC beat in the cellular automata model by mapping the recorded initiation point onto the finite-element mesh and propagating electrical activation. The resulting electrical activation times matched trends from the equivalent simulation in the Mitchell-Schaeffer model (Fig. 4.3A). Importantly, the earliest and latest activation regions matched. The electrical activation timing directly influences the mechanics of the heart; therefore, matching these regions is essential for accurately coupling the electrical modeling results to a mechanical

model. Also, identifying regional differences in electrical (and mechanical) activation timing is critical for planning CRT.[1] Additionally, our transmembrane potential and pseudo-ECG formulations captured the deflections present in the recorded ECG (Fig. 4.3B). Compared to the Mitchell-Schaeffer model which used a finite-element solver, our cellular automata model solved in near real-time making it more tractable for clinical use. Also, our simplification of the transmembrane potential (represented by a step function compared to the Mitchell-Schaeffer reaction-diffusion equation) still captured the necessary dynamics to simulate deflections in the pseudo-ECG. Overall, our electrical modeling pipeline is a suitable, faster alternative to the Mitchell-Schaeffer electrical model for simulating electrical activation times and ECG signals.

After validating the ability of the electrical modeling pipeline to simulate a patient-specific heart beat, we reversed the simulation to test if we could use ECG data with the model to predict the initiation site. We optimized 8 cases (PVC and 7 LV pacing) to predict their initiation site and myocardial fiber velocity (Fig. 4.4). We optimized each case twice using the entire data set of 63 ECG leads and a reduced set of 9 leads to reflect 12 lead ECG more commonly used in the clinic. Surprisingly, 6 of the 8 cases maintained or improved their distance error metric when the ECG data was reduced (Fig. 4.4B). This may be due to the concentration of the ECG leads on the front of the human torso geometry (Fig. 4.2A, all circles). The formulation for the pseudo-ECG in equation 4.1 relied on the location of the lead; therefore, closely clustered leads will have similar pseudo-ECG signals. Because the optimizations weight each ECG signal equally, this biases optimizations where there are many ECG leads located close together. The locations of the subset of 9 ECG leads are more strategically spaced around the heart allowing for a closer fit to the recorded initiation points.

While the scaled conduction velocities varied between different cases (Fig. 4.4C), these values fell within a physiologic range reported by previous simulations (0.65 to 1.5 m/s along the myocardial fiber velocity).[3,17,25,34,35] Because we assumed the conduction anisotropy in the heart based on work by Lee et al, scaling of the myocardial fiber velocity did not change the regional pattern of early and late electrical activation.[27] Demonstrated in these 8 optimized cases, our electrical modeling pipeline can uniquely identify a site of electrical initiation based on ECG data from 9 recorded leads. This optimization method is important as it will be used to tune a baseline model before predicting electrical activation changes with CRT.

Using the 7 pacing cases, we lastly tested the model's ability to simulate pacing from different locations. We mapped the recorded pacing site onto the finite-element mesh as the initiation elements (Fig. 4.5A). The mapping error between the recorded sites and initiation elements is the minimum possible distance shown in Figure 4.4B. These pacing cases did not feature intrinsic conduction, so the simulations only had electrical propagation from the mapped initiation element. The resulting pseudo-ECG at 9 leads is shown in Figure 4.5B. For all cases, the majority of pseudo-ECG signals matched the deflection observed in the recorded data. This was a promising result because it shows that the model can capture different ECG signals associated with pacing from different locations.

4.4.2 Simulating CRT

We deployed the cellular automata electrical model to simulate 6 subject-specific, canine models. Two cases (C1 and C2) tested modeling of myocardial infarction scar based on LGE MRI (Fig. 4.2C). The registered scar elements in the finite-element mesh were excluded from the electrical propagation to simulate complete electrical block.[31] The presence of scar has been shown to be an important factor in determining CRT response and chronic outcomes; therefore, the ability to accurately simulate the effect of scar on electrical propagation is essential.[1] For each subject-specific model, a single initiation element was optimized to match either the healthy or LBBB state. Although the healthy and LBBB data were recorded sequentially during the left bundle branch ablation procedure, we independently optimized the two states. Clinically, only the LBBB state data will be available for preoperative CRT planning.

Because we do not have a recorded initiation site for electrical activation like the EDGAR data, the models were evaluated by their optimized best fit to the recorded ECG signals. For all simulations, the pseudo-ECG is plotted against the recorded ECG in Figure 4.6. The healthy models overall featured higher correlation coefficients compared to the LBBB models (Fig. 4.6B); however, most leads matched deflections in the data. The simulations with scar (C1 and C2) did not feature any major differences in fit to ECG data compared to the nonischemic cases, and their LBBB simulations represent a frequent preoperative state for many patients receiving CRT.[1,36] One way to possibly improve the lead fits is the use of multiple initiation elements; however, the choice of a single initiation element for each model and condition was consistent with the

methods used by the Giffard-Roisin simulations of EDGAR data.[32]

LBBB patients experience delayed electrical activation and mechanical contraction in the posterior-lateral walls of the LV.[36,37] The activation times for LBBB models featured delayed activation in these regions (Fig. 4.7). To match the late activation time (QRS duration), the myocardial fiber velocity was slowed in all models from healthy (1.6±0.2 m/s) to LBBB (0.7±0.1 m/s). An alternative approach to simulating LBBB includes slowing of the fast endocardial layer conduction velocities in the LV. Lee et al simulated slowing of the basal two-thirds of the LV endocardial layer to match bulk myocardium speeds and showed no significant changes in the location of the simulated and measured late activation time.[27] Additionally, slowing of the LV endocardial layer would prevent retrograde activation of the LV Purkinje which has been clinically observed and simulated in models of CRT.[38,39]

To predict changes in electrical activation associated with CRT, we can take a tuned baseline model and add initiation elements to represent pacing leads. In two cases (ischemic C1 and nonischemic C6), we used the tuned LBBB model to simulate biventricular (BiV) pacing (Fig. 4.8). The two pacing locations were added at the epicardium of the LV lateral wall and the endocardium of the RV apex. They were simultaneously initiated with the tuned LBBB initiation element. We calculated a difference map between the LBBB and BiV paced electrical activation times to show the impact of pacing (Fig. 4.8B). The pacing decreased the simulated QRS durations by more than 25% in both cases.

4.4.3 Computational cost of electrical modeling pipeline

The patient-specific electrical modeling pipeline in this chapter was developed starting from the simplest methods available to minimize computational costs. On a desktop with 4 cores, a cellular automata model simulating depolarization (at most 178 ms) computes in about 50 ms, and the pseudo-ECG calculation for 9 lead locations takes about 1.7 seconds. In comparison, the Mitchell-Schaeffer model simulated 300 ms of the cardiac cycle with a computation time of 2 min using a GPU implementation.[32] And in the most state-of-the-art frameworks, the high-resolution model by Arevalo et al simulated multiple cardiac cycles with a computation time of about 1 hour for each second of the simulation on a supercomputer.[40] While simulating other phases of the cardiac cycle (beyond depolarization) are important for predicting electrical abnormalities, we only

needed to predict depolarization to couple to mechanical contraction of the heart. Furthermore, our fast electrical model is also capable of being rapidly tuned (by running multiple model optimizations) due to its computational efficiency.

In the current pipeline, we used brute force optimization to tune the initiation element simulating propagation from over 2,500 possible endocardial elements, which required a computation time of over 80 minutes. Using a more strategic optimization scheme can greatly reduce the search space and speed up the computation time required to tune a baseline model. From a tuned model, a simulation of CRT pacing can be computed in less than 2 seconds. Overall, the electrical modeling pipeline we developed can be rapidly tuned to match a patient's baseline electrical activation state and screen potential CRT pacing configurations. The pipeline is a promising method for predicting changes in electrical activation times relevant for predicting CRT outcomes.

4.4.4 Limitations

The electrical model that we have developed is limited spatially and temporally in simulation interpretation compared to current state-of-the-art models. The cellular automata method can work on any sized mesh; however, we discretized the heart to solve at about 9000 points with an average resolution of 4±1.5 mm. The goal of the cellular automata model was to predict the timing of electrical activation for different regions to inform mechanical contraction. Although our mesh resolution was low, it appropriately matched the resolution of the geometry generated from cine MRI and the mechanical data from DENSE MRI. In comparison, the range of solving points can vary from 65,000 points in the Giffard-Roisin model to more than 40 million points featuring a resolution of 200 to 350 μm developed by Arevalo et al.[32,40–42] While our low-resolution model was able to make similar predictions to the Giffard-Roisin model regarding electrical activation time, it is not capable of simulating re-entrant arrhythmias possible in the high-resolution models. However, this fundamental limitation does not hinder the applicability of our electrical modeling pipeline towards predicting CRT outcomes.

4.5 Conclusion- Predictive electrical modeling for CRT

The electrical modeling pipeline in this chapter is the first step in the *Virtual CRT* pipeline to model long-term outcomes of CRT. Using a human patient-specific data set featuring PVC, we validated the pipeline's ability to match patient-specific ECG data and simulate LV pacing. Additionally, we tuned 6 canine subject-specific models to data from a pre-CRT state featuring LBBB (and myocardial infarction scar in two subjects). To fully validate the electrical modeling pipeline, we will need a data set which includes multiple pacing lead locations and the resulting ECG in a pre-CRT patient. Invasive contact mapping of electrical activation times could also help validate the electrical activation time predictions simulated from the model. In the next chapter, we build the next step of *Virtual CRT* by coupling the electrical activation times from the tuned LBBB subject-specific models to inform a mechanical model.

References

[1] K. C. Bilchick, S. Kuruvilla, Y. S. Hamirani, R. Ramachandran, S. A. Clarke, K. M. Parker, G. J. Stukenborg, P. Mason, J. D. Ferguson, J. R. Moorman, R. Malhotra, J. M. Mangrum, A. E. Darby, J. Dimarco, J. W. Holmes, M. Salerno, C. M. Kramer, and F. H. Epstein, "Impact of mechanical activation, scar, and electrical timing on cardiac resynchronization therapy response and clinical outcomes," *Journal of the American College of Cardiology*, vol. 63, no. 16, pp. 1657–1666, 2014.

[2] G. B. Bleeker, T. A. Kaandorp, H. J. Lamb, E. Boersma, P. Steendijk, A. de Roos, E. E. van der Wall, M. J. Schalij, and J. J. Bax, "Effect of Posterolateral Scar Tissue on Clinical and Echocardiographic Improvement After Cardiac Resynchronization Therapy," *Circulation*, vol. 113, no. 7, 2006.

[3] R. C. P. Kerckhoffs, P. H. M. Bovendeerd, J. C. S. Kotte, F. W. Prinzen, K. Smits, and T. Arts, "Homogeneity of cardiac contraction despite physiological asynchrony of depolarization: A model study," *Annals of Biomedical Engineering*, vol. 31, no. 5, pp. 536–547, 2003.

[4] C. B. Moyer, P. a. Helm, C. J. Clarke, L. P. Budge, C. M. Kramer, J. D. Ferguson, P. T. Norton, and J. W. Holmes, "Wall-motion based analysis of global and regional left atrial mechanics," *IEEE Transactions on Medical Imaging*, vol. 32, no. 10, pp. 1765–1776, 2013.

[5] K. Sunagawa, W. L. Maughan, and K. Sagawa, "Effect of regional ischemia on the left ventricular end-systolic pressure-volume relationship of isolated canine hearts," *Circ Res*, vol. 52, no. 2, pp. 170–178, 1983.

[6] N. A. Trayanova, T. O'Hara, J. D. Bayer, P. M. Boyle, K. S. McDowell, J. Constantino, H. J. Arevalo, Y. Hu, and F. Vadakkumpadan, "Computational cardiology: How computer simulations could be used to develop new therapies and advance existing ones," *Europace*, vol. 14, no. SUPPL. 5, pp. 82–89, 2012.

[7] J. W. Holmes and J. Lumens, "Clinical Applications of Patient-Specific Models: The Case for a Simple Approach," *Journal of Cardiovascular Translational Research*, vol. 11, pp. 71–79, 4 2018.

[8] C. M. Witzenburg and J. W. Holmes, "Predicting the Time Course of Ventricular Dilation and Thickening Using a Rapid Compartmental Model," *Journal of Cardiovascular Translational Research*, vol. 11, pp. 109–122, 4 2018.

[9] S. Alonso, M. Bar, B. Echebarria, M. Bär, and B. Echebarria, "Nonlinear physics of electrical wave propagation in the heart: a review," *Reports on Progress in Physics*, vol. 79, p. 096601, 9 2016.

[10] R. Plonsey and R. C. Barr, "Mathematical modeling of electrical activity of the heart.," *Journal of electrocardiology*, vol. 20, no. 3, pp. 219–26, 1987.

[11] A. L. Hodgkin and A. F. Huxley, "A quantitative description of membrane current and its application to conduction and excitation in nerve," *The Journal of Physiology*, vol. 117, pp. 500–544, 8 1952.

[12] C. H. Luo and Y. Rudy, "A model of the ventricular cardiac action potential. Depolarization, repolarization, and their interaction," *Circulation Research*, 1991.

[13] K. H. W. J. ten Tusscher, D. Noble, P. J. Noble, and A. V. Panfilov, "A model for human ventricular tissue," *American Journal of Physiology-Heart and Circulatory Physiology*, vol. 286, pp. H1573–H1589, 4 2004.

[14] R. Fitzhugh, "Impulses and Physiological States in Theoretical Models of Nerve Membrane.," *Biophysical journal*, vol. 1, pp. 445–66, 7 1961.

[15] C. C. Mitchell and D. G. Schaeffer, "A two-current model for the dynamics of cardiac membrane," *Bulletin of Mathematical Biology*, vol. 65, no. 5, pp. 767–793, 2003.

[16] J. Nagumo, S. Arimoto, and S. Yoshizawa, "An Active Pulse Transmission Line Simulating Nerve Axon," *Proceedings of the IRE*, vol. 50, pp. 2061–2070, 10 1962.

[17] P. Hunter and B. Smaill, "The analysis of cardiac function: A continuum approach," *Progress in Biophysics and Molecular Biology*, vol. 52, no. 2, pp. 101–164, 1988.

[18] M. Wallman, N. P. Smith, and B. Rodriguez, "A comparative study of graph-based, eikonal, and monodomain simulations for the estimation of cardiac activation times," *IEEE Transactions on Biomedical Engineering*, vol. 59, no. 6, pp. 1739–1748, 2012.

[19] M. Okajima, T. Fujino, T. Kobayashi, and K. Yamada, "Computer simulation of the propagation process in excitation of the ventricles," *Circulation Research*, vol. 23, no. 2, pp. 203–211, 1968.

[20] P. M. van Dam, T. F. Oostendorp, and A. van Oosterom, "Application of the fastest route algorithm in the interactive simulation of the effect of local ischemia on the ECG," *Medical and Biological Engineering and Computing*, vol. 47, no. 1, pp. 11–20, 2009.

[21] A. van Oosterom and T. F. Oostendorp, "ECGSIM: an interactive tool for studying the genesis of QRST waveforms.," *Heart (British Cardiac Society)*, vol. 90, pp. 165–8, 2 2004.

[22] U. C. Nguyên, N. J. Verzaal, F. A. van Nieuwenhoven, K. Vernooy, and F. W. Prinzen, "Pathobiology of cardiac dyssynchrony and resynchronization therapy," *EP Europace*, vol. 6, pp. 1660–1665, 5 2018.

[23] Streeter and W. T. Hanna, "Engineering Mechanics for Successive States in Canine Left Ventricular Myocardium," no. 17, pp. 639–655, 1973.

[24] J. Aguado-Sierra, A. Krishnamurthy, C. Villongco, J. Chuang, E. Howard, M. J. Gonzales, J. Omens, D. E. Krummen, S. Narayan, R. C. P. Kerckhoffs, and A. D. McCulloch, "Patient-specific modeling of dyssynchronous heart failure: A case study," *Progress in Biophysics and Molecular Biology*, vol. 107, no. 1, pp. 147–155, 2011.

[25] E. R. Hyde, J. M. Behar, S. Claridge, T. Jackson, A. W. C. Lee, E. W. Remme, M. Sohal, G. Plank, R. Razavi, C. A. Rinaldi, and S. A. Niederer, "Beneficial Effect on Cardiac Resynchronization from Left Ventricular

Endocardial Pacing Is Mediated by Early Access to High Conduction Velocity Tissue: Electrophysiological Simulation Study," *Circulation: Arrhythmia and Electrophysiology*, vol. 8, no. 5, pp. 1164–1172, 2015.

[26] E. Kayvanpour, T. Mansi, F. Sedaghat-Hamedani, A. Amr, D. Neumann, B. Georgescu, P. Seegerer, A. Kamen, J. Haas, K. S. Frese, M. Irawati, E. Wirsz, V. King, S. Buss, D. Mereles, E. Zitron, A. Keller, H. A. Katus, D. Comaniciu, and B. Meder, "Towards personalized cardiology: Multi-scale modeling of the failing heart," *PLoS ONE*, vol. 10, no. 7, pp. 1–18, 2015.

[27] A. Lee, U. Nguyen, O. Razeghi, J. Gould, B. Sidhu, B. Sieniewicz, J. Behar, M. Mafi-Rad, G. Plank, F. Prinzen, C. Rinaldi, K. Vernooy, and S. Niederer, "A rule-based method for predicting the electrical activation of the heart with cardiac resynchronization therapy from non-invasive clinical data," *Medical Image Analysis*, vol. 57, pp. 197–213, 2019.

[28] J.-i. Okada, T. Washio, M. Nakagawa, M. Watanabe, Y. Kadooka, T. Kariya, H. Yamashita, Y. Yamada, S.-i. Momomura, R. Nagai, T. Hisada, and S. Sugiura, "Multi-scale, tailor-made heart simulation can predict the effect of cardiac resynchronization therapy," *Journal of Molecular and Cellular Cardiology*, vol. 108, pp. 17–23, 7 2017.

[29] S. Weinberg, S. Iravanian, and L. Tung, "Representation of collective electrical behavior of cardiac cell sheets," *Biophysical Journal*, vol. 95, no. 3, pp. 1138–1150, 2008.

[30] D. E. Roberts, L. T. Hersh, and A. M. Scher, "Influence of cardiac fiber orientation on wavefront voltage, conduction velocity, and tissue resistivity in the dog," *Circulation Research*, vol. 44, no. 5, pp. 701–712, 1979.

[31] W. T. Miller and D. B. Geselowitz, "Simulation studies of the electrocardiogram. II. Ischemia and infarction.," *Circulation research*, vol. 43, pp. 315–323, 8 1978.

[32] S. Giffard-Roisin, T. Jackson, L. Fovargue, J. Lee, H. Delingette, R. Razavi, N. Ayache, and M. Sermesant, "Noninvasive Personalization of a Cardiac Electrophysiology Model From Body Surface Potential Mapping," *IEEE Transactions on Biomedical Engineering*, vol. 64, pp. 2206–2218, 9 2017.

[33] K. Aras, W. Good, J. Tate, B. Burton, D. Brooks, J. Coll-font, O. Doessel, W. Schulze, D. Potyagaylo, L. Wang, P. V. Dam, and R. Macleod, "ScienceDirect Experimental Data and Geometric Analysis Repository — EDGAR," *Journal of Electrocardiology*, vol. 48, no. 6, pp. 975–981, 2015.

[34] R. C. P. Kerckhoffs, P. H. M. Bovendeerd, F. W. Prinzen, K. Smits, and T. Arts, "Intra- and interventricular asynchrony of electromechanics in the ventricularly paced heart," *Journal of Engineering Mathematics*, vol. 47, no. 3-4, pp. 201–216, 2003.

[35] D. Wei, O. Okazaki, K. Harumi, E. Harasawa, and H. Hosaka, "Comparative simulation of excitation and body surface electrocardiogram with isotropic and anisotropic computer heart models," *IEEE Transactions on Biomedical Engineering*, vol. 42, no. 4, pp. 343–357, 1995.

[36] K. Vernooy, C. J. M. van Deursen, M. Strik, and F. W. Prinzen, "Strategies to improve cardiac resynchronization therapy.," *Nature reviews. Cardiology*, vol. 11, no. 8, pp. 481–93, 2014.

[37] M. Mafi Rad, G. W. Wijntjens, E. B. Engels, Y. Blaauw, J. G. Luermans, L. Pison, H. J. Crijns, F. W. Prinzen, and K. Vernooy, "Vectorcardiographic QRS area identifies delayed left ventricular lateral wall activation determined by electroanatomic mapping in candidates for cardiac resynchronization therapy," *Heart Rhythm*, vol. 13, no. 1, pp. 217–225, 2016.

[38] M. W. Kimmel, N. D. Skadsberg, C. L. Byrd, D. J. Wright, T. G. Laske, and P. A. Iaizzo, "Single-site ventricular and biventricular pacing: investigation of latest depolarization strategy," *Europace*, vol. 9, pp. 1163–1170, 10 2007.

[39] D. Romero, R. Sebastian, B. H. Bijnens, V. Zimmerman, P. M. Boyle, E. J. Vigmond, and A. F. Frangi, "Effects of the purkinje system and cardiac geometry on biventricular pacing: A model study," *Annals of Biomedical Engineering*, vol. 38, no. 4, pp. 1388–1398, 2010.

[40] H. J. Arevalo, F. Vadakkumpadan, E. Guallar, A. Jebb, P. Malamas, K. C. Wu, and N. A. Trayanova, "Arrhythmia risk stratification of patients after myocardial infarction using personalized heart models," *Nature Communications*, vol. 7, p. 11437, 9 2016.

[41] F. Pashakhanloo, D. A. Herzka, H. Halperin, E. R. McVeigh, and N. A. Trayanova, "Role of 3-Dimensional Architecture of Scar and Surviving Tissue in Ventricular Tachycardia," *Circulation: Arrhythmia and Electrophysiology*, vol. 11, p. e006131, 6 2018.

[42] A. J. Prassl, F. Vadakkumpadan, N. Trayanova, H. Arevalo, G. Plank, J. Chen, P. Kohl, and F. Kickinger, "Image-based models of cardiac structure in health and disease," *Wiley Interdisciplinary Reviews: Systems Biology and Medicine*, vol. 2, no. 4, pp. 489–506, 2010.

5

Developing a finite-element mechanical model for predicting mechanics of cardiac resynchronization therapy

5.1 Introduction

5.1.1 Virtual CRT, continued

In the past decade, many groups have developed electrical and mechanical models to predict acute effects of CRT.[1–8] These models have all featured high-resolution biventricular models that simulated electrical propagation with reaction-diffusion type formulations. The coupled mechanical models also used the same high-resolution geometries to simulate mechanics. These models were capable of simulating changes in electrical and mechanical function from different pacing locations, which can help optimize patient-specific CRT. However, the high computational cost makes them intractable for clinical translation without high performance computing. To create a clinically translatable model, we developed a simple electrical model capable of simulating LBBB

and pacing in Chapter 4. The results of that model are intended to serve as an input for mechanical model that will simulate the mechanics of a cardiac cycle. In this chapter, we tested the utility of a finite-element mechanical model for the mechanical component of the *Virtual CRT* pipeline.

5.1.2 Mechanical modeling

Mechanical models of the heart simulate the stress and strain experienced by the tissue throughout the cardiac cycle. Different implementations of mechanical models vary in their geometric assumptions about the LV. The simplest geometric representations include a thin-walled sphere or a thick-walled cylinder, which can be solved analytically.[9–13] More physiologic, patient-specific geometries can be generated using finite-element methods; however, they require dedicated numerical solvers to implement. While the simple geometries can provide a global estimate of stress and strain in the LV, finite-element models provide higher spatial resolution that can account for regional variations in geometry or material properties. This capability may be particularly important in the case of LBBB where different regions of the heart contract at different times and some regions may include post-infarction scar.

One key advancement in the field of biomechanics is the development of algorithms to predict LV growth based on changes in regional mechanics.[13–18] Extending these techniques to patient-specific models may allow for integration of imaging and clinical data to predict long-term response from CRT. The success of these remodeling predictions heavily relies on the ability to accurately simulate LV mechanics. Non-invasive imaging techniques now enable tracking of tissue mechanics (strains) throughout the cardiac cycle.[19,20] These techniques track tissue at various short- and long-axis slice planes, which can be registered together using methods developed in Chapter 3 to interpolate mechanical metrics across the whole LV.[21] In this chapter, we used LV volumes from cine MRI and strain tracking from displacement encoding with stimulated echoes (DENSE) MRI to tune subject-specific finite-element mechanical models to accurately simulate pre-CRT mechanics. While we were able to match reported strains in some situations, the simulated local active contraction curves required to do so were physiologically implausible, suggesting that some critical aspects of the mechanics of dyssynchrony are still not adequately represented in our models.

5.2 Methods

5.2.1 Mechanical modeling pipeline

The goal of the mechanical modeling pipeline is to simulate the mechanics of the LV during LBBB as well as the changes associated with CRT. The idealized modeling pipeline using a finite-element mechanical model is laid out in Figure 5.1 (A and B). The first step is coupling of the electrical and mechanical models. Simulated electrical activation times are used to generate active contraction load curves which define when different regions of the LV contract. The electrical activation times can come from a baseline (LBBB, pre-CRT) model or a paced (CRT) model. A full cardiac cycle is simulated using the active contraction load curves and patient-specific LV pressures. The resulting regional mechanical response (strains) are used to predict growth and remodeling which feed back into the mechanical model for subsequent cardiac cycle simulations.[16,22–24]

The critical component of the mechanical modeling pipeline is the electro-mechanical coupling. Ideally, we can define a function that takes in the electrical activation times and predicts regional active contraction load curves to prospectively simulate mechanical response (LV volume and strains); however, we do not know the formulation of this coupling. In this chapter, we used subject-specific baseline models (pre-CRT) to simulate LV mechanics. We optimized active contraction load curves based on either volume or strain errors to match measured mechanics data from cine or DENSE MRI (Fig. 5.1C and 5.1D). With these optimizations, we evaluated whether the mechanical modeling pipeline could accurately simulate mechanics.

5.2.2 Mechanical data

We simulated 6 canine subject-specific models with LBBB (including 2 with myocardial infarction scar). For each canine, cine and DENSE MRI were recorded one week after inducing LBBB to provide volume and strain data, respectively. LV cavity volumes were calculated using segmented short- and long-axis slices of the LV throughout the cardiac cycle. LV pressure was also recorded from a pressure catheter immediately after the MRI recording. The volume and pressure data were aligned to generate a pressure-volume (PV) loop for each subject (Fig. 5.2A). The end diastolic point of the PV loop (bottom right corner) indicates the end of passive filling and start of active contraction in the cardiac cycle.

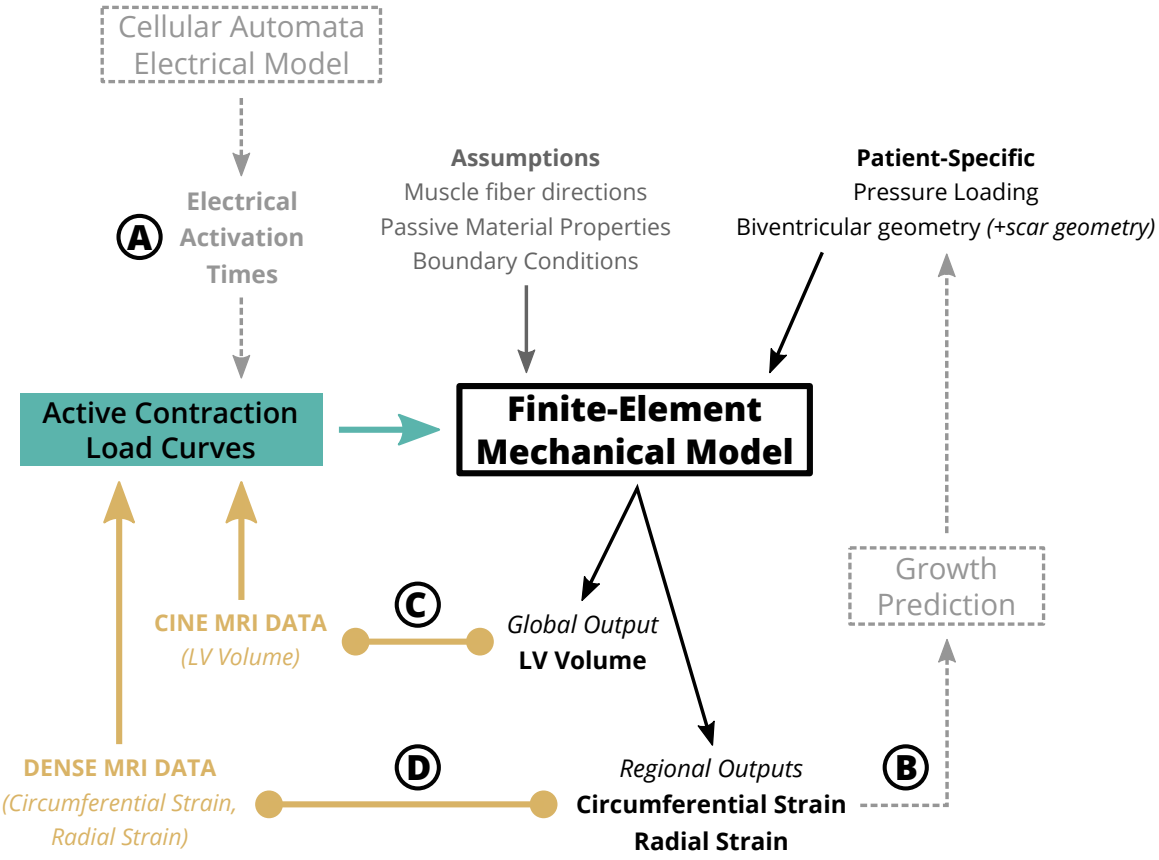

Figure 5.1: Mechanical modeling pipeline. (A) Input from an electrical model defines the regional active contraction load curves in a finite-element mechanical model. (B) The resulting regional strains are input into a growth model to predict changes in the LV geometry. (C, D) To tune the electro-mechanical coupling defining the active contraction load curves, we used recorded mechanical data from cine and DENSE MRI to compare to the simulated mechanical outputs.

We measured circumferential and radial strains from DENSE MRI in 6 short-axis slices of the LV.[25] For each slice, the strain data was binned into 6 sectors for a total of 36 distinct regions (Fig. 5.2C). We aligned the DENSE MRI frames to the PV loop to indicate when the strain data was measured throughout the cardiac cycle (Fig. 5.2A, circles). For all subjects, the strain data began after the start of active contraction (end diastole). For comparison of model simulations to this strain data, we adjusted the simulated strain reference point to match DENSE MRI. To evaluate the impact of the delay in measuring strains, we also modeled canine case C3 at a later time point (9 weeks after inducing LBBB) when DENSE MRI strains were available for the full cardiac cycle.

5.2.3 Building a finite-element model

Mechanical models were created to simulate the mechanics of the LV during LBBB for the canine dataset using FEBio v2.9.[26] Subject-specific models of the LV were created using the methods described in Chapter 3. A ring of rigid-body elements was added next to the most basal, endocardial elements at the mitral valve position. The mitral valve ring was fixed in all directions. A ring of rigid-body elements was added at the apex and constrained to slide along and rotate around the base-apex axis of the LV similar to Estrada et al.[27] A pressure load was applied to the inner surface of the LV to simulate loading from the blood. To represent loading from the RV, a pressure load scaled to 20% of the LV pressure was applied to a selected region of the LV outer surface where the elements were located inside the RV in the biventricular geometry (Fig. 5.2B).

The material properties were assigned using a transversely isotropic Mooney-Rivlin (TIMR) material with active contraction. All myocardial elements were given the same passive material properties fitted by Estrada et al. with the exception of a slightly softer isotropic stiffness ($C_1 = 0.34 kPa$).[27] For models with scar, an isotropic, stiffer combination of parameters with no active contraction was used for the TIMR material in scar elements. The isotropic coefficients were increased to $C_1 = 1.65\ kPa$ and $C_2 = 4.0\ kPa$ and the fiber terms were set to zero based on previous work by Moyer to simulate cardiac fibrosis.[28]

Active contraction was implemented by providing a load curve which adds active stress along the muscle fiber direction as well as scales C_1 and K, the bulk modulus, by 10 times. The active contraction implemented by Estrada et al. also accounts for force-length and force-velocity relationships of cardiac muscle.[27] 36 active contraction load curves were defined for the 36 regions

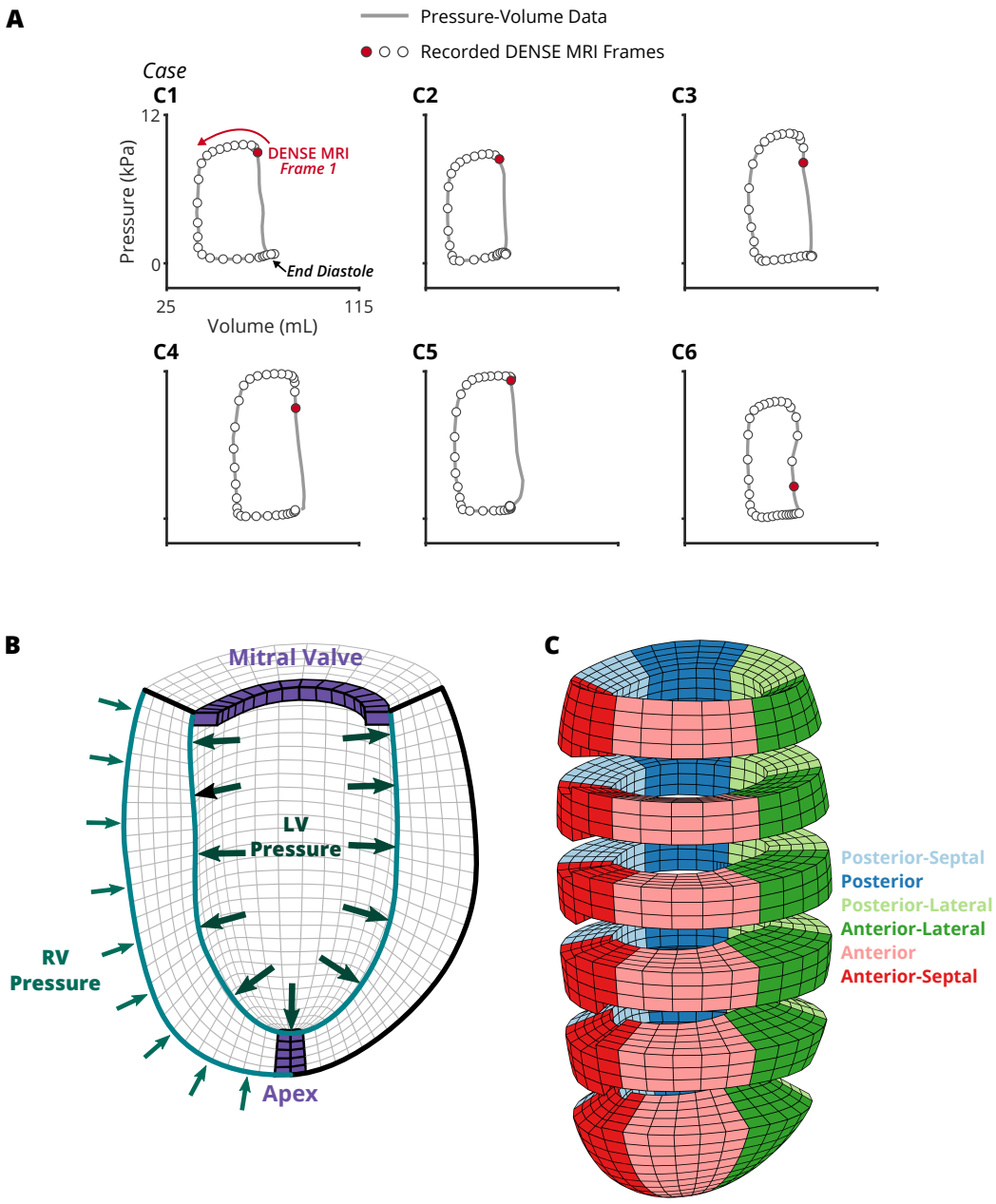

Figure 5.2: (A) Pressure volume loops for 6 canines. The recorded DENSE MRI for all subjects started after end diastole missing the early phase of active contraction. (B) Cross-section of LV finite-element mesh highlighting boundary conditions and loading surfaces. The mitral valve was fixed in all directions, and the apex was allowed to slide along and rotate about the base-apex axis. An LV pressure was applied to the endocardial surface, and 20% of the LV pressure was applied as the RV pressure on the epicardial surface shared with the RV. (C) The LV was divided into 36 regions based on the 6 short-axis DENSE MRI slice locations recorded for each subject. Each short-axis ring was divided into 6 circumferential sectors.

allowing for dyssynchronous contraction associated with LBBB (Fig. 5.2C).

Unloading geometry

Throughout the cardiac cycle, the LV is always pressurized by the blood volume present in the chamber. The LV models were generated from segmented MRI at end diastole. Simulating a finite-element mechanical model relies on starting from a completely unloaded (un-pressurized) geometry. To approximate the unloaded geometry, we iteratively scaled down the LV geometry while conserving wall mass and simulated passive inflation to the recorded end-diastolic pressure. We constrained the unloaded LV cavity volume to be smaller than the minimum volume of the PV loop. We assessed the fit of each scaled down geometry by comparing the simulated PV with the passive filling portion of the recorded PV loop. The unloaded geometry with the best fit was used as the starting geometry for the cardiac cycle simulations. The optimized passive inflation simulations for each subject are shown in Figure 5.3.

5.2.4 Optimization schemes

Volume cost function

To test whether the finite-element mechanical model could replicate *in vivo* LBBB mechanics, we first tested an optimization scheme to tune active contraction load curves based on measured LV cavity volume. For each region, we assumed active contraction started at its average electrical activation time (from the electrical model) but followed a common tension generation profile thereafter; therefore, we time-shifted the common load curve to start at each region's electrical activation time (example in Fig. 5.4C).

The error between the simulated and measured volume was used to tune the common load curve. Because the regions contracted at different times, each point in the load curve contributed to the simulated volume at different times throughout the cardiac cycle. Therefore, the error applied to alter the load curve was calculated by summing regional errors. Each regional error was calculated by time-shifting the volume error by the regional time delay and scaling the volume error by the mass of the region. The common contraction load curve was iteratively altered until the volume error converged. An example of the volume cost optimization is shown in Figure 5.4.

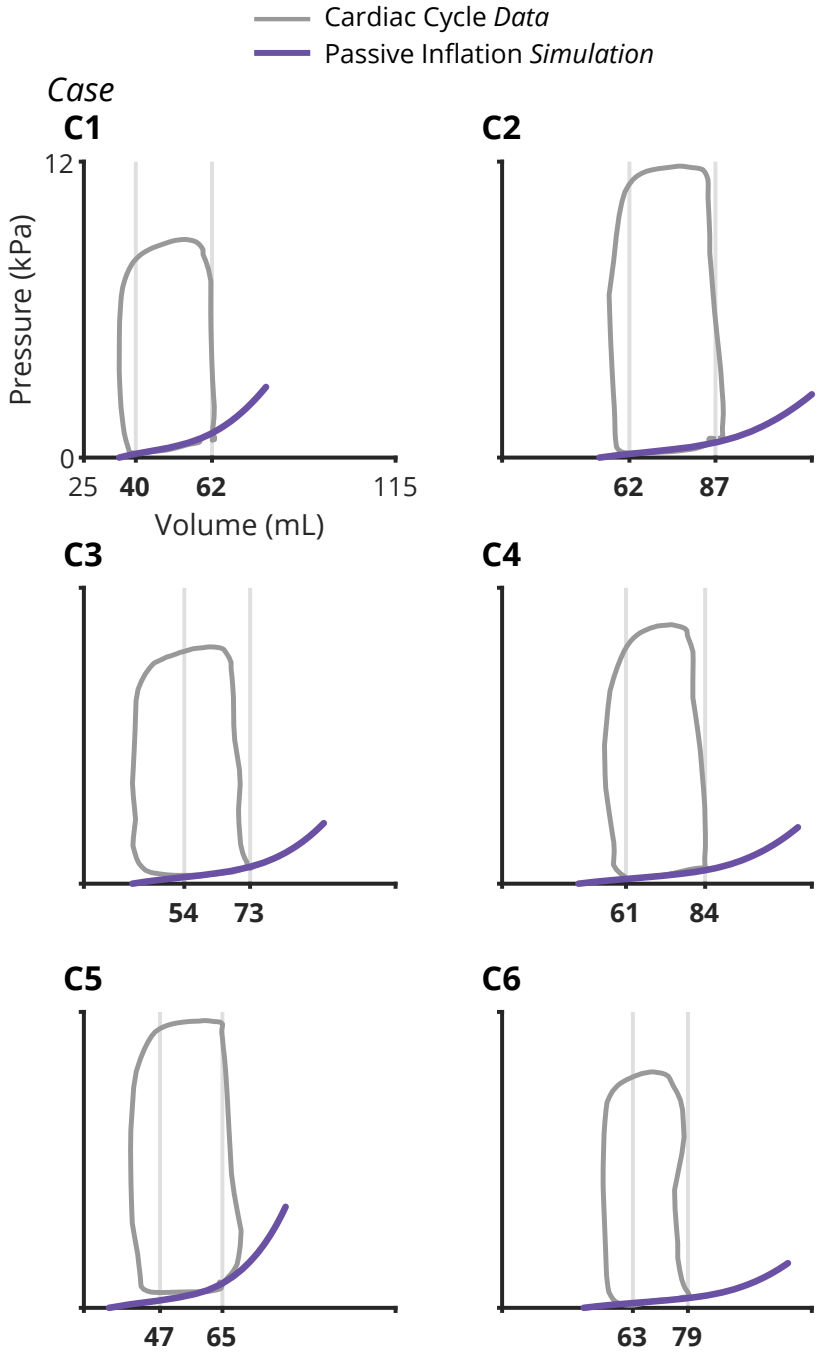

Figure 5.3: Passive inflation simulations for each canine subject-specific model from their optimized unloaded geometries. The unloaded geometry was optimized so that the passive inflation simulation best matched the passive filling of the PV loop data. The two, bolded volume values indicate the bounds of the passive filling phase which were used to evaluate the simulations.

Strain cost function

As an alternative approach, we uncoupled the electrical and mechanical models by removing the common active contraction load curve constraint and optimized each subject using regional strain data. We allowed for all 36 regions to contract with independent load curves regardless of the electrical activation time. Each region started with the same initial contraction load curve based on the elastance of the LV calculated from the recorded PV loop. The model strains were calculated as the average circumferential and radial strains for the elements in each region (with matched reference time to the DENSE MRI data).

Each regional strain error was calculated by summing the difference between the simulated and recorded circumferential and radial strains. The regional strain error was used to directly tune the regional active contraction load curve. The load curves were iteratively altered until the sum of all regional strain errors converged. An example of the strain cost optimization is shown in Figure 5.4.

Comparing optimization cost functions

The volume and strain optimization approaches were compared by looking at their fits to recorded data and their optimized active contraction load curves. Volume error was calculated using sum of squared errors. The strains were compared for a single short-axis slice located halfway base-to-apex in the LV. Sum of squared errors was calculated for the circumferential and radial strains. The volume and cost optimizations were repeated for a final subject case which included DENSE MRI for the entire cardiac cycle.

5.3 Results

5.3.1 Simulating LBBB mechanics

We used two optimization schemes (volume and strain cost functions) to simulate 6 canine models to match LBBB mechanics. The first two subject-specific models (cases C1 and C2) included myocardial infarction scar. We evaluated the final results of the optimizations for their fit to measured volumes and strains.

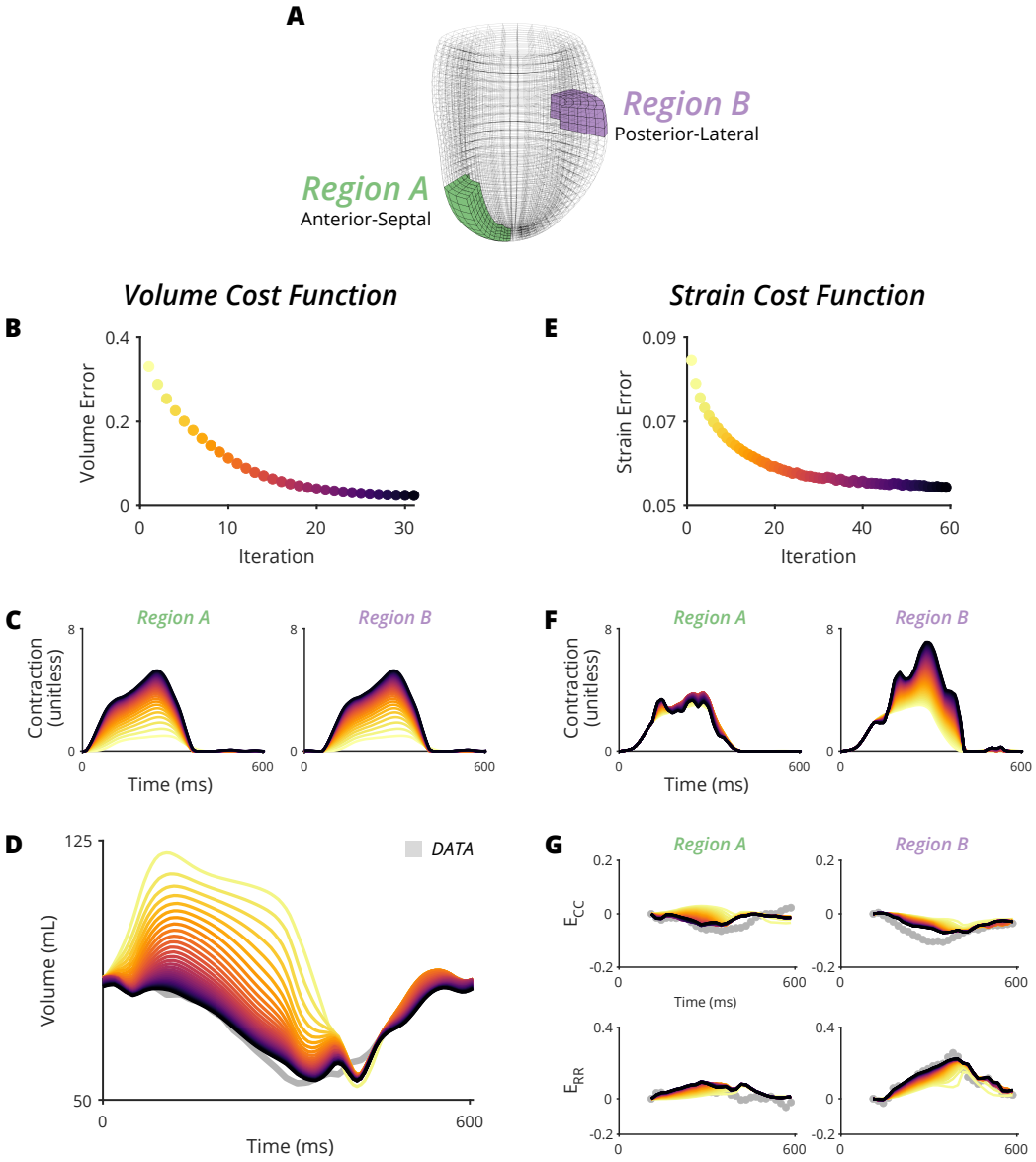

Figure 5.4: Examples of tuning active contraction load curves to match measured mechanics in case C4. (A) Active contraction load curves are shown for 2 of the 36 regions in the LV. (B) Convergence of the volume errors throughout optimization iterations (yellow to purple color gradient). (C) The contraction load curves in the two regions were constrained to have the same shape. However, the region B load curves were time-shifted based on its electrical activation time. (D) The simulated volumes converged towards the data (gray) throughout the optimization iterations. (E) Convergence of the strain errors calculated as the sum of the circumferential and radial strain sum of squared errors in all 36 regions. (F) Both regions started from the same initial load curve (yellow) and converged towards separate shapes. (G) The circumferential and radial strains in the two regions moved towards their data values throughout the optimization iterations. Note the simulated strain was calculated starting from a later time point to match the available DENSE MRI data.

LV volume

The volume cost optimization achieved a better fit to volume data for all cases compared to the strain cost optimization (Fig. 5.5). For the strain cost, the deviation in volume fit is most evident during the early systole phase (from time 0) in Figure 5.5B. The start of the recorded DENSE MRI occurred about 122±33 ms after end diastole, which meant no changes to the active contraction load curves could be made during the beginning of contraction in the strain optimization. This led to an overall decrease stroke volume (width of the PV loop) compared to the data (Fig. 5.5A). The sum of squared volume errors were much larger for the strain cost optimization compared to the volume cost (Fig. 5.5C).

LV strains

To compare circumferential and radial strains to DENSE MRI, we reported strains from a single, mid-LV short-axis slice in all cases. The reference time for DENSE MRI was slightly after end diastole for all cases; therefore, the model strains were calculated from a matched reference state for each case (time greater than 0 ms, Fig. 5.6A and 5.6B). Overall, the simulated circumferential strains for both cost functions had lower ranges than the data (Fig 6A). The circumferential strain patterns observed in the data were not distinguishable in the optimized simulations.

For both cost functions, the radial strains better matched the data ranges (Fig. 5.6B). With the exception of case C2, the simulated radial strains better matched data with the strain cost function. For cases C3, C4, C5, and C6, the Posterior-Lateral (light green) and Anterior-Lateral (dark green) regions thicken (positive radial strain) similar to the data. And the Anterior-Septal (dark red) and Posterior-Septal (light blue) regions thin (negative strain) similar to the data. Overall, the simulated strains slightly improved with the strain cost function compared to the volume cost (Fig. 5.6C). However, the simulated patterns of circumferential and radial strains require further improvement to match measured patterns.

5.3.2 Active contraction load curves

The volume and strain cost optimizations were marked by dramatic differences in the final active contraction load curves for the 36 regions in each model (Fig. 5.7). For the volume cost, one active

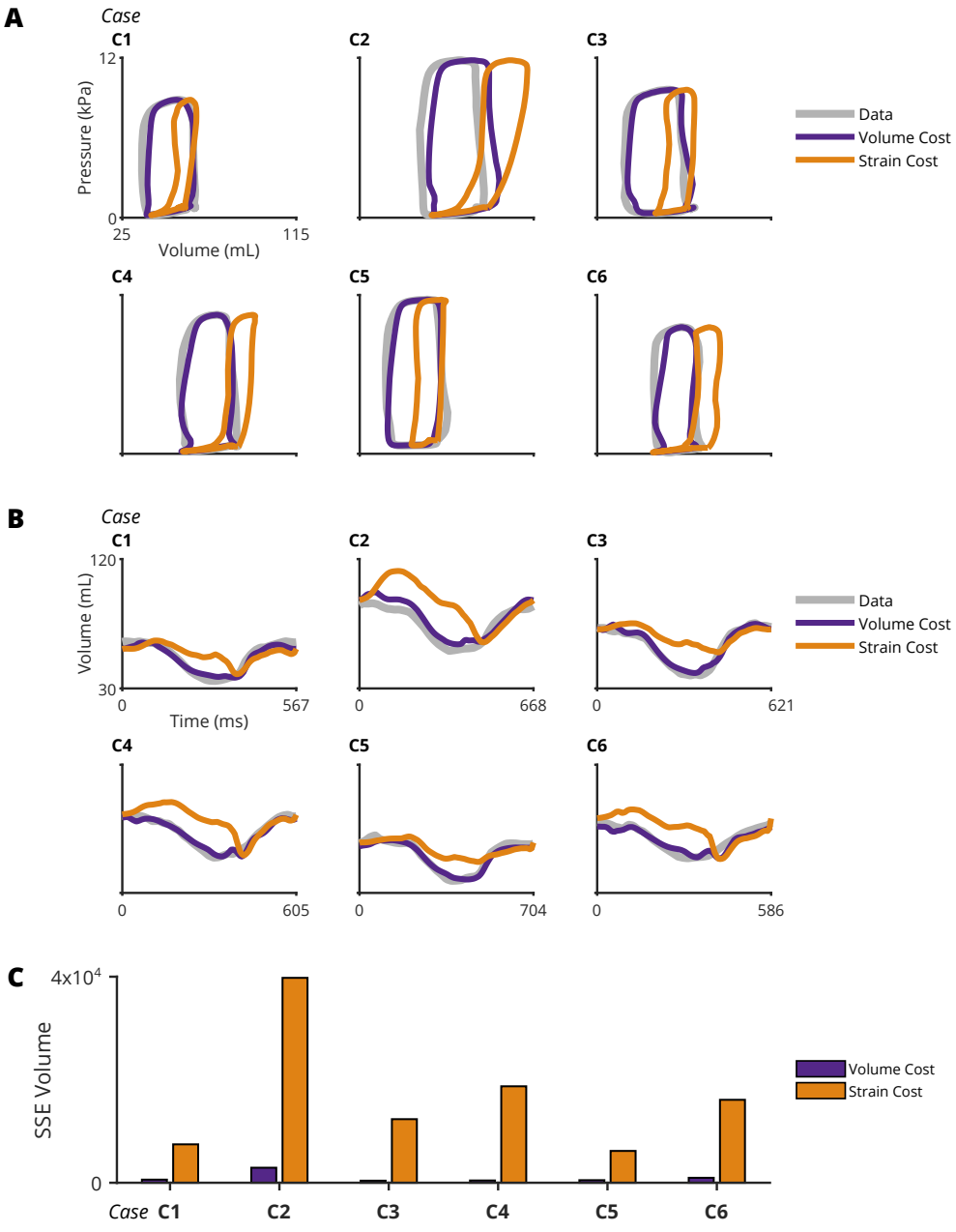

Figure 5.5: Comparing volume error from different optimization cost functions. Simulated pressure-volume loops (A) and volume-time curves (B) from volume cost and strain cost optimizations compared to recorded data. Volume-time curves start from end diastole at time 0 ms. (C) Volume sum of squared errors (SSE) showed a higher error for the strain cost optimizations.

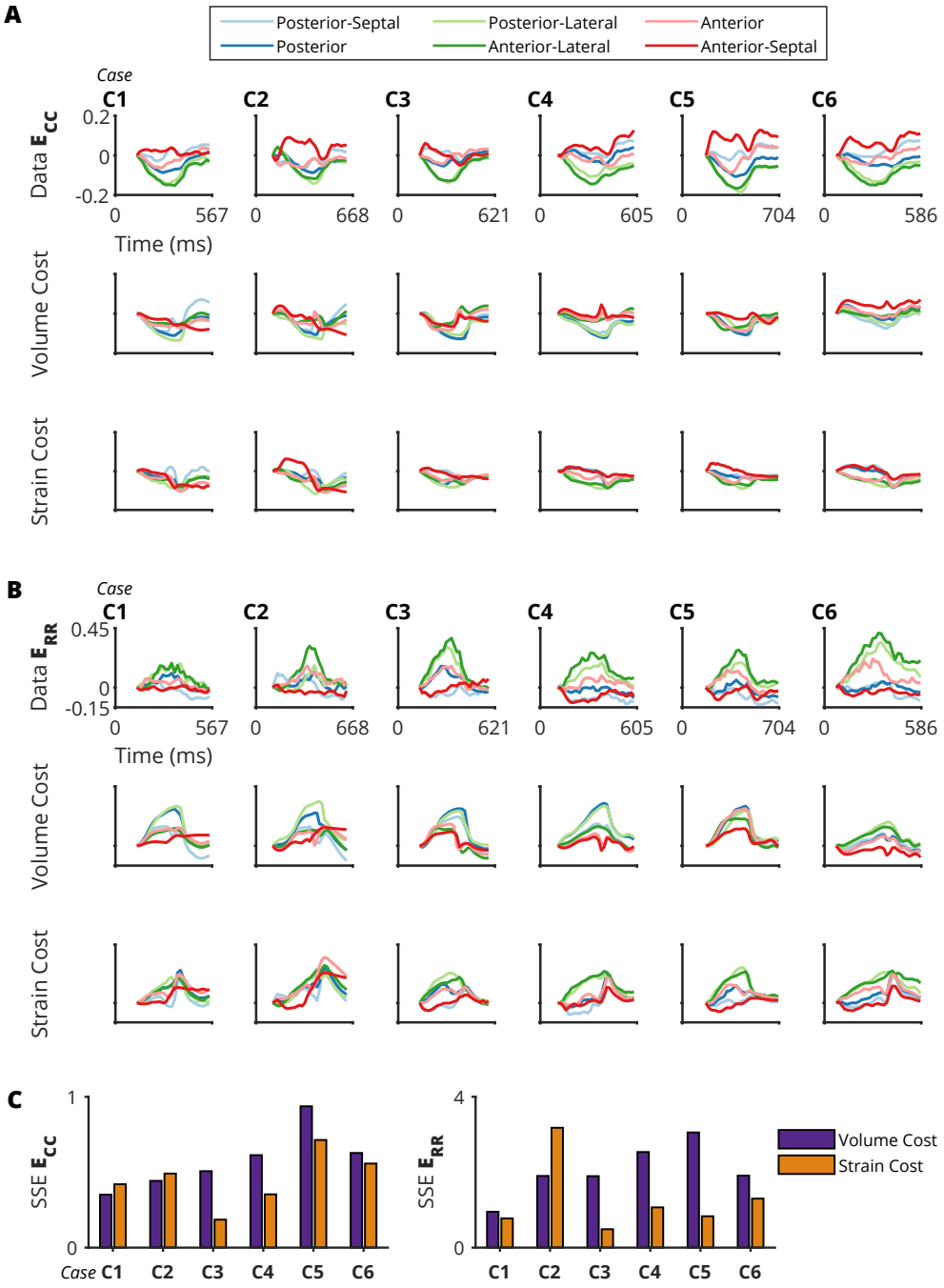

Figure 5.6: Comparing strain error from different optimization cost functions in a single mid-LV slice location. Circumferential (A) and radial (B) strains for a single mid-LV slice in each case compared to data from DENSE MRI. The model strains were calculated with the same reference time as DENSE MRI, which did not occur at end diastole (time 0 ms). (C) Sum of squared errors for circumferential and radial strains to compare cost functions.

contraction load curve was altered and applied to all regions according to the electrical activation time. For the strain cost, each region featured its own active contraction load curve that changed based on the strain error. The volume cost contraction load curves all converged towards a similar shape featuring a double-hump. In contrast, the strain cost contraction load curves did not share a distinguishable common shape. The strain cost optimization results were also confounded by the lack of data during early contraction causing all regional load curves to remain unchanged during that portion of the cardiac cycle.

5.3.3 Full cardiac cycle mechanics

Because the DENSE MRI reference time for the 6 cases did not align with end diastole, we tested one additional data set with DENSE MRI reference starting at end diastole. A new, biventricular geometry was generated for the case, and the electrical activation times previously simulated for case C3 were mapped onto the model. The same unloading, volume cost, and strain cost optimizations were completed for the new data set.

The simulated volumes from both cost functions matched the recorded volume well (Fig. 5.8A and 5.8B). The simulated strains did not match the data for the volume cost optimization; however, the simulated patterns of strain greatly improved with the strain cost function (Fig. 5.8C and 5.8D). While the patterns are more distinguishable, the ranges for both circumferential and radial strains are still smaller compared to the data.

The optimized active contraction load curves for the volume cost featured a similar double-hump shape to the previously simulated cases (Fig. 5.7 and 5.8E). The strain cost contraction load curves did not share a common, distinguishable shape. Overall, the strain cost optimization was able to reproduce more features of regional mechanics than the volume-based optimization approach when full-cycle DENSE was available, but still displayed obvious limitations.

5.4 Discussion

The goal of the mechanical modeling pipeline is to generate accurate predictions of LV mechanics which will be used to predict long-term growth and remodeling. We tested whether our finite-element mechanical modeling pipeline could simulate LV mechanics including volumes

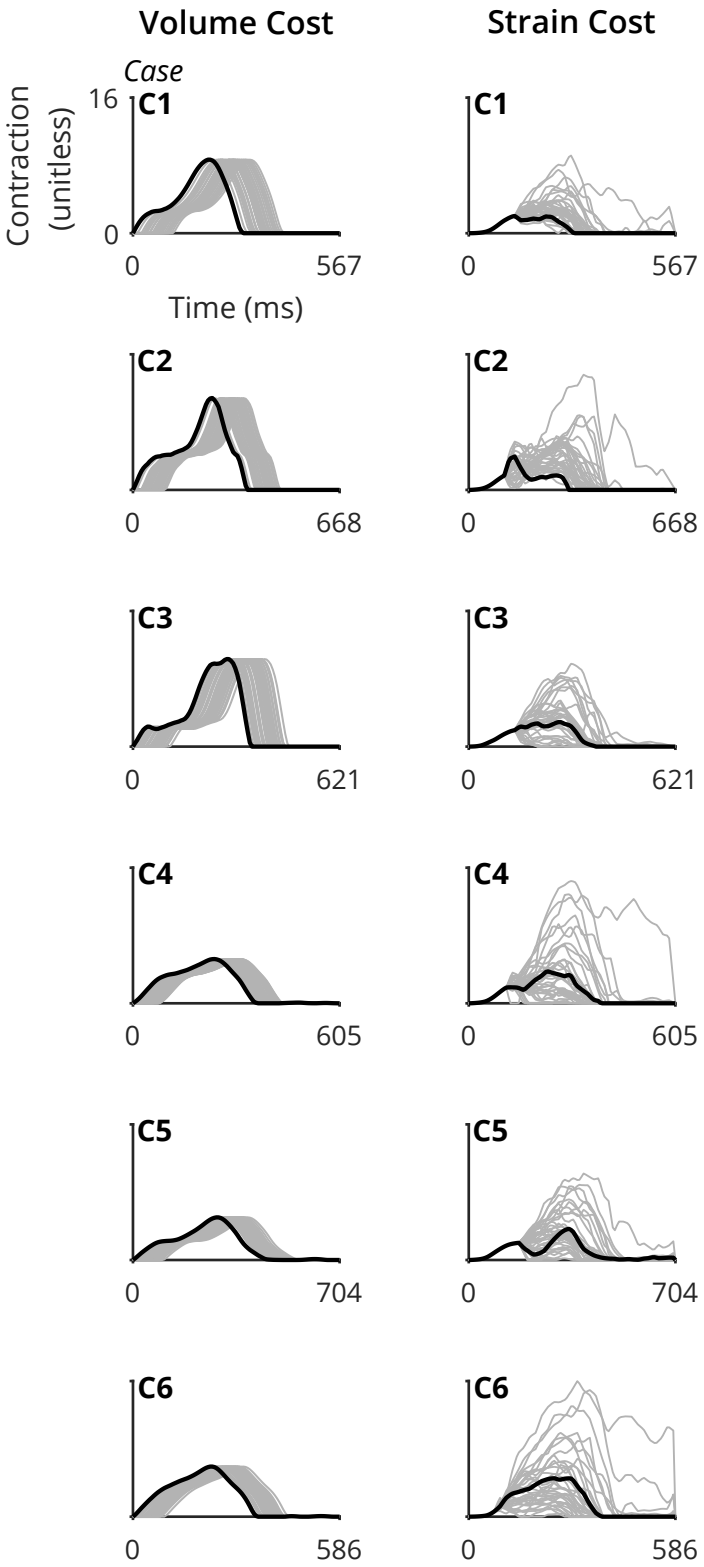

Figure 5.7: Optimized contraction load curves for each case (rows) and cost functions (columns). Each plot shows the 36 load curves for each model. One matched region's load curve is highlighted (black) in each case. The volume cost contraction load curves are a single load curve time-shifted according to electrical activation time. The strain cost contraction load curves are individually optimized to match strain data.

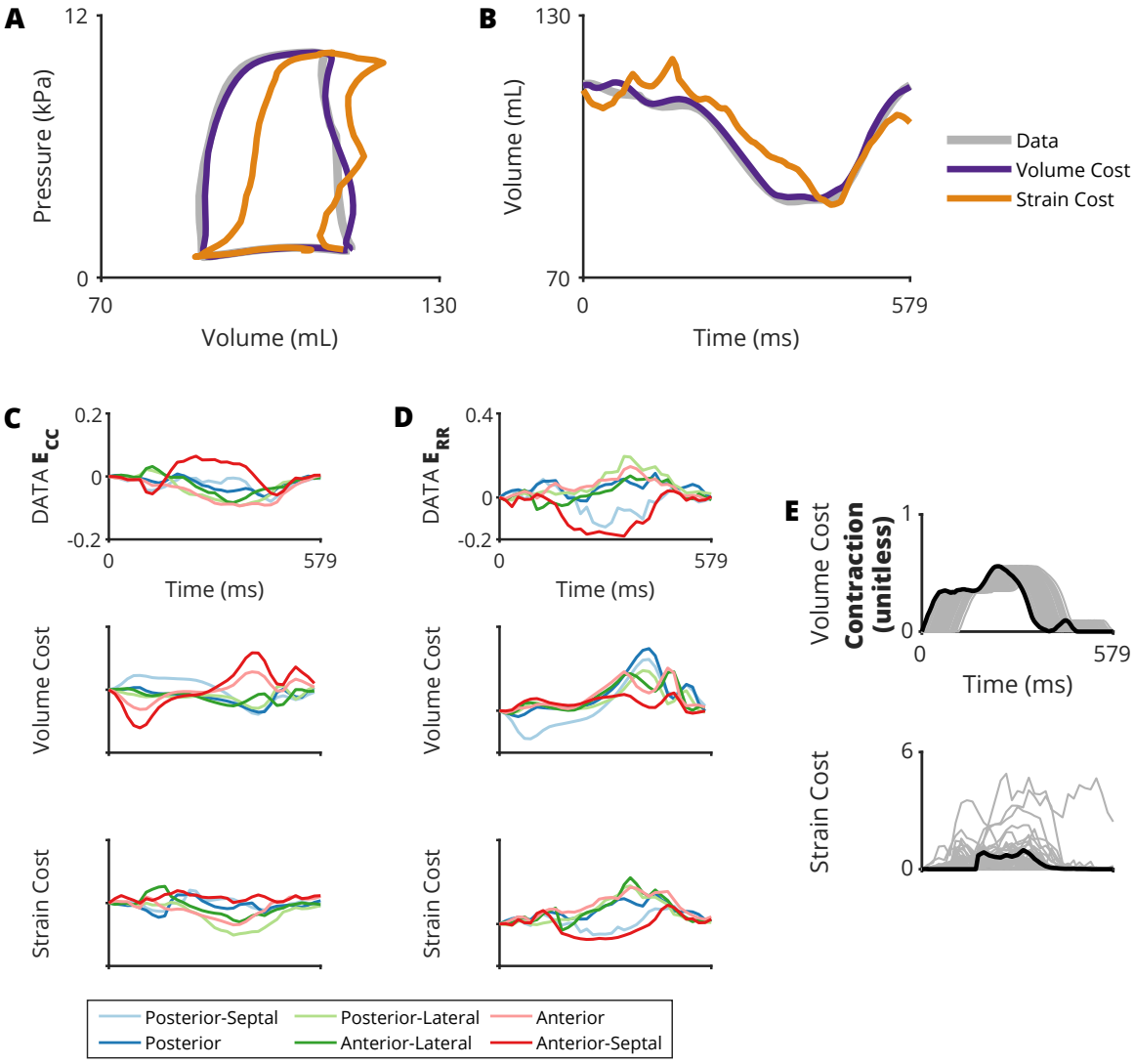

Figure 5.8: For a case with full cycle DENSE MRI, the optimized pressure-volume loop (A) and volume-time curve (B) for both volume and strain cost functions match data well. However, the strain cost model featured simulated circumferential (C) and radial (D) strains that better matched DENSE MRI. (E) The contraction load curves are shown with one common region highlighted (black) for the volume and strain cost.

and strains. We used 6 canine subject-specific models based on the electrical modeling from the previous chapter to simulate pre-CRT mechanics. We used two optimization schemes to tune regional active contraction load curves to match mechanics.

5.4.1 Assuming a simple electro-mechanical coupling

Different electro-mechanical mapping techniques have been used to reveal a homogeneous electro-mechanical delay of about 20 to 40 ms in canines.[29–31] In our modeling pipeline, we assumed a homogeneous, constant electro-mechanical delay across the LV. The simplest formulation for electro-mechanical coupling assumes that each region of the LV contracts along the same active contraction load curve time-shifted according to its electrical activation time. This assumption requires tuning of only one common load curve among all 36 regions. We tuned all of the subject-specific models to match their recorded LV volumes throughout the cardiac cycle (Fig. 5.5B). The simulated volumes matched the data very well in all subjects, and the tuned common contraction load curves all shared a distinguishable double-hump shape (Fig. 5.7). While the shape is a promising finding for defining an electro-mechanical coupling function, the simulations did not match recorded circumferential and radial strains, which means the models failed to simulate LBBB mechanics (Fig. 5.6).

One feature of the finite-element model that affects the mechanical response is the boundary conditions. The models did not have full valve boundary conditions to enforce isovolumetric contraction and relaxation during the cardiac cycle. This confounded the interpretation of the resulting contraction load curves by increasing the sensitivity of the simulated mechanics to the load curve during those phases. The load curve may reflect additional stresses needed to enforce the isovolumetric phases that are unrelated to the muscle contraction. While these models matched volumes well, simulating proper valve boundary conditions may constrain the volume cost optimizations to also better match measured strain patterns.

Another major assumption about the model was the homogeneous, constant electro-mechanical delay. While this assumption was based on electro-mechanical mapping data, previous finite-element mechanical models by Kerckhoffs et al. showed that a heterogeneous electro-mechanical delay was needed to simulate physiologic patterns of strain.[32] However, the need for heterogeneous electro-mechanical delay may be a result of the active contraction model implemented in

their model. Their results along with ours supports further exploration of active contraction physiology and how it is modeled.

5.4.2 Matching LBBB mechanics

Matching strain is important because it is the input for mechanics-based growth algorithms for predicting long-term remodeling in the heart.[16,22–24] Therefore, we tested an alternate approach of optimizing regional active contraction in the model to match strain measured from DENSE MRI (without input from the electrical model). We allowed for each of the 36 regions to have independent load curves to best match their own regional circumferential and radial strain data.

The data we used for the 6 cases recorded strain after the start of contraction (Fig. 5.2A). The lack of data for early contraction led to poor fits in the simulated volumes (Fig. 5.5B). This finding was not surprising because early errors in contraction could not be corrected leading to error propagation throughout the contraction cycle. At the time point that the simulated strains were referenced (Fig. 5.3, red circle), the incorrect deformation of the LV further confounded the resulting strains. It is likely that the simulated and recorded strains were calculated from different deformed states since the volumes did not match. These optimization cases highlighted the importance of the data used for tuning a finite-element mechanical model. When we optimized a case with strain data starting from end diastole (the start of contraction), the simulated model matched both the volume and strains (Fig. 5.8).

While we only simulated one model that replicated LBBB mechanics, this model did not incorporate any information from the electrical model. The tuned active contraction load curves did not share any common shape and therefore did not provide any insight towards coupling electrical activation times to mechanical contraction (Fig. 5.8E, strain cost). This may be a result of the missing valve boundary condition highlighted in the previous section. Additionally, the hyperparameters of the active contraction model implemented by Estrada et al. and used in our model simulations may need to be re-tuned for LBBB physiology, which has been experimentally shown to feature reduced peak shortening and impaired contractile kinetics.[33,34]

5.5 Conclusions- Finite-element mechanical modeling of LBBB and CRT

In this chapter, we tested a finite-element mechanical model for use in our *Virtual CRT* pipeline for simulating long-term outcomes of CRT. We used optimization schemes to test whether the model could replicate the mechanics of the pre-CRT state (LBBB). By accurately simulating mechanics, our goal was to generalize a method to couple electrical activation times to mechanical contraction. Only one case, dependent on the quality of the recorded mechanical data, achieved promising fits to LV volume and strains throughout the cardiac cycle. A larger set of accurate subject-specific simulations will be needed to explore electro-mechanical coupling methods. Once an electro-mechanical modeling pipeline is developed, electrical activation times can be used to directly simulate LV mechanics without the need for any optimization. To simulate a cardiac cycle, the finite-element model required 4 minutes on a desktop with 4 cores making it computationally tractable for clinical applications.

5.5.1 Current model limitations

Our implementation of a finite-element mechanical model was limited by the available data for model validation and the assumptions we made about subject-specific models. With limited strain data from DENSE MRI, the mechanical models could not simulate both the global and regional mechanics; however, we showed one case with full cardiac cycle DENSE MRI which resulted in improved matches to mechanics. This case demonstrates the need for a more complete data set of regional strain throughout the cardiac cycle to accurately tune the finite-element mechanical models.

To apply our finite-element mechanical modeling pipeline to multiple subject-specific models, we limited the number of subject-specific model parameters by assuming the same material properties, boundary conditions, and active contraction hyperparameters across all subjects. These components of the finite-element mechanical model are difficult to tune from available clinical data; therefore, we set them based on previous finite-element mechanical models developed by our group.[27,35,36] Among these three assumptions, we expect the model to be most sensitive to active contraction hyperparameters. Changes to the material properties may change the magnitude of regional strains but not the temporal pattern of strains. Similarly, the regional

strains we are analyzing are located in the middle of the LV away from the boundary conditions at the base and apex; therefore, the effect of the boundary conditions on regional mechanics is limited. The active contraction hyperparameters include variables affecting the force-length and force-velocity relationships of the simulated muscle. In the case of LBBB, the delayed timing of muscle contraction uses a larger range of the force-length and force-velocity relationships than used in the synchronous heart model simulated by Estrada et al.[27] Therefore, further tuning of active contraction will have the greatest impact on accurately simulating LBBB mechanics.

5.5.2 Future model improvements

The single case we simulated in Fig. 5.8 showed that a data set including full cycle strain can allow for optimization of the model to match both global and regional mechanics. The next step in testing the finite-element mechanical modeling pipeline is repeating the optimization on additional subject-specific models with full cycle strain data. As we work to formulate electro-mechanical coupling and tune active contraction hyperparameters, a bank of subject-specific models will allow for us to vary model parameters and directly quantify their effect on simulated mechanics.

In this chapter, we qualitatively evaluated the shapes of the active contraction load curves to hypothesize electro-mechanical coupling formulations. From the active contraction load curves (Fig. 5.7 and 5.8E), the strain optimizations resulted in increased ranges in active contraction magnitude. We can use this to improve the volume optimization. The volume optimizations featured a common active contraction shape across all regions; however, we could scale the magnitudes of the regional curves based on their electrical activation times. The exact relationship between the electrical activation times and active contraction magnitude can be optimized to match measured volumes. If this new model cannot match both global and regional mechanics, the method can be iterated by adding additional parameters based on the electrical activation times, such as scaling the temporal width of active contraction curves in each region.

Using a bank of subject-specific models, an alternative approach could incorporate more quantitative approaches to tune the active contraction model. For each case in the bank of models, we can employ the strain cost optimization to match the global and regional mechanics. If we repeat the optimizations while varying the active contraction hyperparameters, we can populate a solution space of active contraction load curves that accurately simulate LV mechanics. We

can apply data-driven quantitative approaches, such as machine learning, to simultaneously tune active contraction hyperparameters and formulate the relationship between electrical activation time and active contraction load curves. The final result will have used retrospective data to tune active contraction to be used in prospective simulations of CRT patients.

For clinical translation, we aimed to minimize the number of patient-specific inputs required for making a predictive model. The bank of models will enable us to systematically test the effect of adding in and taking out different patient-specific parameters. We can also simulate sensitivity analyses of various assumptions in the modeling pipeline. For example, we could test the impact of material property changes in the model. Or we could test the effect of implementing different boundary conditions such as isovolumetric constraints.

Another option for improving the mechanical model is incorporating a hemodynamic circuit model similar to the left atrium model in Chapter 2. A circulation model can be used to define the pressure loading and account for hemodynamic feedback associated with LBBB. Furthermore, circulation models (without finite-element coupling) have been used to simulate LV growth and remodeling in different heart diseases including LBBB.[13,37,38] With these recent developments, hemodynamic circuit models could also be used to fully replace our finite-element mechanical model in *Virtual CRT*.

References

[1] J. Constantino, Y. Hu, and N. A. Trayanova, "A computational approach to understanding the cardiac electromechanical activation sequence in the normal and failing heart, with translation to the clinical practice of CRT," *Progress in Biophysics and Molecular Biology*, vol. 110, no. 2-3, pp. 372–379, 2012.

[2] Y. Hu, V. Gurev, J. Constantino, and N. Trayanova, "Optimizing cardiac resynchronization therapy to minimize ATP consumption heterogeneity throughout the left ventricle: A simulation analysis using a canine heart failure model," *Heart Rhythm*, vol. 11, no. 6, pp. 1063–1069, 2014.

[3] A. Lee, U. Nguyen, O. Razeghi, J. Gould, B. Sidhu, B. Sieniewicz, J. Behar, M. Mafi-Rad, G. Plank, F. Prinzen, C. Rinaldi, K. Vernooy, and S. Niederer, "A rule-based method for predicting the electrical activation of the heart with cardiac resynchronization therapy from non-invasive clinical data," *Medical Image Analysis*, vol. 57, pp. 197–213, 2019.

[4] S. A. Niederer, A. K. Shetty, G. Plank, J. Bostock, R. Razavi, N. P. Smith, and C. A. Rinaldi, "Biophysical modeling to simulate the response to multisite left ventricular stimulation using a quadripolar pacing lead," *PACE - Pacing and Clinical Electrophysiology*, vol. 35, no. 2, pp. 204–214, 2012.

[5] J.-i. Okada, T. Washio, M. Nakagawa, M. Watanabe, Y. Kadooka, T. Kariya, H. Yamashita, Y. Yamada, S.-i. Momomura, R. Nagai, T. Hisada, and S. Sugiura, "Multi-scale, tailor-made heart simulation can predict the effect of cardiac resynchronization therapy," *Journal of Molecular and Cellular Cardiology*, vol. 108, pp. 17–23, 7 2017.

[6] N. Panthee, J.-i. Okada, T. Washio, Y. Y. Mochizuki, R. Suzuki, H. Koyama, M. Ono, T. Hisada, and S. Sugiura, "Tailor-made heart simulation predicts the effect of cardiac resynchronization therapy in a canine model of heart failure.," *Medical image analysis*, vol. 31, pp. 46–62, 2016.

[7] M. Sermesant, R. Chabiniok, P. Chinchapatnam, T. Mansi, F. Billet, P. Moireau, J. M. Peyrat, D. Chapelle, R. Razavi, N. Ayache, K. Wong, J. Relan, K. Rhode, M. Ginks, P. Lambiase, H. Delingette, M. Sorine, C. A. Rinaldi, D. Chapelle, R. Razavi, and N. Ayache, "Patient-specific electromechanical models of the heart for the prediction of pacing acute effects in CRT: A preliminary clinical validation," *Medical Image Analysis*, vol. 16, no. 1, pp. 201–215, 2012.

[8] C. Tobon-Gomez, N. Duchateau, R. Sebastian, S. Marchesseau, O. Camara, E. Donal, M. De Craene, A. Pashaei, J. Relan, M. Steghofer, P. Lamata, H. Delingette, S. Duckett, M. Garreau, A. Hernandez, K. S. Rhode, M. Sermesant, N. Ayache, C. Leclercq, R. Razavi, N. P. Smith, and A. F. Frangi, "Understanding the mechanisms amenable to CRT response: From pre-operative multimodal image data to patient-specific computational models," *Medical and Biological Engineering and Computing*, vol. 51, no. 11, pp. 1235–1250, 2013.

[9] T. Arts, T. Delhaas, P. Bovendeerd, X. Verbeek, and F. Prinzen, "Adaptation to mechanical load determines shape and properties of heart and circulation: the CircAdapt model," *American journal of physiology. Heart and circulatory physiology*, vol. 288, pp. 1943–1954, 2005.

[10] J. M. Guccione and A. D. Mcculloch, "Mechanics of Active Contraction in Cardiac Muscle: Part I—Constitutive Relations for Fiber Stress That Describe Deactivation," *Journal of Biomechanical Engineering*, vol. 115, no. 1, p. 72, 1993.

[11] I.-E. Lin and L. A. Taber, "A Model for Stress-Induced Growth in the Developing Heart," *Journal of Biomechanical Engineering*, vol. 117, pp. 343–349, 8 1995.

[12] K. Sunagawa, W. L. Maughan, and K. Sagawa, "Effect of regional ischemia on the left ventricular end-systolic pressure-volume relationship of isolated canine hearts," *Circ Res*, vol. 52, no. 2, pp. 170–178, 1983.

[13] C. M. Witzenburg and J. W. Holmes, "Predicting the Time Course of Ventricular Dilation and Thickening Using a Rapid Compartmental Model," *Journal of Cardiovascular Translational Research*, vol. 11, pp. 109–122, 4 2018.

[14] J. L. Emery and J. H. Omens, "Mechanical regulation of myocardial growth during volume-overload hypertrophy in the rat.," *The American journal of physiology*, vol. 273, no. 3 Pt 2, pp. H1198–H1204, 1997.

[15] S. Göktepe, O. J. Abilez, K. K. Parker, and E. Kuhl, "A multiscale model for eccentric and concentric cardiac growth through sarcomerogenesis," *Journal of Theoretical Biology*, vol. 265, no. 3, pp. 433–442, 2010.

[16] R. C. P. Kerckhoffs, J. H. Omens, and A. D. McCulloch, "Mechanical discoordination increases continuously after the onset of left bundle branch block despite constant electrical dyssynchrony in a computational model of cardiac electromechanics and growth," *Europace*, vol. 14, no. SUPPL. 5, pp. 65–72, 2012.

[17] W. Kroon, T. Delhaas, T. Arts, and P. Bovendeerd, "Computational modeling of volumetric soft tissue growth: Application to the cardiac left ventricle," *Biomechanics and Modeling in Mechanobiology*, vol. 8, no. 4, pp. 301–309, 2009.

[18] C. M. Witzenburg and J. W. Holmes, "A Comparison of Phenomenologic Growth Laws for Myocardial Hypertrophy," *Journal of Elasticity*, vol. 129, no. 1-2, pp. 257–281, 2017.

[19] J. J. Cao, N. Ngai, L. Duncanson, J. Cheng, K. Gliganic, and Q. Chen, "A comparison of both DENSE and feature tracking techniques with tagging for the cardiovascular magnetic resonance assessment of myocardial strain," *Journal of Cardiovascular Magnetic Resonance*, vol. 20, no. 1, pp. 1–9, 2018.

[20] D. Kim, W. D. Gilson, C. M. Kramer, and F. H. Epstein, "Myocardial Tissue Tracking with Two-dimensional Cine Displacement-encoded MR Imaging: Development and Initial Evaluation," *Radiology*, vol. 230, no. 3, pp. 862–871, 2004.

[21] T.-K. N. Phung, C. D. Waters, and J. W. Holmes, "Open-Source Routines for Building Personalized Left Ventricular Models From Cardiac Magnetic Resonance Imaging Data," *Journal of Biomechanical Engineering*, vol. 142, pp. 1–6, 2 2020.

[22] J. Arumugam, J. Mojumder, G. Kassab, and L. C. Lee, "Model of Anisotropic Reverse Cardiac Growth in Mechanical Dyssynchrony," *Scientific Reports*, vol. 9, p. 12670, 12 2019.

[23] D. Klepach, L. C. Lee, J. F. Wenk, M. B. Ratcliffe, T. I. Zohdi, J. L. Navia, G. S. Kassab, E. Kuhl, and J. M. Guccione, "Growth and remodeling of the left ventricle: A case study of myocardial infarction and surgical ventricular restoration," *Mechanics Research Communications*, vol. 42, pp. 134–141, 6 2012.

[24] L. C. Lee, J. Sundnes, M. Genet, J. F. Wenk, and S. T. Wall, "An integrated electromechanical-growth heart model for simulating cardiac therapies," *Biomechanics and Modeling in Mechanobiology*, vol. 15, pp. 791–803, 8 2016.

[25] B. S. Spottiswoode, X. Zhong, A. T. Hess, C. M. Kramer, E. M. Meintjes, B. M. Mayosi, and F. H. Epstein, "Tracking myocardial motion from cine DENSE images using spatiotemporal phase unwrapping and temporal fitting," *IEEE Transactions on Medical Imaging*, vol. 26, no. 1, pp. 15–30, 2007.

[26] S. A. Maas, B. J. Ellis, G. A. Ateshian, and J. A. Weiss, "FEBio: Finite Elements for Biomechanics," *Journal of Biomechanical Engineering*, vol. 134, no. 1, p. 011005, 2012.

[27] A. C. Estrada, K. Yoshida, S. A. Clarke, and J. W. Holmes, "Longitudinal Reinforcementof Acute Myocardial Infarcts Improves Function by Transmurally Redistributing Stretch and Stress," *Journal of Biomechanical Engineering*, vol. 142, no. 2, pp. 1–10, 2020.

[28] C. B. Moyer, P. a. Helm, C. J. Clarke, L. P. Budge, C. M. Kramer, J. D. Ferguson, P. T. Norton, and J. W. Holmes, "Wall-motion based analysis of global and regional left atrial mechanics," *IEEE Transactions on Medical Imaging*, vol. 32, no. 10, pp. 1765–1776, 2013.

[29] F. R. Badke, P. Boinay, and J. W. Covell, "Effects of ventricular pacing on regional left ventricular performance in the dog," *American Journal of Physiology-Heart and Circulatory Physiology*, vol. 238, pp. H858–H867, 6 1980.

[30] B. T. Wyman, W. C. Hunter, F. W. Prinzen, and E. R. McVeigh, "Mapping propagation of mechanical activation in the paced heart with MRI tagging.," *The American journal of physiology*, vol. 276, no. 3 Pt 2, pp. H881–H891, 1999.

[31] O. P. Faris, F. J. Evans, D. B. Ennis, P. A. Helm, J. L. Taylor, A. S. Chesnick, M. A. Guttman, C. Ozturk, and E. R. McVeigh, "Novel technique for cardiac electromechanical mapping with magnetic resonance imaging tagging and an epicardial electrode sock," *Annals of Biomedical Engineering*, vol. 31, no. 4, pp. 430–440, 2003.

[32] R. C. P. Kerckhoffs, P. H. M. Bovendeerd, J. C. S. Kotte, F. W. Prinzen, K. Smits, and T. Arts, "Homogeneity of cardiac contraction despite physiological asynchrony of depolarization: A model study," *Annals of Biomedical Engineering*, vol. 31, no. 5, pp. 536–547, 2003.

[33] K. Chakir, S. K. Daya, T. Aiba, R. S. Tunin, V. L. Dimaano, T. P. Abraham, K. Jacques, E. W. Lai, K. Pacak, W. Z. Zhu, R. P. Xiao, G. F. Tomaselli, and D. A. Kass, "Mechanisms of enhanced β-adrenergic reserve from cardiac resynchronization therapy," *Circulation*, vol. 119, no. 9, pp. 1231–1240, 2009.

[34] J. A. Kirk and D. A. Kass, "Cellular and Molecular Aspects of Dyssynchrony and Resynchronization.," *Cardiac electrophysiology clinics*, vol. 7, pp. 585–97, 12 2015.

[35] C. B. Moyer, P. T. Norton, J. D. Ferguson, and J. W. Holmes, "Changes in Global and Regional Mechanics Due to Atrial Fibrillation: Insights from a Coupled Finite-Element and Circulation Model.," *Annals of biomedical engineering*, vol. 43, no. 7, pp. 1600–1613, 2015.

[36] C. B. Moyer, *Mechanical Function of the Left Atrium*. PhD thesis, University of Virginia, 2013.

[37] P. J. A. Oomen, C. M. Witzenburg, T.-K. N. Phung, K. C. Bilchick, and J. W. Holmes, "Fast Predictions of Cardiac Growth During Ventricular Dyssynchrony," in *Proceedings of the 2019 Summer Biomechanics, Bioengineering and Biotransport Conference*, (Seven Springs, PA), 2019.

[38] J. Walmsley, T. Arts, N. Derval, P. Bordachar, H. Cochet, S. Ploux, F. W. Prinzen, T. Delhaas, and J. Lumens, "Fast Simulation of Mechanical Heterogeneity in the Electrically Asynchronous Heart Using the MultiPatch Module," *PLoS Computational Biology*, vol. 11, no. 7, pp. 1–23, 2015.

6

Conclusions- Computational modeling for the clinic

Computational modeling is a powerful tool for simulating cardiac injuries and therapies. Researchers build biophysical models by developing and tuning governing equations to replicate recorded data. These models can then be extended to test *de novo* conditions, develop therapies, and design experiments. There is an immense, untapped potential for integrating computational models into clinical decision making. And this opportunity will require tailoring computational modeling methods to suit the needs of physicians and patients. Even as researchers continue developing novel computational methods, older, validated modeling techniques can be adapted for the clinic. Two current examples include HeartFlow and Medtronic's CardioInsight Cardiac Mapping. HeartFlow simulates patient-specific coronary blood flow to predict coronary artery disease.* And CardioInsight maps electrical information onto the heart surface to characterize cardiac arrhythmias.†

*Heartflow.com
†Medtronic.com

In this dissertation, we demonstrated the use of computational modeling at different spatial and computational scales for different clinical applications. In Chapter 2, we employed a coupled hemodynamic circuit and finite-element mechanical model of the left atrium. While the model may be too complex to tailor for patient-specific simulations, the validated baseline model was used to directly compare various ablation patterns. Theoretically, this model can be used to design new ablation patterns not yet available in the clinic. In Chapters 3, 4, and 5, we developed methods geared towards patient-specific clinical applications. In Chapter 3, we created a data fusion routine to register and display anatomic and functional information from multimodal imaging. This method serves as the initial step for building and validating a biophysical model; however, the display of the information is already a useful tool for clinical decision making. The data fusion routine was developed to quickly generate a patient-specific visual for CRT planning within 24 hours and is currently being tested in a randomized clinical trial.[‡] In Chapter 4, we developed and validated a simple, fast electrical model capable of simulating LBBB and LV pacing, which in the future will drive models of LV mechanics, growth, and remodeling in response to CRT. In Chapter 5, we tested finite-element mechanical modeling for simulating accurate LBBB mechanics, which is necessary for making predictions about LV growth and remodeling.

The work in Chapters 4 and 5 aims to improve upon the decision-making tool developed in Chapter 3 by introducing biophysically based predictive modeling. Future work for the modeling pipeline includes improving the finite-element mechanical modeling method to better match *in vivo* mechanics or switching to an alternative mechanical modeling technique, such as compartmental modeling. Then, incorporating a mechanics-based growth algorithm will enable simulations of long-term CRT outcomes. If the pipeline is computationally efficient, *Virtual CRT* can be used in the clinic by physicians to rapidly screen potential CRT lead configurations and optimize patient-specific CRT prior to implantation. Overall, this pipeline will connect three well established advancements in the field of cardiac modeling (simulating electrical activation patterns, LV mechanics, and LV growth and remodeling) and translate them to the clinic.

As we translate *Virtual CRT* to the clinic, we will need to comprehensively assess the modeling results and how they should be interpreted by physicians. For a given CRT pacing lead location, the main output from *Virtual CRT* will be the predicted change in end diastolic vol-

[‡]clinicaltrials.gov/ct2/show/NCT03398369

ume of the LV six months after CRT. This metric can be used by physicians to plan CRT lead placement. However, given the generalized assumptions we use in the modeling pipeline, we will need a method to evaluate the confidence of our predictions. We can apply developments from the field of *uncertainty quantification* to assess the *Virtual CRT* modeling pipeline and calculate confidence intervals for our predictions.

Furthermore, we will need to develop a method to test *Virtual CRT* predictions in a clinical setting. We can first retrospectively test the modeling pipeline accuracy by simulating patient-specific CRT lead placement and comparing the model predictions to recorded patient outcomes. The modeling pipeline should be tested on a patient data set including those who succeeded and those who failed to respond to CRT. The model can then be tested in a prospective clinical trial in which a control group receives standard treatment and a test group receives *Virtual CRT* optimized CRT lead placement.

This dissertation presented computational modeling specifically for the heart to guide therapies; however, there are undoubtedly many areas in medicine which may benefit from looking back to simpler models for uses in the clinic. The opportunity for clinically translatable models is becoming more evident as the library of computational models expands with new advances in experimental techniques. For example, computational modeling of the lungs has followed a similar trajectory to the cardiovascular field. Lung modeling has ranged in complexity from simple lumped parameter models to simulate global lung mechanics to more complex finite-element models to predict particulate deposition throughout the airway tree. The remodeling of the lung through different diseases, such as asthma and pulmonary fibrosis, presents an opportunity for developing mechanics-based growth algorithms similar to the heart to predict long-term functional changes. As computational models are continually developed and improved, their impact in medicine will be even greater if they can be adapted for use in the clinic.